# Exploring the opportunities of piezoelectric composites for shear strain-driven energy harvesting

## Frederik Van Loock

Faculty of Aerospace Engineering · Delft University of Technology

**TU**Delft
Delft
University of
Technology

# Exploring the opportunities of piezoelectric composites for shear strain-driven energy harvesting

MASTER OF SCIENCE THESIS

For obtaining the degree of Master of Science in Aerospace Engineering at Delft University of Technology

Frederik Van Loock

22 October 2014

**GRADUATION COMMITTEE**

Dated: 22 October 2014

Comittee chairman :

<div style="text-align:right">Prof. dr. W.A. Groen</div>

Committee members:

<div style="text-align:right">Prof. dr. ir. S. van der Zwaag</div>

<div style="text-align:right">Dr. ir. R. De Breuker</div>

<div style="text-align:right">Ir. D.B. Deutz</div>

# Abstract

This thesis investigates the shear strain-driven energy harvesting performance of compliant piezoelectric composite material systems.

A characterization study was performed to observe and quantify the piezoelectric shear coupling of two phase piezoelectric composite materials ranging from 0-3 (particulate) to 1-3 (fiber) composites. To this aim, the shear mode properties of piezoelectric composites were experimentally established by a novel impedance-based measurement technique, which was complemented with standard quasi-static measurements. Finite element simulations were performed to validate the new method. Moreover, homogenization-based finite element simulations served to numerically obtain the effective properties of the experimentally investigated material systems.

Next, the energy-based performance of a compliant composite patch provided with interdigitated electrodes was assessed for shear and axial strain-driven mechanical excitation schemes. Numerical simulations by means of an adaptive finite element model were performed to determine the effect of the patches' electrode geometry on its energy harvesting capability. In addition, two finite energy harvesting case studies were developed to investigate the effect of complex strain distributions and to suggest practical experimental validation schemes for the purely numerical approach presented in this thesis.

# Table of contents

# List of figures

# List of tables

# Nomenclature

**Abbreviations**

| Symbol | Description |
|--------|-------------|
| Au | Gold atom |
| Ba | Barium atom |
| C | Carbon atom |
| Cu | Copper atom |
| DC | Direct current |
| DEP | Dielectrophoresis |
| EBC | Electrical boundary condition |
| FEA | Finite element analysis |
| FEM | Finite element model |
| FOM | Figure of merit |
| GFRP | Glass fiber reincorced polymer |
| IDE | Interdigitated electrodes |
| MBC | Mechanical boundary condition |
| MSA | Multilayer stack actuator |
| O | Oxygen atom |
| P(VDCN-VA) | Polyvinylidene vinylacetate |
| PAN | Polyacrilonitrile |
| Pb | Lead atom |
| PEH | Piezoelectric energy harvesting/harvester |
| PPE | Parallel plate electrodes |
| PVDF | Polyvinylidene fluoride |
| PZT | Lead zirconium titanate |
| RE | Relative error |
| rpm | Revolutions per minute |
| RVE | Reduced volume element |
| SEM | Scanning electron microscope |
| SFC | Structured fiber composite |
| Sn | Tin atom |
| SS | Substrate |
| Ti | Titanium atom |
| Zr | Zirconium atom |

**Latin symbols**

| Symbol | Description | Units |
|--------|-------------|-------|
| $B$ | Susceptance | $[\Omega]$ |
| $C$ | Capacitance | $[F]$ |
| $C_{free}$ | Free capacitance | $[F]$ |
| $c_{ij}$ | Stiffness | $[\frac{N}{m^2}]$ |
| $d_{ij}$ | Piezoelectric charge constant | $[\frac{C}{N}]$ |
| $D_i$ | Electric displacement | $[\frac{C}{m^2}]$ |
| $du$ | Displacement along the x-axis | $[m]$ |
| $dv$ | Displacement along the z-axis | $[m]$ |
| $E_i$ | Electric field | $[\frac{V}{m}]$ |
| $e_i$ | Unit vector | $[-]$ |
| $f_a$ | Antiresonance frequency | $[Hz]$ |
| $f_m$ | Minimum impedance frequency | $[Hz]$ |
| $f_n$ | Maximum impedance frequency | $[Hz]$ |
| $f_p$ | Parallel antiresonance frequency | $[Hz]$ |
| $f_r$ | Resonance frequency | $[Hz]$ |
| $f_s$ | Series resonance frequency | $[Hz]$ |
| $F_t$ | Tensile force | $[N]$ |
| $F_v$ | Vertical tip force | $[N]$ |
| $FOM_{ef,dyn}$ | Dynamic efficiency FOM | $[-]$ |
| $g$ | Piezoelectric voltage constant | $[\frac{Vm}{N}]$ |
| $k$ | Variable IDE dimension function | $[m]$ |
| $k'$ | Variable IDE dimension function | $[m]$ |
| $K(x)$ | Complete elliptical integral of the first kind | $[-]$ |
| $k_{ij}$ | Piezoelectric coupling factor | $[-]$ |
| $k_{sys}$ | System coupling factor | $[-]$ |
| $l$ | Sample length | $[m]$ |
| $L_{beam}$ | Beam length | $[m]$ |
| $L_{rod}$ | Rod length | $[m]$ |
| $L_{RVE}$ | RVE dimension | $[m]$ |
| $M_t$ | Torsional moment | $[Nm]$ |
| $n$ | Number of finite elements | $[-]$ |
| $n_a$ | Number of active material layers | $[-]$ |
| $P$ | Polarization density | $[\frac{C}{m^2}]$ |
| $p$ | Common electrode finger width | $[m]$ |
| $Q_{gen}$ | Generated charge | $[C]$ |
| $Q_{m,sys}$ | System mechanical quality factor | $[-]$ |
| $Q_m$ | Mechanical quality factor | $[-]$ |
| $r_{rod}$ | Rod radius | $[m]$ |
| $RE_{max}$ | Maximum relative error | $[-]$ |
| $s_{ij}$ | Compliance | $[\frac{m^2}{N}]$ |
| $s_f$ | Electrode finger spacing | $[m]$ |
| $S_i$ | Strain (engineering) | $[-]$ |
| $T$ | Temperature | $[^\circ C]$ |
| $t$ | Sample thickness | $[m]$ |
| $T_c$ | Curie temperature (piezoelectric) | $[^\circ C]$ |
| $T_i$ | Stress | $[\frac{N}{m^2}]$ |
| $t_p$ | Patch thickness | $[m]$ |
| $t_s$ | Side electrode thickness | $[m]$ |

| | | |
|---|---|---|
| $U_{el}$ | Elastic deformation energy | $[J]$ |
| $U_{gen}$ | Generated energy | $[J]$ |
| $V$ | Electric potential | $[V]$ |
| $V_{gen}$ | Generated voltage | $[V]$ |
| $w$ | Sample width | $[m]$ |
| $w_{beam}$ | Beam width | $[m]$ |
| $W_{el}^{S}$ | Strain density energy density | $[\frac{J}{m^3}]$ |
| $w_{el}^{S}$ | Strain density energy density constant | $[\frac{J}{m^3}]$ |
| $W_{el}^{T}$ | Stress density energy density | $[\frac{J}{m^3}]$ |
| $w_{el}^{T}$ | Stress density energy density constant | $[\frac{m^3}{J}]$ |
| $w_f$ | Electrode finger width | $[m]$ |
| $X$ | Reactance or Controlling dimension | $[S$ or $m]$ |
| $Y$ | Admittance | $[S]$ |
| $Z$ | Impedance | $[\Omega]$ |
| $Z_p$ | Patch surface dimension | $[m]$ |

## Greek symbols

| Symbol | Description | Units |
|---|---|---|
| $\gamma_{ij}$ | Engineering shear strain | $[-]$ |
| $\epsilon_{ij}$ | Tensorial shear strain | $[-]$ |
| $\epsilon_0$ | Absolute vacuum permittivity | $[\frac{F}{m}]$ |
| $\epsilon_{ij}^{a,T}$ | Zero stress absolute permittivity | $[\frac{F}{m}]$ |
| $\eta_{IDE}$ | IDE energy density efficiency | $[-]$ |
| $\eta_{stat}$ | Static electromechanical efficiency | $[-]$ |
| $\eta_{dyn}$ | Dynamic electromechanical efficiency | $[-]$ |
| $\eta_{sys,dyn}$ | Dynamic system efficiency | $[-]$ |
| $\theta_{rot}$ | (Patch) rotation angle | $[°]$ |
| $\lambda$ | Wavelength | $[m]$ |
| $\nu$ | Elastic wave velocity | $[\frac{m}{s}]$ |
| $\rho$ | Material density | $[\frac{kg}{m^3}]$ |

# Preface

This MSc. thesis concludes my time as an Aerospace Engineering student at the TU Delft. It is with great pleasure that I present the results of the thesis research project performed at the Novel Aerospace Materials (NovAM) group.

This thesis would not have been possible without the support of many people.
First and foremost I would like to thank my principal supervisor Prof. dr. Pim Groen for giving me the opportunity to work on the topic of piezoelectric energy harvesting within the NovAM smart materials team. In spite of his admirable knowledge of and vast experience with piezoelectric technologies, he granted me a lot of freedom to develop the outline of this thesis, which is much appreciated too. Moreover, his way of coaching and lecturing students definitely changed my view on how to work and communicate in an academic environment.

I would also like to take the opportunity to thank my second supervisor Prof. dr. ir. Sybrand van der Zwaag. His guidance proved to be a continuous source of inspiration and motivation throughout my thesis and, without doubt, for the rest of my life.

I owe a lot to my daily supervisor, Daniella Deutz. Thank you for sacrificing so much of your time, for the insightful talks during or in between the experiments and simulations, and taking a personal interest in my work. I would also like to acknowledge Hamideh Khanbareh, Nijesh K. James and the rest of the NovAM (smart materials) group. Doing a MSc. thesis at NovAM turned out to be an unforgettable experience, thanks to all!

Lastly, I would like to thank my friends and family. Especially my parents, Geertje and Dr. Raymond, for their support and faith in me. Thank you mom and dad.

"As far as the laws of mathematics refer to reality, they are not certain, as far as they are certain, they do not refer to reality."

— *A. Einstein (1921)*

# Chapter 1

# Introduction

Electromechanical energy harvesting received an increased amount of interest during the last decade by both academics and industry due to its remarkable ability to recover mechanical waste energy; an attractive technology for the present and future need for sustainable energy generation and delivery solutions [1]. Amongst the common electromechanical coupling methods, piezoelectric energy harvesting has become the dominant conversion mechanism for low-power energy scavenging as it is characterized by relatively high power densities and it does not suffer from drawbacks such as low output voltages or external voltage source requirements [2–4].

Several piezoelectric energy harvesting applications, ranging from wireless sensor nodes powered by mechanical vibrations for structural health monitoring of aerospace structures to biomedical implantable devices powered by blood pressure cycles, have successfully been developed and tested (see Figure 1.1) [5, 6]. By integrating piezoelectric energy harvesters (PEHs) in these systems advantages, including, but not limited to, maintenance cost reduction, reduction of hazardous waste material from electrochemical energy storage devices, and safety improvements can be achieved [2, 7].

**(a)**

**(b)**
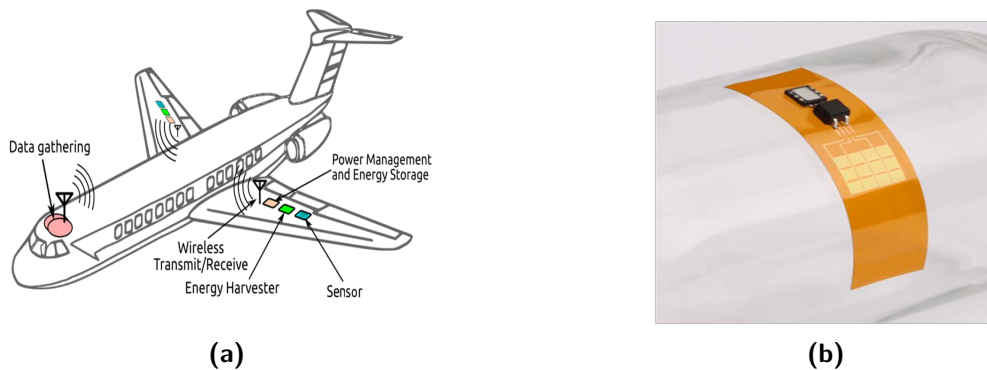
**Figure 1.1:** Overview of a self-powered (wireless) aircraft structural health monitoring concept (a) and a flexible piezoelectric energy harvesting device developed as a power source for biomedical electronic implants (b) [6, 8].

Although the outlook of piezoelectric energy harvesting is promising, the amount of harvesters used in praxis remains limited as the technology is far from mature [7, 9, 10]. Improvement of the properties of the employed conversion materials, the optimization of the attached electronic circuits, and the realisation of compliant (high strain resistant) harvesters are some of the paramount issues to be dealt with for further performance enhancement of the piezoelectric energy harvesting technology [4]. This thesis will focus on the latter topic; how are flexible piezoelectric composite materials efficiently employed for piezoelectric energy harvesting purposes?

The aim of this chapter is to introduce the reader to the concept as well as the design and performance assessment considerations for piezoelectric energy harvesting. Section 1.1 discusses piezoelectricity focusing on the piezoelectric constitutive equations, operation modes, and common materials. Subsequently, Section 1.2 presents the basic design features of a typical PEH system. Next, the PEH figures of merits are introduced in Section 1.3. Based on the findings of the proceeding sections, the final section of this introductory chapter (Section 1.4) presents the scope and outline of the thesis.

## 1.1 Piezoelectricity

The direct piezoelectric[1] effect was demonstrated experimentally by the brothers Jacques and Pierre Curie in 1880 [12, 13]. When a mechanical load is applied on a piezoelectric material, an electrical charge is generated (direct piezoelectric effect, see Figure 1.2a), and vice versa, the material deforms upon application of an electric field (inverse piezoelectric effect, see Figure 1.2b) [13]. The inverse effect can be used for actuating applications such as adaptive aerostructures, whereas the direct effect can serve for sensory applications such as vibrational energy harvesters or touch sensors [11].
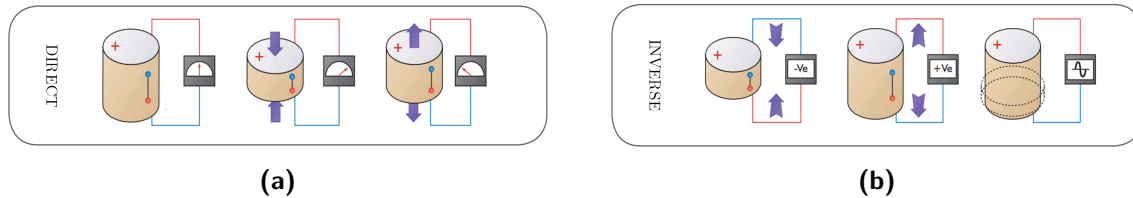


**Figure 1.2:** The direct (a) and inverse (b) piezoelectric effect. Adapted from [14].

A theoretical basis to describe the piezoelectric effect is presented in the next subsection (Section 1.1.1). The three dominant piezoelectric modes are briefly discussed in Section 1.1.2. Lastly, a short overview of the common piezoelectric materials applied for energy harvesting applications is presented in Section 1.1.3.

### 1.1.1 Piezoelectric equations and constants

The coupling of the mechanical (stress and strain) and electrical (field and displacement) physical domains by piezoelectric materials can be described by the standard piezoelectric linear constitutive equations. A short form notation in vector-matrix format is presented in Equation 1.1 [11, 15].

---

[1]The term *Piezoelectricity* is derived from the ancient greek words '$\pi\iota\epsilon\zeta\epsilon\iota\nu$' ('to press') and '$\eta\lambda\epsilon\kappa\tau\rho\rho\nu$' ('amber', a natural material known to exhibit electrical charging properties in the Classical Antiquity), meaning literately 'electricity by pressing' [11].

$$
\begin{bmatrix} \bar{S} \\ \bar{D} \end{bmatrix} = \begin{bmatrix} \bar{\bar{s}}^{E} & \bar{\bar{d}}^{t} \\ \bar{\bar{d}} & \bar{\bar{\epsilon}}^{a,T} \end{bmatrix} \begin{bmatrix} \bar{T} \\ \bar{E} \end{bmatrix} \tag{1.1}
$$

Where in Equation 1.1, $\bar{S}$ $[-]$ is the strain vector, $\bar{D}$ $[\frac{C}{m^2}]$ the electric displacement vector, $\bar{\bar{s}}^{E}$ $[\frac{m^2}{N}]$ the short-circuit[2] material's compliance matrix, $\bar{\bar{d}}$ $[\frac{C}{N}]$ the material's piezoelectric coupling matrix, $\bar{\bar{\epsilon}}^{a,T}$ $[\frac{F}{m}]$ the material's zero stress[3] absolute permittivity matrix, $\bar{T}$ $[\frac{N}{m^2}]$ the stress vector, and $\bar{E}$ $[\frac{V}{m}]$ the electric field vector.
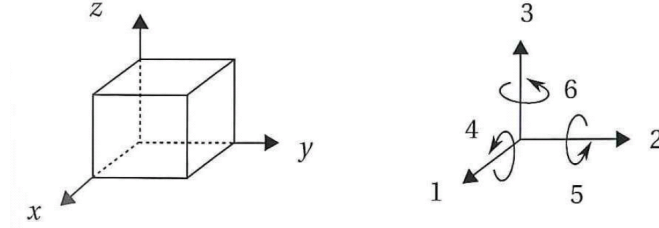


**Figure 1.3:** The standard piezoelectric axes system. Obtained from [11].

The elements of these electromechanical property matrices and state vectors are described with respect to the standard piezoelectric orthogonal axes system (see Figure 1.3). By convention, the 3-axis is directed along the poling axis of the piezoelectric material[4] [13, 15]. The full version of the piezoelectric linear constitutive equations in matrix-vector format can be formulated as presented in Equation 1.2.

$$
\begin{bmatrix} S_1 \\ S_2 \\ S_3 \\ S_4 \\ S_5 \\ S_6 \\ D_1 \\ D_2 \\ D_3 \end{bmatrix} = \begin{bmatrix} s_{11}^{E} & s_{12}^{E} & s_{13}^{E} & s_{14}^{E} & s_{15}^{E} & s_{16}^{E} & d_{11} & d_{21} & d_{31} \\ s_{21}^{E} & s_{22}^{E} & s_{23}^{E} & s_{24}^{E} & s_{25}^{E} & s_{26}^{E} & d_{12} & d_{22} & d_{32} \\ s_{31}^{E} & s_{32}^{E} & s_{33}^{E} & s_{34}^{E} & s_{35}^{E} & s_{36}^{E} & d_{13} & d_{23} & d_{33} \\ s_{41}^{E} & s_{42}^{E} & s_{43}^{E} & s_{44}^{E} & s_{45}^{E} & s_{46}^{E} & d_{14} & d_{24} & d_{34} \\ s_{51}^{E} & s_{52}^{E} & s_{53}^{E} & s_{54}^{E} & s_{55}^{E} & s_{56}^{E} & d_{15} & d_{25} & d_{35} \\ s_{61}^{E} & s_{62}^{E} & s_{63}^{E} & s_{64}^{E} & s_{65}^{E} & s_{66}^{E} & d_{16} & d_{26} & d_{36} \\ d_{11} & d_{12} & d_{13} & d_{14} & d_{15} & d_{16} & \epsilon_{11}^{a,T} & \epsilon_{12}^{a,T} & \epsilon_{13}^{a,T} \\ d_{21} & d_{22} & d_{23} & d_{24} & d_{25} & d_{26} & \epsilon_{21}^{a,T} & \epsilon_{22}^{a,T} & \epsilon_{23}^{a,T} \\ d_{31} & d_{32} & d_{33} & d_{34} & d_{35} & d_{36} & \epsilon_{31}^{a,T} & \epsilon_{32}^{a,T} & \epsilon_{33}^{a,T} \end{bmatrix} \begin{bmatrix} T_1 \\ T_2 \\ T_3 \\ T_4 \\ T_5 \\ T_6 \\ E_1 \\ E_2 \\ E_3 \end{bmatrix} \tag{1.2}
$$

Where in Equation 1.2, $S_i$ $[-]$ is the strain in the $i$-direction grouped by $\bar{S}$, $D_i$ $[\frac{C}{m^2}]$ is the electric displacement in the $i$-direction grouped by $\bar{D}$, $s_{ij}^{E}$ $[\frac{m^2}{N}]$ the short-circuit elastic compliance in the $i$- and $j$-direction grouped by $\bar{\bar{s}}^{E}$, $d_{ij}$ $[\frac{m}{V}{=}\frac{C}{N}]$ the piezoelectric charge constant in the $i$- and $j$-direction grouped by $\bar{\bar{d}}$, $\epsilon_{ij}^{a,T}$ $[\frac{F}{m}]$ the material's zero stress absolute permittivity in the $i$- and $j$-direction grouped by $\bar{\bar{\epsilon}}^{a,T}$, $T_i$ $[\frac{N}{m^2}]$ the stress in the $i$-direction grouped by $\bar{T}$, and $E_i$ $[\frac{V}{m}]$ the electric field in the $i$-direction grouped by $\bar{E}$.

For energy harvesting, one is interested in the electric field (or voltage) resulting from an applied stress (or strain) on the piezoelectric material. Therefore, switching $\bar{E}$ and $\bar{D}$ in Equation 1.1 and omitting the directional subscripts, a generic form of the strain-voltage piezoelectric constitutive equations can be obtained as formulated in Equation 1.3.

---

[2]For short-circuit electrical boundary conditions the electric field is zero or constant.
[3]Zero stress refers to a zero or constant stress mechanical boundary condition.
[4]The poling process is discussed in Section 2.2.1.

$$\begin{bmatrix} S \\ E \end{bmatrix} = \begin{bmatrix} s^D & g \\ -g & (\epsilon^{a,T})^{-1} \end{bmatrix} \begin{bmatrix} T \\ D \end{bmatrix} \qquad (1.3)$$

Where in Equation 1.3, $g$ $[\frac{Vm}{N} = \frac{m^2}{C}]$ is the piezoelectric voltage constant related to the charge constant $d$ as formulated in Equation 1.4, and $s^D$ is the open circuit[5] elastic compliance related to the short-circuit compliance $s^E$ as described in Equation 1.5 [11].

$$g = \frac{d}{\epsilon^{T,a}} \qquad (1.4)$$

$$s^D = s^E - \frac{d^2}{\epsilon^{a,T}} = s^E\left(1 - \frac{d^2}{s^E \epsilon^{a,T}}\right) = s^E(1 - k^2) \qquad (1.5)$$

Where in Equation 1.5, $k$ [-] is the piezoelectric coupling factor. This coupling factor is an important figure for the performance assessment of PEH materials as $k^2$ defines how efficiently the input mechanical or electrical energy is converted to electrical or mechanical energy, respectively, as described in Equation 1.6 [1, 13, 16].

$$k^2 = \frac{\text{Electrical energy converted to mechanical energy}}{\text{Input electrical energy}} = \frac{\text{Mechanical energy converted to electrical energy}}{\text{Input mechanical energy}} \qquad (1.6)$$

For alternating electrical excitation of a piezoelectric material, the mechanical quality factor $Q_m$ $[-]$ is a measure of the amplification of the vibrational mechanical output signal, induced by the inverse piezoelectric effect, at the resonance frequency $f_r$ $[Hz]$ [17]. Hence, $Q_m$ accounts for the mechanical losses/damping occurring at resonance and is, by consequence, an important material parameter for piezoelectric energy harvesters (PEHs) operating on dynamic (vibrational) load cases. For a detailed discussion of the mechanical quality factor the interested reader is referred to the paper of *Uchino et al.* or the seminal book on piezoelectric ceramics of *Jaffe et al.* [13, 17].

### 1.1.2 Piezoelectric operation modes

The piezoelectric operation modes describe the coupling of the electrical and mechanical energy domains [11]. An operation mode can be employed by application of the correct combination of electrical and mechanical boundary conditions. For PEHs, the two prevalent operational modes are the $d_{33}$-mode (longitudinal operation) for which both the electric field and mechanical deformation/stress are along the 3-axis (poling axis, see Section 1.1.1) and the $d_{31}$-mode (transverse operation) for which the electric field and mechanical deformation/stress is along the 3- and 1-axis, respectively [10, 11]. A less common operational mode is the shear or $d_{15}$-mode for which the piezoelectric body is sheared around the axis perpendicular to the plane formed by the poling axes (3-axis) and applied electrode axis (1-axis). The $d_{33}$-, $d_{31}$-, and $d_{15}$-modes are depicted in Figure 1.4.

Henceforth, the piezoelectric coupling factor can be defined with respect to the mode of operation by use of the appropriate indices as presented in Equation 1.7 ($d_{33}$-mode), Equation 1.8 ($d_{31}$-mode), and Equation 1.9 ($d_{15}$-mode) [13].

---

[5]For open circuit electrical boundary conditions, the electric displacement is zero or constant.
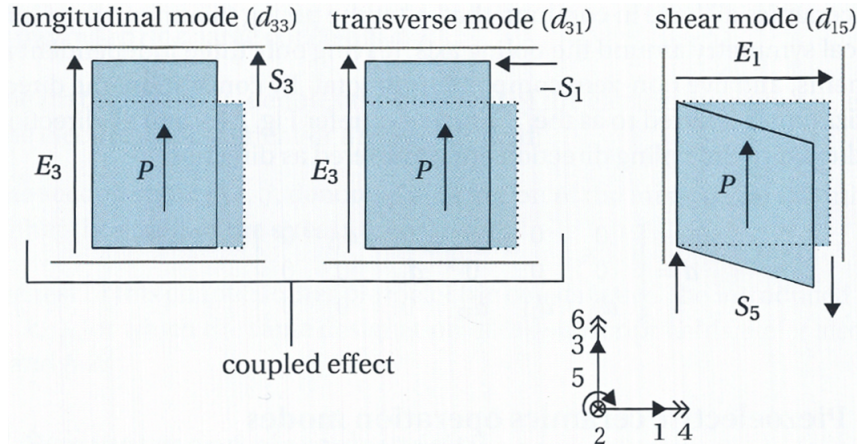
**Figure 1.4:** The longitudinal, transverse, and shear piezoelectric operation modes (from left to right). Note that the longitudinal and transverse modes are inherently coupled. Obtained from [11].

$$k_{33}^2 = \frac{d_{33}^2}{s_{33}^E \epsilon_{33}^{a,T}} \qquad (1.7) \qquad k_{31}^2 = \frac{d_{31}^2}{s_{11}^E \epsilon_{33}^{a,T}} \qquad (1.8) \qquad k_{15}^2 = \frac{d_{15}^2}{s_{55}^E \epsilon_{11}^{a,T}} \qquad (1.9)$$

### 1.1.3 Piezoelectric materials

A wide range of materials exhibit the piezoelectric phenomenon, commonly classified as piezoelectric single crystals (i), piezoelectric ceramics (ii), thin film piezoelectrics (iii), piezoelectric polymers (iv), and piezoelectric composites (v) [18, 19]. The three most frequently applied material classes for energy harvesting applications, being piezoelectric ceramics, polymers, and composites, are briefly discussed in the coming paragraphs. A comprehensive overview of the various piezoelectric materials can be found in the book of *Holterman* and *Groen* [11].

**Piezoelectric ceramics**

The commercially available piezoelectric ceramic PZT (lead zirconium titanate or Pb[Zr$_x$Ti$_{1-x}$]O$_3$) is probably the most known and applied piezoelectric material [2, 3, 10]. PZT is a polycrystalline material with a perovskite structure commonly denoted by the general A$^{2+}$B$^{4+}$O$_3^{-2}$ formula [11, 13, 20]. For perovskite crystal structures A$^{2+}$ and B$^{4+}$ cations are arranged with oxygen O$^{2-}$ anions in various crystal structures depending on a.o. the material's temperature. Below a critical temperature, known as the (piezoelectric) *Curie* temperature T$_c$ [°C], the location of the B$^{4+}$ cation does not coincide with the center of the oxygen octahedron, resulting in a permanent electrical dipole moment [11, 20]. The stress on, or the electrical state of, the material can change the magnitude and direction of this dipole, which directly leads to the material's piezoelectric property. Figure 1.5 clearly shows the presence of a dipole moment for a perovskite unit cell below its *Curie* temperature.

When piezoelectric ceramics are sintered and cooled below their *Curie* temperature, regions with aligned dipoles will be created within the grains, commonly referred to as *Weiss* domains [20, 21]. However, due to the random distribution of grains and *Weiss* domains, there is no net polarization (and hence no piezoelectric effect) over the entire material. By consequence, the ceramic has to be poled to align the dipoles in one direction, the poling or 3-axis
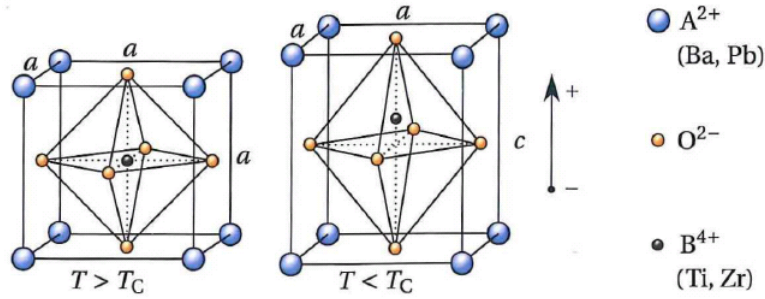
**Figure 1.5:** Cubic and tetragonal perovskite unit cell above and below the *Curie* temperature ($T_c$), respectively. Obtained from [11].

direction (see Figure 1.3), by applying a strong electric field (typically in the order of 1 to $3\frac{kV}{mm}$ at an elevated temperature ($<T_c$)) [11, 20].

PZT is available in a 'soft' and 'hard' version depending on its doping treatment[6] [11]. Soft PZT is commonly applied for sensing and energy harvesting applications due to its superior piezoelectric coupling efficiency with respect to its hard counterpart [11]. However, for high frequency resonant energy harvesting devices, hard PZT might be preferred as its high mechanical quality factor may compensate for the loss in electromechanical coupling efficiency as discussed in Section 1.3.1 [3].

**Piezoelectric polymers**

Several polymeric materials, including polyvinylidene fluoride (PVDF), polyacrilonitrile (PAN), and polyvinylidene vinylacetate (P(VDCN-VA)), are known to exhibit piezoelectric properties [9, 11, 22]. Since the seminal piezoelectric characterization of PVDF by *Kawai* in 1969, PVDF ($CH_2$-$CF_2$) has become the dominant polymeric piezoelectric material system [10, 22, 23]. The semi-crystalline PVDF can occur in various phases ($\alpha$, $\beta$, $\gamma$, $\delta$) depending on the configuration of the chain links [24]. For the $\beta$-phase, the chain configuration results in a net dipole moment resulting in the piezoelectric capability of crystalline $\beta$-phase PVDF. The $\beta$-phase can be obtained by stretching or annealing the non-piezoelectric $\alpha$-phase material. Moreover, PVDF is often blended with a second polymeric material such as trifluoroethylene to enhance the crystallinity, and therefore the piezoelectric properties, of the resulting copolymer [11, 22].

---

[6]For soft PZT materials some of the $A^{2+}$ and/or $B^{4+}$ sites in the perovskite crystal unit cell (see Figure 1.5) are replaced by three valent and/or five valent cations (donor doping), respectively, resulting in cationic vacancies at the A and/or B sites to maintain overall charge neutrality. Consequently, the domain walls of these soft piezoceramics are less hindered to move, which causes the poling process to be more efficient. Moreover, piezoceramics with high coupling factors, though lower mechanical quality factors are produced by this doping treatment [11, 13]. Contrarily, for hard PZT, some of the $B^{4+}$ cations are replaced by lower valent cations (acceptor doping), resulting in 'pinned' domain walls. Consequently, the poling treatment is more difficult (high electric fields are required) and materials with high mechanical quality factors, though low coupling factors are achieved [11, 13].

**Piezoelectric composites**

Similar to structural composites such as glass fiber reinforced polymers (GFRPs), piezoelectric composites can be produced with a tailored, unique set of piezoelectric, mechanical, and electrical properties. Most two phase piezoelectric composites consist of a ceramic piezoelectric (active) material such as PZT loaded into a (passive) polymer matrix [25]. The connectivity pattern of the active and passive phase highly influences its piezoelectric and processing properties [26, 27]. An overview of the 10 possible connectivity schemes and corresponding notations of two phase composites is depicted in Figure 1.6.

Production of 0-3 composites, whereby piezoelectric particles are randomly dispersed in the polymer matrix, is the most straightforward and, by consequence, the less costly method to manufacture piezoelectric composites. However, piezoelectric properties of random particulate composites are significantly lower than the best performing pristine polymeric or ceramic piezoelectric materials [25].

Composites with a 1-3 connectivity pattern, commonly produced by the 'dice and fill'[7] or 'arrange and fill'[8] method, are known to have superior performances with respect to random particulate composites, yet they come with high production costs and can suffer from performance degradation after a certain number of loading cycles [2, 29].

An interesting alternative to standard 0-3 and 1-3 piezoelectric composites, are the quasi 1-3 composites with piezoelectric short fibers (or particles) structured in the host matrix by means of the dielectrophoresis process (DEP), known as DEP structured fiber composites (SFC) [11, 25]. These quasi 1-3 composite can be produced with piezoelectric properties close to conventional 1-3 composites but with a more straightforward and cost-effective production process [25].
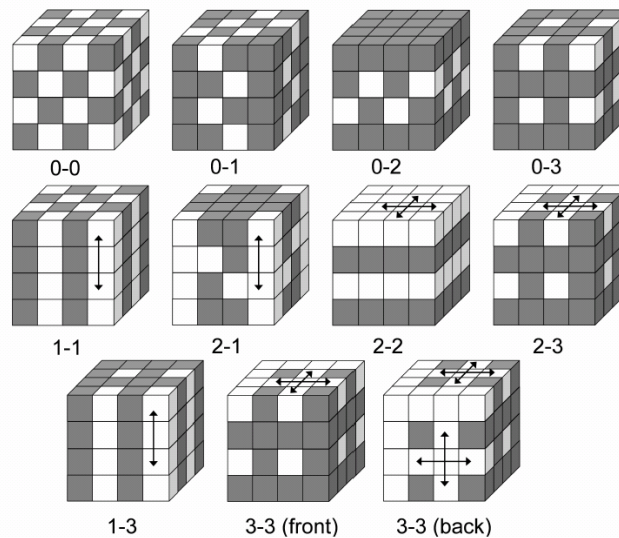


**Figure 1.6:** Overview of the possible connectivity schemes between the active (white) and passive (dark) phases of two phase piezoelectric composites. Obtained from [26], adapted from [27].

---

[7]'Dice and fill' 1-3 composite are made by dicing a poled piezoelectric ceramic block or plate after which the resulting gaps are filled with an uncured polymer [11, 20].

[8]'Arrange and fill' 1-3 composites are obtained by placing piezoelectric ceramic fibers in a mould (regular or random) after which an uncured polymer is injected. The poling treatment is performed after the polymer is cured [28].

## 1.2   Piezoelectric energy harvesting systems

Prior to presenting the PEH figures of merit, one has to know the main 'building blocks' or modules of such a PEH system. *Rödig et al.* identified five fundamental modules: the mechanical energy source (i), mechanical transformer (ii), the piezoelectric transducer element (iii), the power transfer circuit (iv), and the electrical energy storage management (v) (see Figure 1.7) [30].
Although electronics are included in Figure 1.7 to present the complete picture of a typical PEH system, only the first three modules (i-iii) are treated in this thesis as the harvester's electronics (circuit and storage) is considered beyond the scope of the MSc. thesis research project.
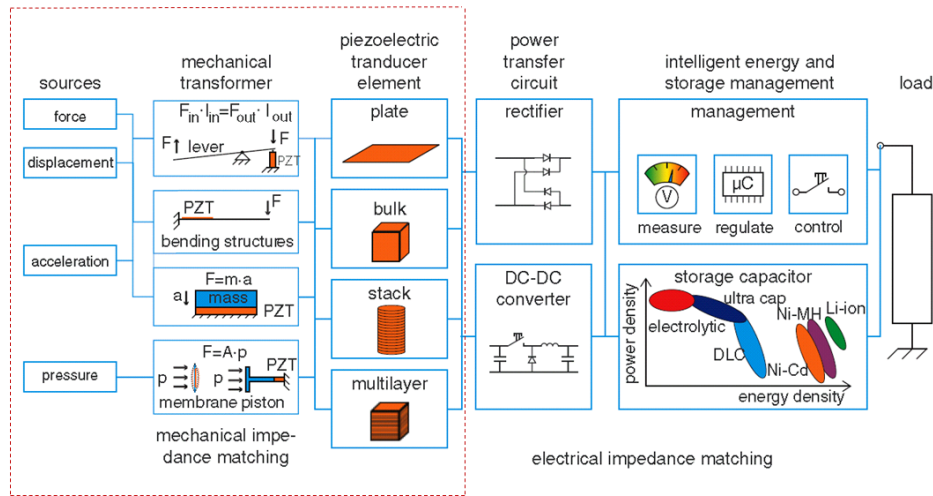


**Figure 1.7:** Overview of main modules of a typical piezoelectric energy harvesting system. This thesis focuses on the first three modules as demarcated by the dashed red rectangle. Adapted from [30].
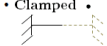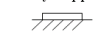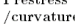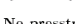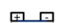
Figure 1.7 gives a basic overview of the main 'building blocks' of a typical PEH system. Though, a more detailed analysis of modules (i), (ii), and (iii) of Figure 1.7 is required to understand the effect of the PEH design choices on the final PEH performance.
An attempt to disentangle the web of the various piezoelectric energy harvester design configurations reported in the literature led to the generation of the design synthesis chart depicted in Figure 1.8. Each column of the chart represents a main design feature with two or more design options/elements. In this way, the majority of the energy harvesters configurations can be reconstructed by connecting the options of each design feature. Note that there is a strong interdependency between the various categories as is prevalent from the following brief overview of the PEH design features and corresponding options:

- **Planform geometry**
  PEH design configurations come in various shapes of which the rectangular (cantilever type) is by far the most common. Several studies have indicated the beneficial effect of changing the rectangular geometry into a triangular or trapezoidal one as a non-uniform width alters the span-wise strain distribution [2,31]. Henceforth, higher power densities can be achieved [32].
  Most circular shaped designs are developed for (quasi) static load cases operated by human touch or differential pressure loading scenarios [33–35].

| Planform Geometry | Mechanical Boundary Conditions | Initial Conditions | Piezo- Substrate Design | Electrode Design | Material Operation | Load Introduction | Load Case |
|---|---|---|---|---|---|---|---|
| Rectangular • | • Clamped • | • Prestress • /curvature | • Unimorph • ($n_a = 1$) | • PPE • | • $d_{31}$ • | • Direct Excitation • | • Static |
| Circular • | • Simply supported • | | • With SS • | | | | • Quasi Static |
| Triangular • | | • No presstress • /curvature | • Bimorph • ($n_a = 2$) • W/O SS • | •IDE • | • $d_{33}$ • | • Inertial Motion • | • Dynamic (vibrational) |
| Trapezoïdal • | • Fully supported • | | • Multilayer • ($n_a > 2$) | | • $d_{15}$ • | | |
| | | | • Bulk/MSA • | | | | |

**Figure 1.8:** Piezoelectric energy harvester design synthesis chart of the three demarcated modules of Figure 1.7. Each column represents a main design feature for which the most commonly applied design elements/options are shown. MBC = Mechanical Boundary Condition, MSA = Multilayer Stack Actuator, SS = Substrate, PPE = Parallel Plate Electrodes, IDE = Interdigitated Electrodes, $n_a$ [−] = Number of active material layers.

- **Mechanical boundary conditions (MBC)**
  The three most frequently adopted mechanical boundary conditions are the clamped, simply supported, and fully supported conditions. Boundary locations with clamped boundary conditions imply zero displacements and slopes, whereas for simply supported conditions the displacements and moments are zero [36]. For fully supported conditions, the piezoelectric harvester (patch) is entirely attached to its host structure such that its displacements are governed by the occurring strains in the host structure[9].

- **Initial conditions**
  More exotic PEH designs can be obtained by applying initial conditions such as 'prestress' or 'prestrain' in the active material. An example is the dimorph configuration used for an energy harvesting shoe concept as proposed by *Paradiso et al.* [37]. Application of these initial conditions can result in beneficial stress and strain distributions (e.g. lower peak stresses or deflections) during operations as well as the additional availability of natural frequency tuning mechanisms at the cost of an increased production process and modelling complexity [9, 37, 38].

- **Piezo-substrate design**
  The amount ($n_a$ [−]) and thickness of the (active) piezoelectric layers as well as the amount, thickness, and material of the (passive) substrate layer(s) are critical parameters for the design of a piezoelectric energy harvesting system [2]. If the harvester contains solely one piezoelectric layer ($n_a$=1), often supported by a substrate layer, it is known as a 'unimorph' configuration. A second popular design configuration is the 'bimorph', for which two piezoelectric layers ($n_a$=2) are employed.
  Harvesters with a unimorph or bimorph configuration are by far the most common [2, 4, 10]. 'Multimorph' ($n_a$ >2) configurations are scarce in the literature as the increased complexity (modelling, manufacturability, ...) in many cases does not compensate for potential performance improvements (e.g. lower natural frequencies) [2, 39].
  Lastly, instead of the popular layer based configuration, a bulk (or stack) configuration can be applied for the design of the harvesting system. For a (multilayer) stack configuration the positive and negative electrodes are alternatively located/stacked in the bulk material. This modification of the straightforward bulk design is primarily convenient for actuation rather than energy harvesting or sensing purposes as a conveniently (low) operational voltage can be achieved by decreasing the distance between the electrode

---

[9]The fully supported mechanical boundary condition refers to strain-driven harvesting operations as explained in Section 1.3.1.

plates [11].

- **Electrode design**
  The most common electrode pattern is the parallel plate electrode (PPE) design. Similar to a parallel plate capacitor, where the dielectric medium is located between two electrode plates, the piezoelectric layer is sandwiched between an bottom and top electrode. An alternative to the conventional PPE lay-out, is the interdigitated electrode (IDE) design which is extensively discussed in Chapter 2.

- **Material operation**
  PEHs are designed to operate on one of the prevalent piezoelectric material operation modes ($d_{31}$, $d_{33}$, and $d_{15}$), as discussed in Section 1.1.2.

- **Load introduction**
  An optimal piezoelectric harvester design can only be achieved when the harvester is adapted to the anticipated loading scenario [2,3,9]. Most PEH are based on one of the two basic methods to couple the mechanical excitation to the harvesting system [10]. The first way is to create strain in the active material as a result of the harvester's inertial motion to base excitations.
  The second method is to introduce the mechanical input strain or force on the harvester by directly transferring the load to the harvester's conversion material (direct excitation method).

- **Load case**
  The majority of the energy harvesting applications are developed for dynamic (vibrational) load cases as a high energy output can be achieved when the piezoelectric system operates at its resonance frequency [2]. Consequently, most dynamic energy harvesting devices are designed to operate at one specific resonance frequency which can be tuned in accordance to the vibrational spectrum of their operating environment[10].
  Next, quasi static operations can be characterized by low frequency ($<5Hz$), off-resonance mechanical excitation scenarios.
  Lastly, for static energy harvesters, the mechanical excitation is a short duration, non-repetitive force or strain. Strictly speaking, they can be seen as energy harvesters in the purest sense as energy is generated only once and not (semi-)continuously which is the case for (power) harvesters developed for dynamic and quasi static load cases.

---

[10]A classic example is the addition of a (variable) tip mass to a cantilever bi- or unimorph design configuration [3].

## 1.3    Piezoelectric energy harvesting figures of merit

Piezoelectric energy harvesting figures of merit (FOMs) can be used to assess and compare the performance of one or more PEH designs. In literature, two categories of FOMs are frequently applied (see Figure 1.9). On the one hand one can use the fundamental material system FOMs to define the performance of employed piezoelectric material systems. On the other hand, one has to apply the overall PEH system FOMs to quantify the performance of the PEH design. These two categories are discussed in detail in the two coming subsections.
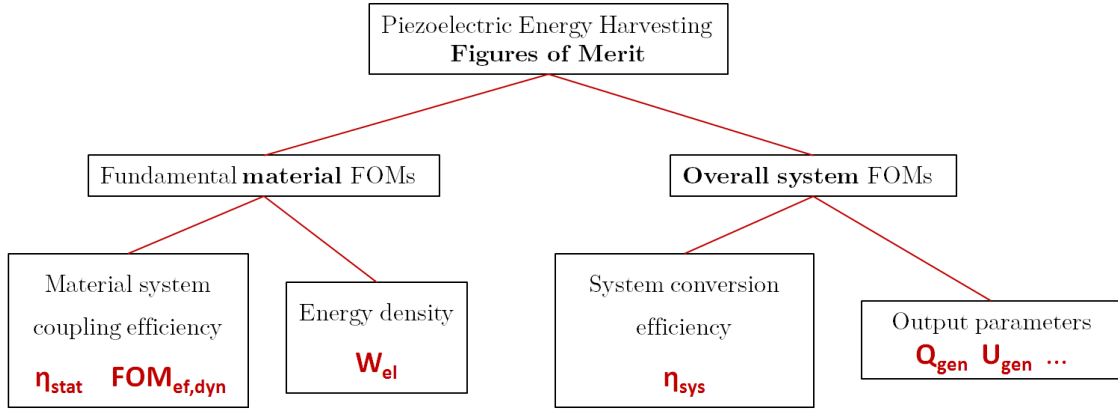


**Figure 1.9:** The two piezoelectric energy harvesting figures of merit categories.

### 1.3.1    Material system figures of merit

The first fundamental material system figure of merit is the (static) electromechanical conversion efficiency $\eta_{stat}$ $[-]$. In Section 1.1.1 this parameter was defined by Equation 1.5 and 1.6. Hence, $\eta_{stat}$ $[-]$ is formulated by Equation 1.10.

$$\eta_{stat} = \left.\frac{\text{Mechanical energy converted to electrical energy}}{\text{Input mechanical energy}}\right|_{static} = k^2 = \frac{d^2}{s^E \epsilon^{a,T}} \qquad (1.10)$$

Most piezoelectric energy harvesters are designed to operate at resonance to increase their efficiency [2, 3, 9]. For these kind of loading schemes, one has to apply a different efficiency figure of merit, $FOM_{ef,dyn}$ $[-]$, for which the effect of the resonance excitation conditions is included by the mechanical quality factor $Q_m$ (see Equation 1.11) [40].

$$FOM_{ef,dyn} = \left.\frac{\text{Mechanical energy converted to electrical energy}}{\text{Input mechanical energy}}\right|_{resonance} = k^2 Q_m = \frac{d^2 Q_m}{s^E \epsilon^{a,T}}$$
$$(1.11)$$

Moreover, for energy harvesting applications, it is useful to determine the generated electrical energy per volume or energy density $W_{el}$ $\left[\frac{J}{m^3}\right]$ irrespective of the efficiency at which this output energy is produced. For the correct interpretation of this figure of merit one has to make a distinction between stress-driven operational conditions (for which the combination of the mechanical induced stress and the compliance of the piezoelectric material determines the resulting strain) or strain-driven energy harvesting applications (for which the strain of the piezoelectric material is ruled by the external strain of the host structure) [30]. Henceforth, $W_{el}^T$ (Equation 1.12) describes the material's energy density for stress-driven application, whereas $W_{el}^S$ (Equation 1.13) should be applied for strain-driven applications.

$$W_{el}^T = \frac{1}{w_{el}^T}T^2 = \frac{d^2}{\epsilon^{a,T}}T^2 = dgT^2 \tag{1.12}$$

$$W_{el}^S = w_{el}^S S^2 = \frac{d^2}{\epsilon^{a,T}s^E s^D}S^2 = \frac{k^2}{s^D}S^2 \tag{1.13}$$

Where in Equation 1.12 and 1.13, $w_{el}^T$ $[\frac{m^3}{J}]$ and $w_{el}^S$ $[\frac{J}{m^3}]$ are the stress and strain energy density constants, respectively, quantifying a material's energy density independent of the actual strain or stress acting on the material.

Based on these fundamental material system FOMs one can investigate the relative performance of piezoelectric materials for energy harvesting purposes. Figure 1.10 summarizes the results of such a material performance evaluation study for two stiff and brittle piezoelectric ceramics (PZT4 and PZT5A) and one compliant and tough piezoelectric polymer (PVDF). Note that for $W_{el}^T$ and $W_{el}^S$ the failure (ceramics) or yield (polymer) stresses/strains are taken into account. Due to the lack of reported shear failure properties, the $d_{15}$ mode could not be included in the $W_{el}$ comparison graphs.

The materials performance evaluation study, summarized in Figure 1.10, demonstrates the advantages and drawbacks of compliant (polymeric and to some degree composites) versus stiff (ceramics) piezoelectric materials for energy harvesting applications:

- The electromechanical coupling efficiency of ceramic materials is superior to PVDF (Figure 1.10a and b). However, since compliant piezoelectric material systems are characterized with high mechanical losses, this effect is more pronounced for dynamic energy harvesting applications.

- When the material loading limits are not taken into account ($w_{el}$), the compliant PVDF is most suitable for stress-driven applications (Figure 1.10c and f). However, when failure (ceramics) or yield (polymer) stresses/strains are included for $W_{el}$, the performance of PVDF compared to the ceramics is better for strain-driven conditions with respect to stress-driven conditions (Figure 1.10e and f).

- In general, employment of the $d_{33}$- or $d_{15}$-mode enables higher energy efficiencies and density (constants) compared to $d_{31}$-mode operations.
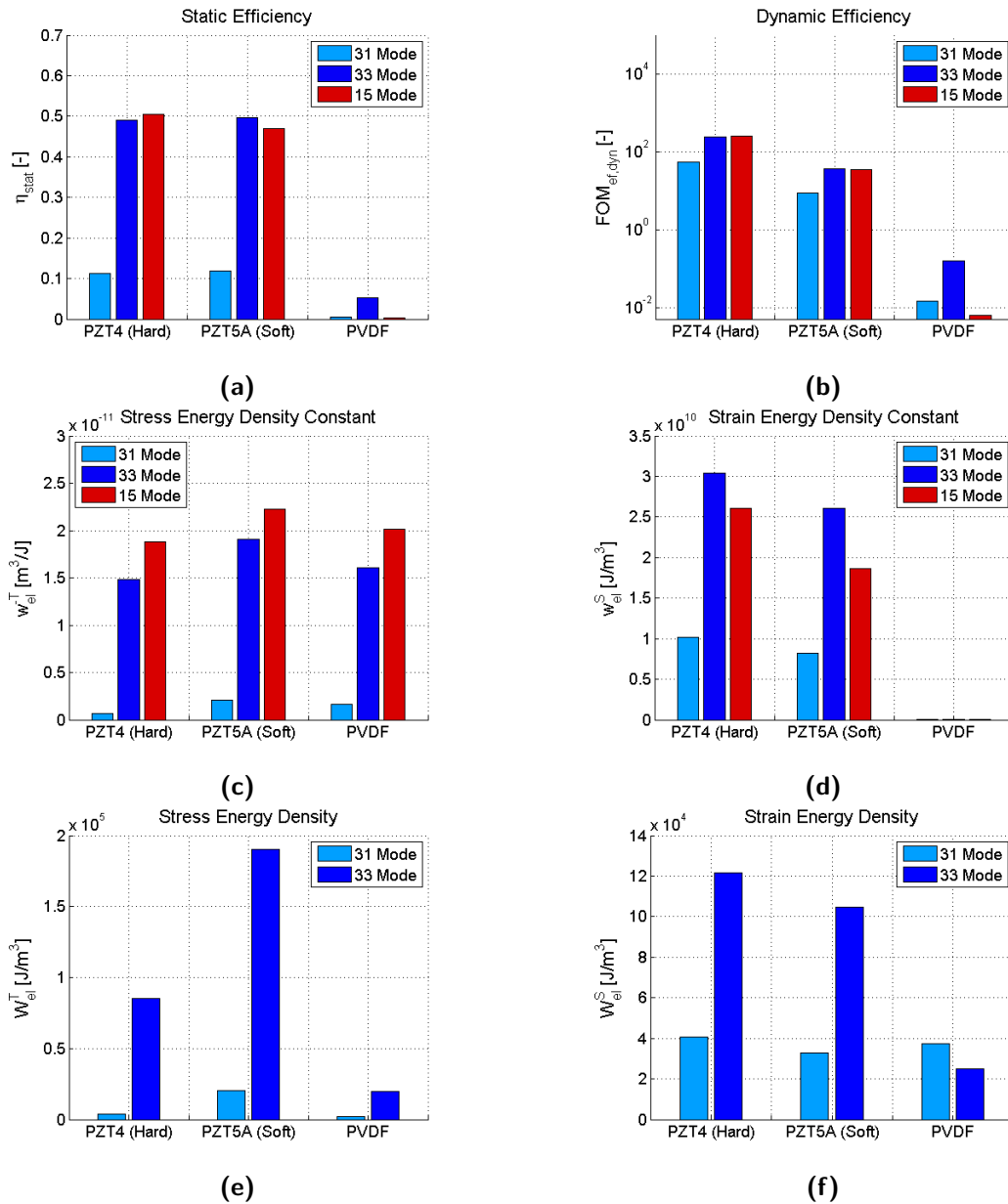
**Figure 1.10:** Performance study of three piezoelectric materials (PZT4, PZT5A, and PVDF) for energy harvesting purposes: static efficiency (a), (dynamic) resonance efficiency (b), stress density energy constant (c), strain energy density constant (d), stress energy density (e), and strain energy density (f). Material property sources: PZT4 ( [14, 41] ), PZT5A ( [14, 41] ), and PVDF ( [42–44] ).

### 1.3.2 Overall system figures of merit

The fundamental material FOMs discussed above allow comparison of the various piezoelectric materials for given harvesting applications. However, when designing a PEH system, one has to assess its performance as defined by the (interaction of the) various PEH system's design features (see Section 1.2).

#### System figures of merit

The first overall system of merit is the PEH system efficiency $\eta_{sys}$ $[-]$, relating the mechanical input energy to the final generated electrical energy. Closed-form expressions for $\eta_{sys}$ are highly dependent on the harvester design configuration and loading schemes. However, *Richards et al.* derived a general expression for the system efficiency valid for a PEH operating at resonance as described by Equation 1.14 [16].

$$\eta_{sys,dyn} = \frac{\frac{k_{sys}^2}{2(1-k_{sys}^2)}}{\frac{1}{Q_{m,sys}} + \frac{k_{sys}^2}{2(1-k_{sys}^2)}} \tag{1.14}$$

Where in Equation 1.14, $k_{sys}$ $[-]$ and $Q_{m,sys}$ $[-]$ are the system's coupling and quality factor, respectively, which can both be quantified by equivalent circuit theory [16].

Besides the PEH's system efficiency, characteristic output parameters can also serve as useful overall system FOMs. The most obvious ones are the generated power $P_{out}$ $[W]$ or energy $U_{gen}$ $[J]$, for dynamic or static loading schemes, respectively.
Moreover, the generated voltage $V_{gen}$ $[V]$ and/or charge $Q_{gen}$ $[C]$ can be applied as assessment figures as certain harvesting applications require maximal or minimal voltage and/or charge figures. For (quasi) static loading conditions, $U_{gen}$, $V_{gen}$, and $Q_{gen}$ are related to each other as described by Equation 1.15 [45, 46].

$$U_{gen} = \frac{1}{2} V_{gen} Q_{gen} \tag{1.15}$$

Moreover, $V_{gen}$ and $Q_{gen}$ are related to the harvester's free capacitance $C_{free}$ $[F]$ (Equation 1.16), which can be a applied as a system characteristic FOM too [46].

$$Q_{gen} = C_{free} V_{gen} \tag{1.16}$$

The aforementioned FOMs can be tailored for specific harvesting applications. For example, for weight and/or volume restricted application fields, one can rationalize the FOMs of interest to the harvester's mass and/or volume.

## 1.4   Scope and outline of this thesis

To examine the opportunities of compliant piezoelectric material systems for energy harvesting purposes, it has been shown that:

- Compliant piezoelectric materials are most appropriate for (quasi) static (off-resonance) mechanical loading schemes due to their relatively low mechanical quality and coupling factors. Moreover, they are well suited for high strain-driven loading schemes.

- PEH concepts based on the material's shear (or $d_{15}$) mode allow for high energy efficiencies and densities. However, reported shear material properties are scarce, in particular for compliant (composite) materials.

- The combination of material properties, loading conditions, as well as design characteristics such as the electrode lay-out determine the final performance of a PEH device.

- Several output parameters, included but not limited to the generated energy $U_{gen}$ and charge $Q_{gen}$, can be used to quantify and optimize a PEH's performance. For weight restricted applications (e.g. aerospace), one can optimize for mass and/or volume normalized objective functions.

Consequently, the two major research hypotheses are formulated as follows:

  *1.*   *'Do piezoelectric (0-3 and 1-3) composites exhibit shear coupling properties and how can they be quantified?'*

  *2.*   *'How does a shear strain-driven composite piezoelectric energy harvesting patch perform in terms of generated energy with respect to normal strain loading conditions?'*

These two hypotheses are the key drivers for this MSc. research project as described in the two coming chapters. The first research question is investigated in Chapter 2 by focusing on the characterization of shear piezoelectric properties of piezoelectric composite materials. Once the shear mode capabilities of these piezoelectric composite material systems is established, the performance of a flexible (piezoelectric composite) energy harvesting patch under shear strain-driven operations is assessed with respect to conventional axial loading schemes (Chapter 3). The main conclusions and recommendations for further research on this topic are summarized in the final chapter (Chapter 4).

# Chapter 2

# Shear mode characterization of piezoelectric composites

This chapter presents the shear mode characterization study on particulate and fiber piezo-electric composite material systems.

## 2.1 Introduction

To observe and quantify the shear properties ($s_{55}^E$, $\epsilon_{11}^T$, $d_{15}$, and $k_{15}$) of the aforementioned piezoelectric composites, a dedicated characterization strategy is developed. This introductory section commences with a detailed overview of the employed experimental measurement technique, after which the complementary (experimental and numerical) research steps are introduced.

### 2.1.1 Standard resonance-based $d_{15}$ measurement technique for PZT ceramics

The resonance-based measurement technique, as described in the American *IEEE Standard on Piezoelectricity (1987)* and the European *EN 50324-2 Standard (2002)*, has become a popular method for the characterization of piezoelectric properties[1] [15,48]. For this method, the electrical impedance of a piezoelectric sample is measured while it is excited by an alternating electric field ($\leq 0.01 \frac{V}{mm}$) for a predefined range of frequencies [48]. Due to piezoelectric transduction, elastic waves, with wavelengths proportional to the excitation frequency, will propagate through the sample. When the sample's geometry accommodates an odd[2] multiple of half a wavelength ($\lambda$ [$m$]), resonance will occur, distinctively affecting the measured impedance response [13, 49].

---

[1]Although the use of resonance or impedance-based characterization techniques can lead to under/overestimation of the actual piezoelectric properties due to e.g. unaccounted electrical/mechanical losses, it has become a well-accepted method for first order property quantification as other available methods, such as capacitance-based and quasi-static measurement techniques, can induce (at least as significant) errors [47,48]. When practically possible, it is recommended to combine the various methods to obtain the most accurate experimental electromechanical properties [13,15,49,50]. Therefore, quasi-static measurements are performed to complement the impedance-based experimental characterization study.

[2]Elastic waves with even wavenumbers do not result in resonance as the resulting positive and negative charges cancel each other due to mode symmetry [11,13].
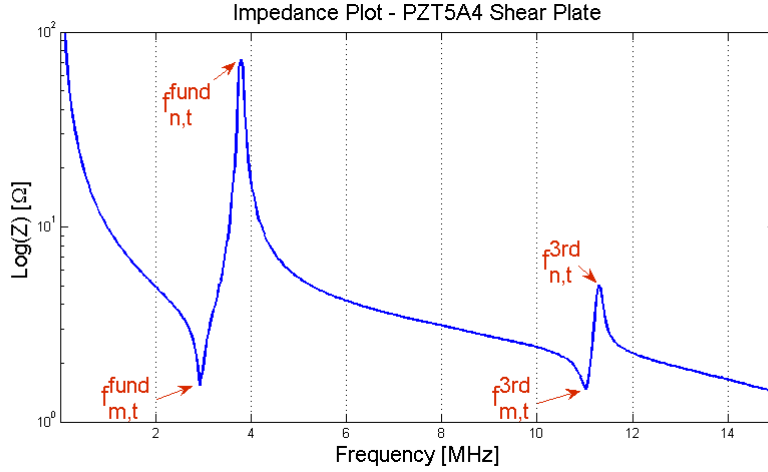
**Figure 2.1:** Experimentally obtained thickness impedance plot of a PZT5A4 shear measurement plate with properties summarized by Table 2.1 according to the experimental measurement procedure presented in Section 2.2.1.

One can plot the measured impedance data versus the applied excitation frequencies, resulting in a characteristic impedance plot. An example of such an impedance plot is illustrated in Figure 2.1, showing the experimental obtained impedance data of a thickness shear plate with properties defined in Table 2.1. On this plot, one can identify two pairs of resonance and antiresonance peaks corresponding to the fundamental and $3^{rd}$ overtone thickness shear resonance mode. Note that, in theory, resonance $f_r$ [$Hz$] and antiresonance $f_a$ [$Hz$] are defined as the frequencies at zero susceptance ($B$ [$\Omega$]) and reactance ($X$ [$S$]), respectively. $f_r$ and $f_a$ can be approximated by the series $f_s$ and parallel $f_p$ resonance frequencies of the representative electrical circuit, corresponding to the maximum of the real part of the admittance ($Y$ [$S$]) and impedance ($Z$ [$\Omega$]) [50].

In practice, it is much more convenient to determine the frequencies at minimum and maximum impedance ($Z$ [$\Omega$]) corresponding to $f_m$ [$Hz$] and $f_n$ [$Hz$], respectively, as shown in Figure 2.1 [15]. For low loss (high mechanical and electrical quality factor) piezoelectric materials with high electromechanical coupling factors, one can assume: $f_r \approx f_m \approx f_s$ and $f_a \approx f_n \approx f_p$ [11, 13, 49, 50].

Resonance and antiresonance frequencies are determined by the sample's geometry, material properties, and measurement boundary conditions as described by Equation 2.1 and 2.2, respectively [13].

$$f_{m,X}^i = \frac{iv_{jj}^E}{2X} = \frac{i}{2X\sqrt{s_{jj}^E\rho}} \quad \text{for } i=1, 3, 5, ... \tag{2.1}$$

$$f_{n,X}^i = \frac{iv_{jj}^D}{2X} = \frac{i}{2X\sqrt{s_{jj}^D\rho}} \quad \text{for } i=1, 3, 5, ... \tag{2.2}$$

Where in Equation 2.1 and 2.2, $f_{m,X}^i$ and $f_{n,X}^i$ are the resonance and antiresonance peak of the $i$-th mode[2], $v^E$ [$\frac{m}{s}$] and $v^D$ [$\frac{m}{s}$] are the elastic wave velocities for zero/constant electric field and charge boundary conditions, respectively, $\rho$ [$\frac{kg}{m^3}$] is the material's density, and X [$m$] is the sample's controlling dimension.

Besides the determination of purely mechanical properties such as the elastic compliance (see Equation 2.2 and 2.1), the (anti)resonance frequencies obtained from impedance measure-

| $t\ [m]$ | $w\ [m]$ | $l\ [m]$ | $\rho\ \left[\frac{kg}{m^3}\right]$ | $\epsilon_{11}^T\ [-]$ |
|---|---|---|---|---|
| $3.1{\cdot}10^{-4}$ | $1.2{\cdot}10^{-2}$ | $3.35{\cdot}10^{-2}$ | $7900$ | $1650$ |

**Table 2.1:** Key geometrical and material properties of the PZT5A4 shear measurement plate of which an experimentally obtained impedance plot is shown in Figure 2.1. The $t$, $w$, and $l$ dimensions are defined in Figure 2.2.

ments can be be used to quantify the piezoelectric coupling of a material sample. The exact procedure is dependent on the piezoelectric coupling mode under analysis. In the following paragraphs the impedance-based method for $d_{15}$-mode measurements is presented. For a comprehensive overview of the standard impedance-based measurements of different modes and sample geometries one can consult the *IEEE Standard on Piezoelectricity (1987)* or the book of *Jaffe et al.* [13, 15].

As discussed in Section 1.1.2, the $d_{15}$ mode governs shear around the axis perpendicular to the plane formed by the poling (3-) and electrode 1-axis. Hence, for shear mode excitation, the poling electrodes are only temporary and should be removed before application of the *final* electrodes which have to induce electric field lines perpendicular to the poling direction[3]. Consequently, a standard shear measurement sample has to be prepared as illustrated in Figure 2.2. A bulky piezoelectric ceramic block is produced and poled uniformly by parallel plate electrodes (PPE) (step 1). After poling, the temporary poling electrodes are removed and the block is sliced into plates along a cutting plane parallel to the poling axis (step 2). Next, the final PPE are applied on the samples' cutting planes such that, due to $d_{15}$-mode piezoelectric coupling, the resulting thickness shear plates will shear around the 2-axis (step 3).

To avoid cross-coupling of the thickness- and length- shear resonance modes, the length to thickness ratio ($\frac{l}{t}\ [-]$) has to be sufficiently high[4]. $\frac{l}{t}$ ratios proposed in the literature range from 3.5 to 10 [11, 13, 51, 52]. Hence, a minimum (conservative) $\frac{l}{t}$ ratio equal to 10 is consistently maintained for the work presented in this thesis.

Once the sample is prepared according to the aforementioned procedure, the impedance data is collected from which the fundamental (and overtone) (anti)resonance peaks can be derived.
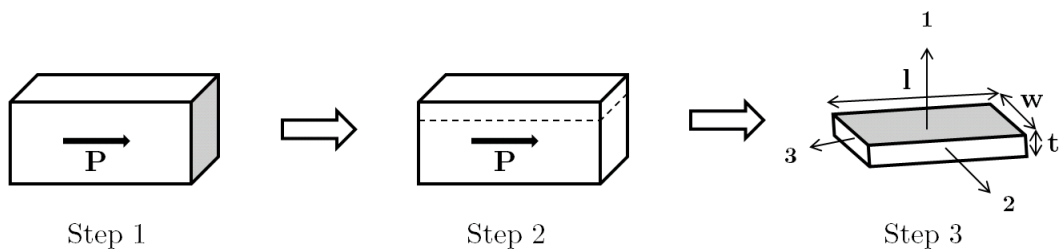


**Figure 2.2:** Preparation scheme of a piezoelectric ceramic thickness shear measurement sample.

---

[3]The complexity of this production production process is probably one of the main reasons why the shear mode is the least implemented one for industrial applications as well as the least investigated one in the piezoelectric literature.

[4]In contrast to earlier literature on this topic, *Cao et al.* demonstrated that the length to width ratio $\frac{l}{w}$ has no significant importance concerning the correct interpretation of the impedance spectrum for shear property characterization [13, 51].

Subsequently, one can apply Equation 2.3 to quantify the shear coupling factor[5].

$$k_{15}^2 = \frac{\pi}{2}\frac{f_m}{f_n}\tan\left(\frac{\pi}{2}\frac{f_n - f_m}{f_n}\right)$$ (2.3)

To compute the $d_{15}$ piezoelectric charge constant, one has to determine the zero stress relative permittivity $\epsilon_{11}^T$ by measuring the capacitance $C$ $[F]$ of the sample at a frequency below the fundamental resonance frequency at or below $1kHz$ [13, 51]. For the standard PPE shear measurement sample under analysis, $\epsilon_{11}^T$ is quantified by Equation 2.4.

$$\epsilon_{11}^T = \frac{Ct}{\epsilon_0 lw}$$ (2.4)

Where in Equation 2.4, $\epsilon_0$ $[\frac{F}{m}]$ is the absolute vacuum permittivity equal to $8.854...\cdot10^{-12}\frac{F}{m}$ [11].

Next, $d_{15}$ is determined by rewriting Equation 1.9 as presented in Equation 2.5.

$$d_{15} = k_{15}\sqrt{s_{55}^E \epsilon_{11}^{a,T}}$$ (2.5)

Where the shear elastic compliance $s_{55}^E$ in Equation 2.5 is obtained by use of Equation 2.1. As an example, the shear property values calculated according to the aforementioned procedure and based on the PZT5A4 shear plate impedance plot depicted by Figure 2.1 are given in Table 2.2. The experimentally obtained values are compared with the material properties reported by the manufacturer.

The (relatively small) discrepancy between the reported and measured properties can be attributed to the $f_r \approx f_m \approx f_s$ and $f_a \approx f_n \approx f_p$) approximation (inherent to impedance-based measurements) as well as ageing of the sample's piezoelectric properties[6] [49, 50].

|  | $k_{15}$ $[-]$ | $s_{55}^E$ $[Pa^{-1}]$ | $d_{15}$ $[\frac{C}{N}]$ |
|---|---|---|---|
| Measured | 0.67 | $4.39\cdot10^{-11}$ | $5.34\cdot10^{-10}$ |
| Reported | 0.69 | $4.50\cdot10^{-11}$ | $5.50\cdot10^{-10}$ |
| *RE [%]* | *3.3* | *2.5* | *2.8* |

**Table 2.2:** Experimentally obtained versus reported shear material properties of the PZT5A4 shear plate (RE = Relative Error). Reported data obtained from [14].

### 2.1.2 Novel resonance-based $d_{15}$ measurement method

The impedance-based measurement method, as presented in the previous section is a convenient and straightforward way for the characterization of shear mode properties of piezoelectric (ceramic) materials. However, if one wants to prepare a piezoelectric (particulate) composite according to the preparation scheme illustrated in Figure 2.2, two practical issues arise:

1. The required poling field for piezoelectric composites is significantly higher than for ceramics ($\sim 10\frac{kV}{mm}$ versus $\sim 2\frac{kV}{mm}$) [26]. If one wants to obtain a shear measurement sample with a $\frac{l}{t} \geq 10$ and realistic thickness, one has to apply an inconveniently high constant poling voltage of at least $100kV$.

---

[5]Equation 2.3 can be derived by solving the classic wave equation for a piezoelectric medium under constant induction as described by *Aurelle et al.* [52].

[6]The poling and manufacturing process of the example thickness shear measurement sample under analysis was performed $\pm7$ years prior to the execution of the reported impedance measurements.

2. When the bulky sample is produced according to the conventional particulate composite production method, an inhomogeneous particle distribution will be obtained due to sinking of the particles during the polymer's curing process.

To address these practical problems, a novel sample preparation method, adapted for the impedance-based measurement technique presented in Section 2.1.1, was developed. The main advantage of this new method is that it is well suited for the characterization of thin (particulate) piezoelectric samples as illustrated in Figure 2.3. First, the composite sample is produced[7] and uniformly poled by parallel plate electrodes (Step 1). Next, these temporary poling electrodes are removed after which the final IDE electrodes are applied (Step 2).

The proposed method employs interdigitated electrodes as depicted in Figure 2.4. For small finger widths ($w_f$ $[m]$), large finger spacings ($s_f$ $[m]$), and relatively thin samples, quasi-uniform field lines are obtained/induced perpendicular to the poling axis. In this way, a thickness shear measurement sample is obtained with reversed 1- and 3-axes with respect to the standard shear plate $d_{15}$ measurement sample illustrated in Figure 2.2.

Careful inspection of the IDE lay-out reveals that the orientation of the field lines in each cell opposes the one of the neighbouring cell. At first sight one may think the opposing thickness shear motion would impede the occurrence of resonance from which the shear mode properties are eventually derived from. However, elastic shear waves propagate, in contrast to longitudinal waves, perpendicular to the motion of the particles [53]. By consequence, standing shear waves excited by the alternating lateral electric field will occur. This is confirmed by *Milyutin et al.* who developed an IDE-based (AlN) thin film shear mode bulk acoustic wave resonator for gravimetric sensor applications[8] [54].



Step 1          Step 2
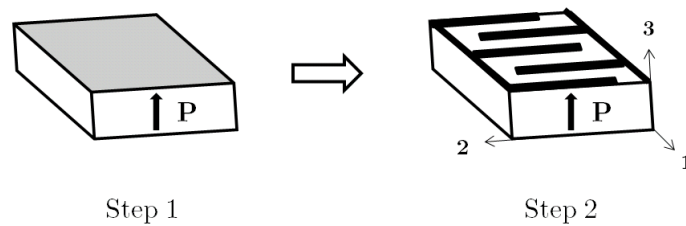
**Figure 2.3:** Novel IDE-based sample preparation scheme for the impedance-based shear mode characterization method presented in Section 2.1.1.

---

[7]The piezoelectric composite sample production method is discussed in Section 2.2.

[8]The occurrence of pure shear resonance modes by IDE excitation is also demonstrated by finite element simulations (Section 2.3.1).

**(a)**



**(b)**
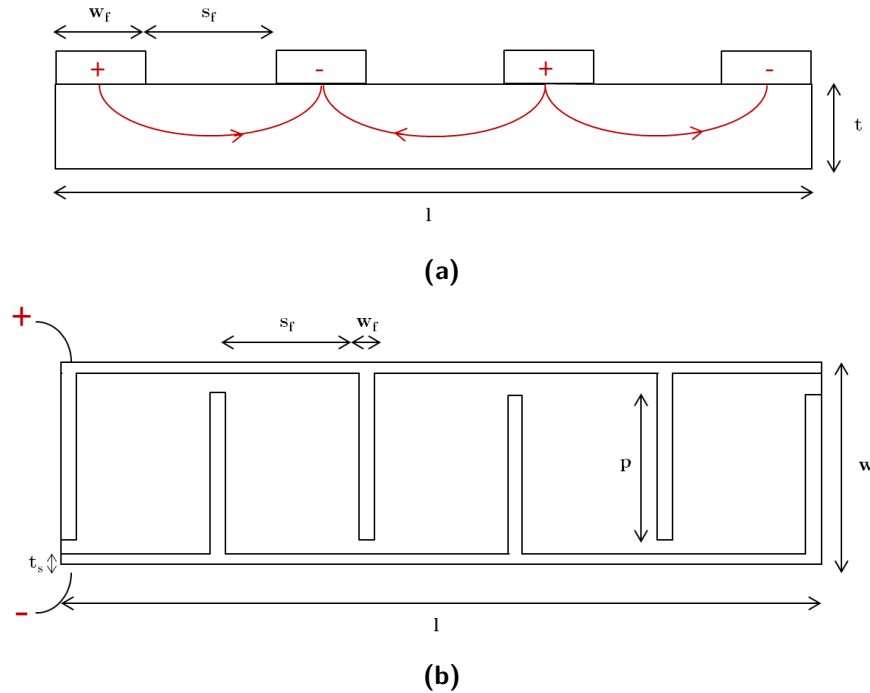
**Figure 2.4:** Generic interdigitated electrode lay-out: cross-sectional view (a) and top view (b). The red lines schematically indicate the direction of the electric field. Note that height of the electrode fingers is exaggerated for reasons of clarity.
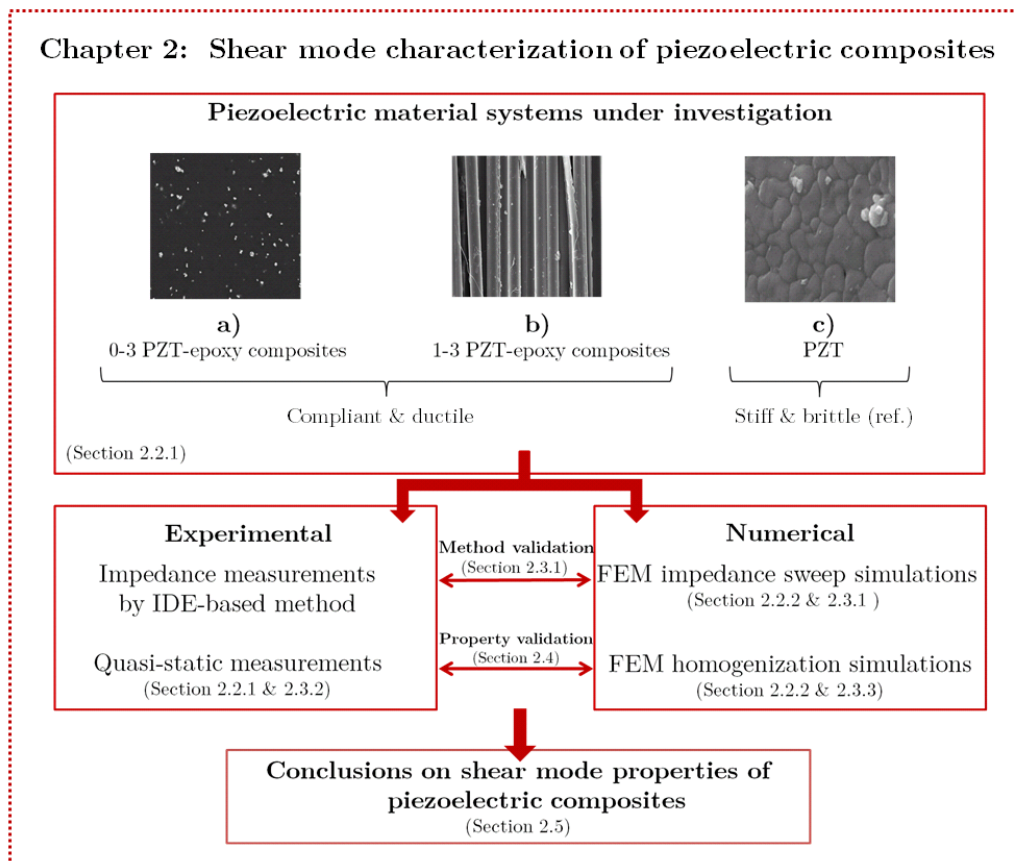


**Figure 2.5:** Graphical outline of Chapter 2. Micrographs obtained from [26, 55, 56].

### 2.1.3   Outline Chapter 2

An overview of this chapter's research 'route' is illustrated in Figure 2.5.

The shear mode properties of two phase piezoelectric composites with the same material components (PZT and epoxy) though different connectivity schemes (0-3 and 1-3) and PZT loading grades were investigated. Moreover, a monolithic PZT material was added for reference.

Samples were prepared and measured experimentally with the novel $d_{15}$ impedance-based measurement method, complemented with quasi-static measurements. Numerical (finite element) simulations were performed to validate the novel IDE-base measurement method and to obtain effective properties by implementation of a numerical homogenization technique.

Based on the experimental and numerical results, conclusions were drawn on the shear mode properties of the composite piezoelectric material systems under analysis.

## 2.2   Methods and materials

This section outlines the procedures concerning the shear property characterization study of the piezoelectric composite material systems. First, the experimental steps are discussed. Next, the set-up of the finite element models (FEMs) for the impedance and effective property simulations are presented.

### 2.2.1   Experimental measurements

Three piezoelectric material systems are investigated in this study: 0-3 (particulate) piezoelectric composites, 1-3 (fiber) composites, and plain piezoelectric ceramics. The preparation as well as the experimental characterization procedures of these materials are described in the coming sections.

#### 0-3 Composites

PZT-epoxy particulate composites were produced and prepared as described in the coming paragraphs.

PZT5A4 (Morgan Electroceramics, Ruabon, UK) powder was calcined (T=1150°$C$) for one hour and milled to micron particle size by $5mm$ Y-stabilized ZrO balls. The powder was subsequently sieved, dried for 12 hours at 150°$C$, and stored under vacuum conditions at room temperature.

Next, the powder was added to Epotek 302-3M epoxy (Epoxy Technology Inc., Billerica (MA), USA). At first, the PZT particles were mixed with the (diglycidyl ether of bisphenol-A) resin component for 5 minutes at $2500rpm$ with a *DAC 150 FVZ SpeedMixer* (Hauschild, Germany). Then the multi-functional aliphatic amine hardener was added to the PZT-resin mixture. After mixing for 5 minutes at $2500rpm$, the uncured composite was degassed in vacuum for 10 minutes.

**(a)**                                                                    **(b)**

**Figure 2.6:** Particulate composite preparation pictures: the *Balzers Union SCD40 Sputter-coater* (a), the poling set-up: DC generator (left), poling jig (central), and silicon oil bath (right) (b).

Particulate composite samples were cured to their final shape in two different ways.

For the impedance-based measurement method, rectangular samples were made by moulding the mixture in a rectangular Teflon mould and curing overnight at room temperature. Subsequently, the samples were released from the mould and post-cured at $100°C$ for $\pm 1$ hour. Parallel plate poling electrodes (Au) were deposited on the samples with a *Balzers Union SCD40 Sputter-coater* (Balzers, Liechtenstein) (Figure 2.6a). The samples were poled in a silicone oil bath at $100°C$ with an electric field of $10\frac{kV}{mm}$ for one hour (Figure 2.6b).

Next, the temporary poling electrodes were removed by wet sanding and the Au interdigitated electrodes were sputtered on top surface of the sample (Figure 2.7a). Copper tape was applied at the two end sides of the IDE to connect the sample with the leads of the impedance analyzer, introduced in the coming subsection on the characterization instruments.

Figure 2.7c shows the dispersion of the micron-sized PZT particles of an impedance measurement sample.

For the quasi-static piezoelectric charge constant measurement method, discs ($d_{33}$ and $d_{31}$) and ring ($d_{15}$) samples were produced by tape casting the PZT-epoxy mixture on an aluminium foil (see Figure 2.6b) [57]. Next, the discs (d=8mm, t=1mm) and rings ($d_{out}$=8mm, $d_{in}$=4mm, t=1mm) were punched out of the resulting slabs after curing at $100°C$ overnight. Solely the samples' top surface was electroded by the aforementioned gold sputtering method as the aluminium foil provided a conducting layer on the bottom surfaces. Next, the samples were poled in a silicone oil bath at $80°C$ with an electric field of $7.5\frac{kV}{mm}$ for half an hour[9].



**(a)**                                  **(b)**                                  **(c)**
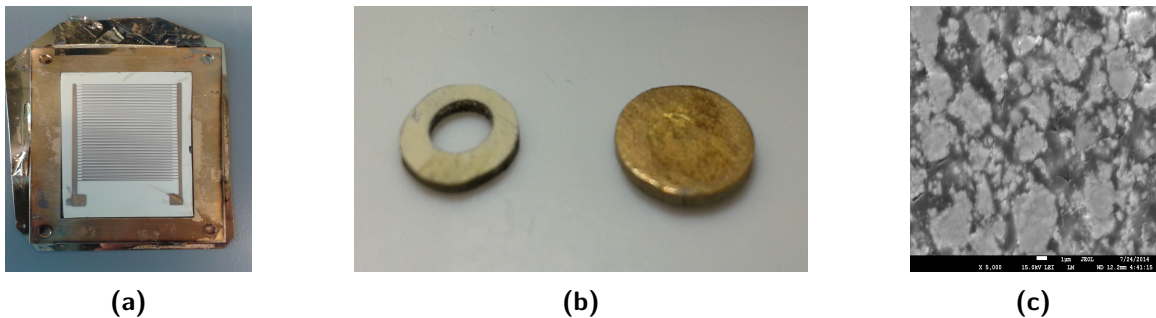
**Figure 2.7:** Particulate composite sample pictures: an injection moulded rectangular (impedance-based) measurement sample attached to the mask fixture after the IDE sputtering process (a), a ring and disc (quasi-static) measurement sample (b), a SEM micrograph of a $50vol\%$ PZT-epoxy particulate composite (c).

---

[9]The quasi-static measurements served to characterize the relative magnitude of the piezoectric charge constants ($d_{33}$, $d_{31}$, and $d_{15}$) at various PZT volume fractions rather than to demonstrate their maximum values at optimum poling conditions. Henceforth, a conservatively low poling field and temperature was consistently

Subsequently, a gold layer was sputtered on all surfaces of the ring-shaped samples. The layer on the top and bottom surfaces was removed to obtain radially electroded (and thickness-poled) rings conform the $d_{15}$ quasi-static testing procedures, as discussed in Section 2.2.1 (see Figure 2.7b).

### 1-3 Composites

Two kinds of fiber (SP53-epoxy) composite samples were obtained from Smart Materials GmbH (Dresden, Germany). The first set of samples have a thickness of $1.54mm$, a PZT filling grade of 0.48, and a fiber diameter of $800\mu m$. The second type of samples are characterized with a $0.30mm$ thickness, a filling grade of 0.65, and a fiber diameter of $250\mu m$. All samples were poled by the manufacturer in the thickness direction with CuSn parallel plate electrodes.

The samples were prepared for the IDE-based impedance method by removing the original PPE electrodes by wet sanding. Subsequently, gold IDEs were sputtered by the aforementioned process. Cu tape was applied for the impedance and capacitance measurements.

Quasi-static $d_{15}$ measurements were not performed for the fiber composite samples. One would either have to make measurement rings from the as-received composite fiber plates, accepting material losses and a high risk of breaking the labour-intensive composite material, or devise a production method to obtain homogeneous, thickness-poled and radially-electroded fiber composite rings conform the dimensions of the measurement device's sample holder as presented in the coming subsection on the employed characterization instruments[10].
These practical considerations stipulate once more the convenience of the novel impedance-based $d_{15}$ measurement method.

### Piezoelectric ceramics

Reference piezoelectric ceramic materials were investigated for four purposes: to perform a standard shear property impedance-based measurement as presented in Section 2.1.1 (i), to validate the numerical impedance simulations (ii), to calibrate the quasi-static $d_{15}$ measurements (iii), and to validate the novel IDE-based shear mode characterization strategy (iv).

A standard PZT5A4 shear plate measurement sample, with dimensions summarized in Table 2.1, was obtained from Morgan Electroceramics (Figure 2.8c). The impedance measurements were performed with the original nickel PPE. The electromechanical properties of the PZT5A4 material can be found in Appendix A.

Validation of the numerical impedance simulations were performed with PZ27 discs from Ferroperm Piezoceramics (Kvistgard, Danmark). The discs' thicknesses and diameters are equal to $1mm$ and $10mm$, respectively. The discs were poled (by the manufacturer) along their thickness dimension with silver electrodes applied at the bottom and top surfaces (Figure 2.8b). The electromechanical properties of the PZ27 piezoelectric ceramic material can be found in Appendix A.

---

applied for all the piezoelectric composite discs and rings to reduce the risk of short-circuiting the thin discs during the poling process.
[10]The former is considered beyond the scope of the research project.

Calibration of the quasi-static $d_{15}$ measurements, used to complement the impedance-based shear mode measurements, were performed with PZ27 rings and discs obtained from Ferroperm Piezoceramics. The discs are identical to the one described above, whereas the rings' thicknesses, inner and outer diameters are equal to $2mm$, $3.4mm$, and $5.5mm$ respectively. The rings were poled (by the manufacturer) along their thickness, while the electrodes are applied at the outer and inner surfaces as illustrated in Figure 2.8a.

For the validation of the IDE-based shear mode measurement method, PZT507 plates ($l=32.5mm$, $w=36.0mm$, and $t=0.199mm$, Morgan Electroceramics) were prepared according to the novel method. To ensure optimum (uniform) piezoelectric properties, the plates were re-poled with the original parallel plate electrodes at $2.5\frac{kV}{mm}$ for half an hour at $100°$C. Subsequently, the temporary poling electrodes were manually removed by wet sanding and dried at room temperature to evaporate remnant water. Gold IDE electrodes were applied on one surface by the aforementioned mask etch sputtering process.

Lastly, copper tape was applied at the two side electrode ends as shown in Figure 2.8d.



**(a)**



**(b)**



**(c)**



**(d)**
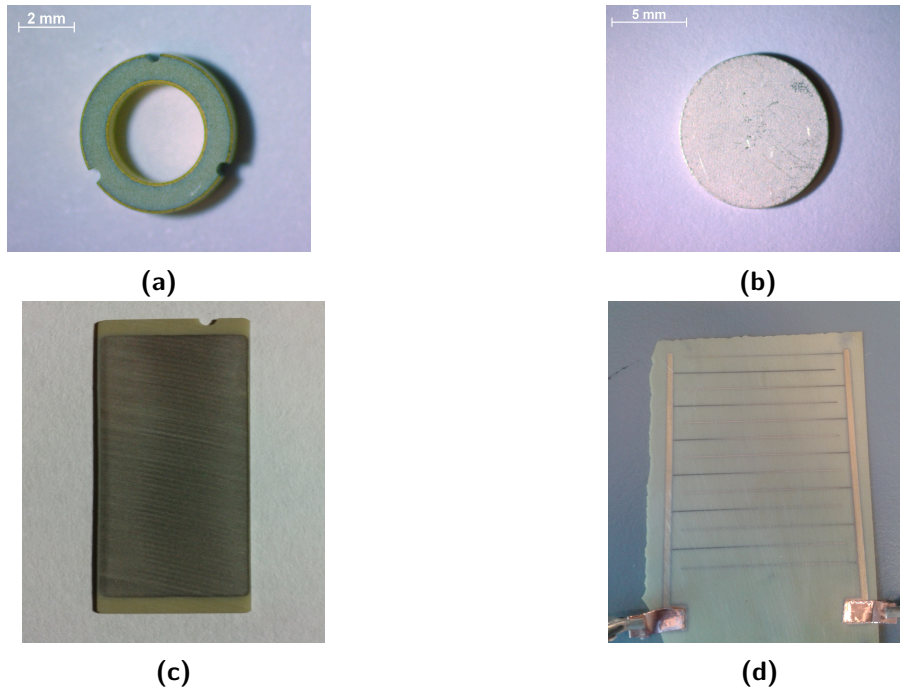
**Figure 2.8:** PZT reference samples: a PZ27 ring (a), a PZ27 disc (b), a PZT5A4 shear plate (c), and a prepared IDE-based PZT507 reference shear measurement plate (d).

### Characterization instruments

Several instruments were used for the experimental characterization of the samples described above:

- **Impedance measurements**
  Experimental impedance measurements were performed with a *HP4194A Impedance Analyzer* (Figure 2.9a).

- **Capacitance measurements**
  The samples' capacitance was measured with an *Agilent4263B LCR Meter* with a 1V potential at a fixed frequency of $1kHz$.

- **Quasi-static $d_{15}$ measurements**

  Quasi-static piezoelectric charge constant measurements were performed with a *PM300 PiezoMeter* (Piezotest, United Kingdom). The $d_{33}$ and $d_{31}$ were obtained with PPE discs, while the $d_{15}$ measurements require radially electroded, thickness-poled rings as shown in Figure 2.9b. All measurements were done with a dynamic excitation force of $0.25N$ (at a frequency of $110Hz$) and a $10N$ sample grip (static) force.

- **Imaging**

  A *JEOL JSM7500F* scanning electron microscope (SEM) served to observe the distribution of particulates within the prepared 0-3 composites. Prior to imaging, the composite samples were embedded into a room temperature curing epoxy (Figure 2.9c). Next, the imaging samples were coated with a thin conductive gold layer ($\pm 3nm$) by the aforementioned low-vacuum sputtering process.

  An optical microscope (*Zeiss Axiocam ERc 5s*) was used to measure the sub-millimeter dimensions of the various samples.



**(a)**          **(b)**          **(c)**
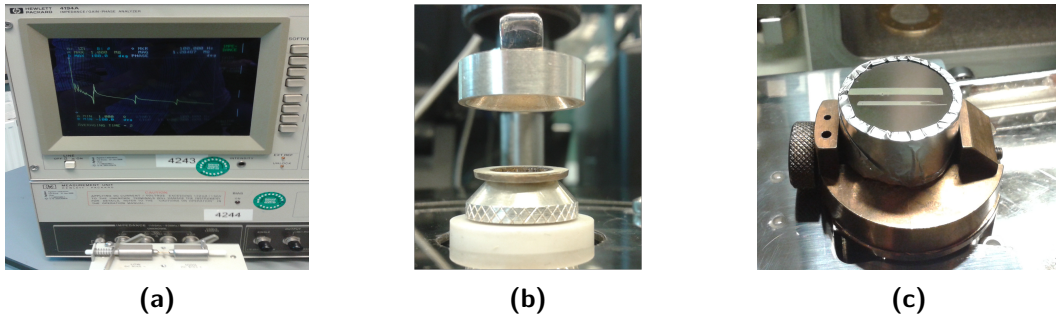
**Figure 2.9:** Experimental characterization pictures: the *HP4194A Impedance Analyzer* (a), the $d_{15}$ ring-shaped sample holder of the *PM300 PiezoMeter* with a particulate composite ring (b), and a prepared piezoelectric composite imaging sample in the *JEOL JSM7500F* sample fixture (c).

### 2.2.2   Numerical simulations

In addition to the experimental measurement procedures discussed in Section 2.2.1, numerical methods were employed to validate the novel IDE-base impedance measurement technique as well as to simulate the investigated composites' effective properties.

Consequently, two kinds of FEM simulations were performed in the *COMSOL Multiphysics®* (V4.4) environment, hereafter referred to as Comsol [58]. Impedance models were constructed and simulated with a *Frequency Domain Study* to validate the novel IDE-based impedance measurements. Next, the effective properties were studied by homogenization-based simulations by a *Stationary Study* approach.

**Impedance sweep FEM models**

As a first step towards simulating the frequency response of IDE-base samples by aid of a two dimensional FEM analysis, a straightforward parallel plate PZT disc model was constructed. Based on these results, two dimensional IDE-based models were set up conform the produced PZT and piezoelectric composite impedance measurements samples.

**Parallel plate disc model**

An experimental PZ27 disc sample was simulated by a two dimensional (plane strain) analysis

within Comsol's *Piezoelectric Devices* module[11]. The dimensions of the model corresponded to size of the experimental disc. The implemented electromechanical (PZ27) material properties can be found in Appendix A.

A frequency-dependent terminal voltage $(1V)$ was applied at the top boundary, while the lower boundary of the disc was provided with grounded electrical boundary conditions. The impedance $Z$ of the disc at each excitation frequency was obtained from Equation 2.6.

$$|Z(f)| = \frac{1}{|Y(f)|} \tag{2.6}$$

Where $Y$ is the simulated admittance of the piezoelectric disc between the ground and potential terminals of the Comsol model.

A mesh convergence study was performed to provide the model with a mesh size able to resolve the standing elastic waves at the resonance condition(s) of interest, while keeping the computational costs sufficiently low. With the standard rule of thumb of adopting a minimum number of five elements $(n)$ per wavelength in mind and focusing on the first fundamental thickness resonance frequency, the convergence study was performed by varying the amount of (triangular) elements per thickness $(\frac{n}{t})$ [49,59].

From Figure 2.10 it is clear that the numerically obtained fundamental thickness resonance $f_{m,t}^{fund}$ convergences to the experimental value for a minimum of three elements per thickness. Note that the impedance graphs plot the normalized impedance $(= \frac{Z}{Z_{f_{min}}})$[12] to be able to compare the (three dimensional) experimental and (two dimensional) numerical impedance data.

As half a fundamental wavelength is accommodated by the disc's thickness at $f_{m,t}^{fund}$, the aforementioned rule of thumb holds. Consequently, a minimum value of $\frac{n}{t}$ equal to $3mm^{-1}$ was consistently applied for the (IDE-based) shear impedance simulations presented in coming subsection.

**IDE-based thickness shear measurement model**

The IDE-based impedance FEMs serve to simulate (and validate) the frequency response of the experimental measurement samples prepared according to the novel IDE-based shear measurement method.

Based on the results of the PPE disc impedance simulations presented above, an adaptive two dimensional (plane) strain model was constructed in Comsol's *Piezoelectric Devices* module. The IDE fingers were simulated by applying alternating ground and terminal voltage $(1V)$ strips on a rectangular piezoelectric sample as illustrated in Figure 2.11. The dimensions of the model (sample thickness $(t)$, sample length $(L)$, IDE finger width $(w_f)$, and IDE finger

| $t$ [mm] | $L$ [mm] | $w_f$ [mm] | $s_f$ [mm] |
|:---:|:---:|:---:|:---:|
| 0.199 | 32.5 | 0.25 | 3.0 |

**Table 2.3:** Key dimensions of the validation (IDE-based) shear measurement impedance model.

---

[11]As a result, each node is characterized with 3 degrees of freedom (DOF): two displacements $(u,v)$ and one potential $(V)$.

[12]$Z_{f_{min}}$ refers to the measured/simulated impedance at the lower bound frequency.
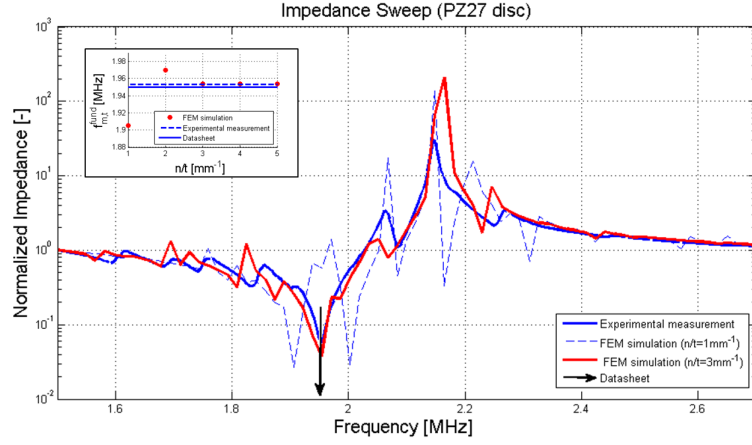
**Figure 2.10:** Mesh convergence figures for the PZ27 reference disc: experimental versus simulated ($\frac{n}{t}$=1$mm^{-1}$ and $\frac{n}{t}$=3$mm^{-1}$) impedance sweep at the fundamental (thickness) resonance frequency $f_{m,t}^{fund}$ and convergence of $f_{m,t}^{fund}$ with increasing number of elements per disc thickness (insert). The resonance frequency, based on the material properties reported by the manufacturer (Appendix A), is added for reference purposes [60].

spacing ($s_f$) as well as its bulk electromechanical material properties, can be adapted to the (experimental) sample of interest. The plate's piezoelectric material was assumed to be poled (uniformly) along its thickness.

As introduced in Section 2.2.1, the novel IDE-based impedance method was experimentally validated with an IDE PZT507 shear measurement plate. Consequently, the geometrical (Table 2.3) and material properties (Appendix A) of the experimental sample were implemented in the adaptive IDE model to obtain a representative IDE-based thickness shear measurement (validation) model (see Figure 2.11).
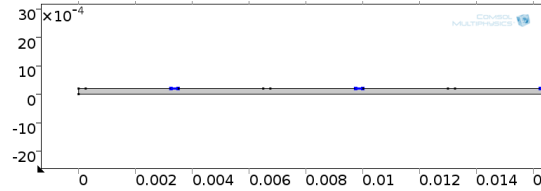


**Figure 2.11:** Image of (half of) the two dimensional IDE-based shear measurement model adapted to the experimental PZT507 shear measurement sample. The blue boundaries depict the IDE fingers provided with ground electrical boundary conditions.

**Homogenization-based FEM models**

Finite element simulations were performed to simulate the shear mode properties ($s_{55}^{E}$, $\epsilon_{11}^{T}$, $d_{15}$, and $k_{15}$) of the investigated piezoelectric material systems. By applying a numerical homogenization technique, the effective macroscopic electromechanical properties of the periodically structured composite material were determined by a microscopic analysis of a single representative volume element (RVE) [61, 62].

The homogenization-based simulations were performed with a two dimensional (instead of three dimensional) RVE to reduce the required computational cost. *Chambion et al.* have demonstrated that this simplification still results in accurate results when plane strain conditions are implied [63].
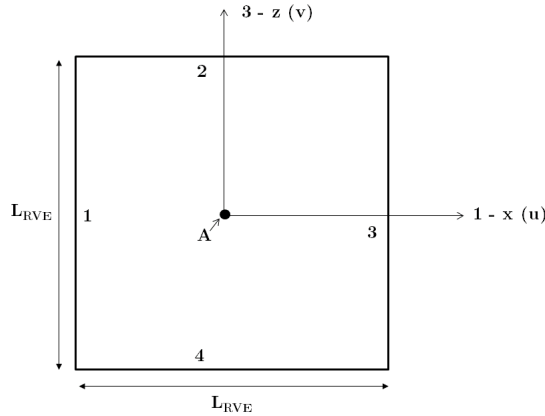
**Figure 2.12:** Representation of the generic two dimensional square RVE for the FEM homogenization simulations. The RVE's line boundaries are denoted by numbers 1 to 4, the node at the RVE's centroid by A.

A generic representation of the simulated RVE is defined in Figure 2.12. The RVE's boundaries are denoted by number 1 to 4, the center node is indicated with capital A. In this generic illustration, the RVE is presented as a bulk material without making a distinction between the two phases of the actual simulated composite materials.

The first of these investigated material systems is a 1-3 (fiber) composite with equally distanced PZT fibers oriented along the poling/thickness direction in a (non-piezoelectric) polymeric matrix. The second one is a 0-3 (particulate) composite material with equally distanced circular particles in a (non-piezoelectric) polymeric matrix of which the centroids are positioned at either the center or the corner of the RVE to study the effect of the defined particle location on the effective material properties. The PZT particles in the 0-3 composite are in reality randomly distributed within the polymeric matrix. However, equally distanced particles can be assumed for the effective property simulations when low PZT volume fractions (with relatively large inter-particle distances) are considered [61, 63].

The polymeric matrix is implemented as epoxy with electromechanical properties presented in Appendix A. Two piezoelectric (PZT) materials are simulated for the piezoelectric phase in accordance with the prepared experimental samples. The 1-3 composite is modelled with Sonox SP53 fibers (Appendix A), while the particles of the simulated 0-3 composite are assumed to exhibit PZT5A4 properties (Appendix A). The size of the RVE, defined by $L_{RVE}$, was adapted to realistic dimensions of the composite material: i.e. 1-3 composite: $L_{RVE}$=1$mm$, 0-3 composite: $L_{RVE}$=10$\mu m$ (assuming a mean particle size of ~4$\mu m$)[13]. Note that the PZT particles and fibers are assumed to be perfectly bonded to the polymeric matrix and that no particle interactions as well as interfacial effects are taken into account.

All homogenization simulations were performed within Comsol's *Piezoelectric Devices* module. The entire composite material was analysed as a piezoelectric material with strain-charge formulated constitutive equations. The piezoelectric phase was assumed to be poled (uniformly) along the RVE's 3-axis. Due to the required mesh adaptability concerning the various investigated PZT phase geometries and volume fractions, a physics-controlled, triangular element mesh was applied.

---

[13]Different PZT volume fractions were simulated by adapting the size of the PZT fibers (width) or particles (radius).

| Case | Property | BC | 1 | 2 | 3 | 4 | A |
|------|----------|-----|---|---|---|---|---|
| **I** | $s_{33}^E$ | MBC | – | $dv=\frac{+\epsilon_{33}^0 \cdot z}{2}$ | – | $dv=\frac{-\epsilon_{33}^0 \cdot z}{2}$ | – |
|       |            | EBC | $V=0$ | $V=0$ | $V=0$ | $V=0$ | – |
| **II** | $s_{55}^E$ | MBC | $du=Z\cdot\epsilon_{13}^0$ $dv=X\cdot\epsilon_{13}^0$ | $du=Z\cdot\epsilon_{13}^0$ $dv=X\cdot\epsilon_{13}^0$ | $du=Z\cdot\epsilon_{13}^0$ $dv=X\cdot\epsilon_{13}^0$ | $du=Z\cdot\epsilon_{13}^0$ $dv=X\cdot\epsilon_{13}^0$ | – |
|        |            | EBC | $V=0$ | $V=0$ | $V=0$ | $V=0$ | – |
| **III** | $d_{15}, \epsilon_{11}^T$ | MBC | – | – | – | – | $du=0, dv=0$ |
|         |            | EBC | $V=1$ | – | $V=0$ | – | – |

**Table 2.4:** Set of boundary conditions for each of the three cases investigated cases for the homogenization simulations. Note that '$X$' and '$Z$' refer to the coordinate of the nodes along the boundary line with respect to the center-located coordinate system defined by Figure 2.12 and the '$-$' symbol indicates symmetrical boundary conditions with respect to the opposite boundary line. (E/M)BC = (Electrical/Mechanical) Boundary Condition(s).

For the present shear mode property analysis, three sets of boundary conditions (cases) are required, as summarized in Table 2.4.

Case I allows one to determine the effective $s_E^{33}$ property of the material[14]. The RVE is strained uniformly ($\epsilon_{33}^0$=0.1) along the poling (3-)axis, whereas zero electric field electrical boundary conditions are implied along the four boundary lines (see Figure 2.13a). Consequently, $s_{33}^E$ is determined via Equation 2.7[15] [64].

$$s_{33}^E = \frac{\hat{S}_3}{\hat{T}_3} = \frac{\frac{1}{A}\int_A S_3 dA}{\frac{1}{A}\int_A T_3 dA} \tag{2.7}$$

Case II is applied to obtain the effective shear elastic compliance $s_{55}^E$. A pure shear strain ($\epsilon_{13}^0$=0.1) is imposed on the two dimensional RVE at zero electric field electrical boundary conditions (see Figure 2.13b). Under these conditions, $s_{55}^E$ is determined via Equation 2.8 [64].

$$s_{55}^E = \frac{\hat{S}_5}{\hat{T}_5} = \frac{\frac{1}{A}\int_A S_5 dA}{\frac{1}{A}\int_A T_5 dA} \tag{2.8}$$

Case III governs the computation of the effective $d_{15}$ and $\epsilon_{11}^T$ properties. A potential of $1V$ is applied along the 1-axis while (symmetric) free-stress mechanical boundary conditions are imposed at the four boundary lines (see Figure 2.13c). Rigid body displacements are prevented by implying zero displacements at node A. By consequence, $d_{15}$ and $\epsilon_{11}^T$ are computed with Equation 2.9 and 2.10 [64].

$$d_{15} = \frac{\hat{S}_5}{\hat{E}_1} = \frac{\frac{1}{A}\int_A S_5 dA}{\frac{1}{A}\int_A E_1 dA} \tag{2.9}$$

$$\epsilon_{11}^T = \frac{\hat{D}_1}{\hat{E}_1} = \frac{\frac{1}{A}\int_A D_1 dA}{\frac{1}{A}\int_A E_1 dA} \tag{2.10}$$

---

[14]Although the property characterization study presented in this chapter focuses on shear mode properties, the $s_{33}^E$ compliance property is investigated too for model verification purposes.

[15]Note that the surface integrals are computed by Comsol by evaluating the corresponding surface element-averaged values.

**(a)**



**(b)**



**(c)**
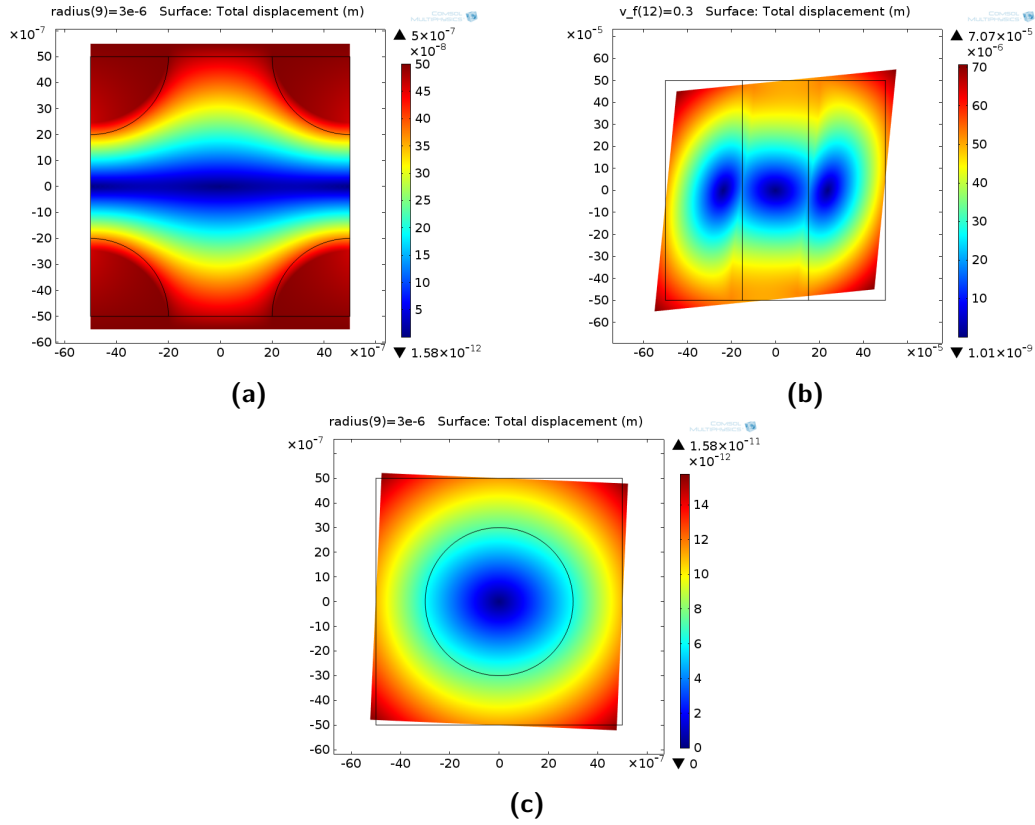
**Figure 2.13:** Surface displacement graphs of the three investigated cases, each depicted with one of the three analysed composite material types with identical PZT volume fractions ($v_f$=0.3): case I with corner-located circular PZT particles (displacement scaling factor = ×1) (a), case II with a center-located PZT fiber (displacement scaling factor = ×1) (b), and case III with a center-located circular PZT particle (displacement scaling factor = ×1000) (c).

Finally, the effective shear mode coupling factor $k_{15}$ can be determined by implementing Equation 2.8, 2.9, and 2.10 into Equation 1.9.

The final part of this section on the numerical homogenization simulation procedures presents the analytical framework applied for the verification of the applied FEM numerical models. The verification procedure is performed by comparing the numerically simulated effective properties in terms of PZT volume fractions with those obtained by simplified analytical models available in literature.

The analytical model derived by *Smith* and *Auld* is used for verifying the $s_{33}^E$ homogenization model of 1-3 fiber composites [65]. Under the geometrical restrictions of sufficiently small fiber diameters and inter-fiber distances, that is smaller than twice the composite's thickness (in 3-axis direction for the present analysis), the composite's effective stiffness $c_{33}^E$ ($=\frac{1}{s_{33}^E}$) in terms of fiber volume fraction ($v_f$ [−]) is described by Equation 2.11 [66].

$$c_{33}^E = \frac{1}{s_{33}^E} = v_f \left[ c_{33}^{E,f} - \frac{2v_f(c_{13}^{E,f} - c_{12}^m)^2}{v_f(c_{11}^m + c_{12}^m) + (1-v_f)(c_{11}^{E,f} - c_{12}^{E,f})} \right] \qquad (2.11)$$

Where in Equation 2.11, the '$f$' and '$m$' indices refer to the properties of the fiber and polymer phase, respectively.

The analytical model applied for the verification of the shear properties of the $1-3$ composite is based on an analytical asymptotic homogenization method as presented by *Benjeddou* and *Al-Ajmi* who considered a transversely poled (along the fiber's thickness) 1-3 fiber composite [67]. Adapting the equations to the longitudinally poled fiber composite in the present analysis and assuming uniform electric fields as well as plane stress boundary conditions, closed-form expressions of the macroscopic shear composite's properties can be obtained as described in Equation 2.12, 2.13, and 2.14 [67].

$$c_{55}^E = \frac{1}{s_{55}^E} = \frac{c_{55}^{E,f} c_{55}^m}{v_f c_{55}^m + (1 - v_f) c_{55}^{E,f}} \tag{2.12}$$

$$\epsilon_{11}^T = \epsilon_{11}^{T,f} v_f + \epsilon_{11}^m (1 - v_f) + v_f(1 - v_f) \frac{(d_{15}^{E,f} c_{55}^{E,f})^2}{v_f c_{55}^m + (1 - v_f) c_{55}^{E,f}} \tag{2.13}$$

$$d_{15} = \frac{d_{15} c_{55}^m c_{55}^{E,f} v_f}{c_{55}^E (v_f c_{55}^m + (1 - v_f) c_{55}^{E,f})} \tag{2.14}$$

Where in the denominator of Equation 2.14, $c_{55}^E$ refers to the composite's effective shear compliance obtained from Equation 2.12. Analogous to the FEM homogenization effective material study presented above, the analytical value for $k_{15}$ is determined by implementing Equation 2.12, 2.13, and 2.14 into Equation 1.9.

For the analytical verification of spherical particulate 0-3 composites, the model of *Furukawa et al.* is applied [68]. This highly simplified model assumes the piezoelectric phase to be isotropic and treats both phases as incompressible linear elastic materials. Moreover, the model is based on low piezoelectric particulate volume fractions; experimental validation indicated close agreement up to $v_f$=0.3 [68, 69]. Under these restrictions, Equations 2.15, 2.16, and 2.17 can be used to quantify the property versus volume fraction relation for the effective longitudinal stiffness $c_{33}^E$, shear stiffness $c_{55}^E$, and permittivity $\epsilon_{11}^T$, respectively.

$$c_{33}^E = \frac{1}{s_{33}^E} = c_{33}^m \frac{3c_{33}^m + 2c_{33}^{E,f} - v_f(c_{33}^m - c_{33}^{E,f})}{3c_{33}^m + 2c_{33}^{E,f} + 2v_f(c_{33}^m - c_{33}^{E,f})} \tag{2.15}$$

$$c_{55}^E = \frac{1}{s_{55}^E} = c_{55}^m \frac{3c_{55}^m + 2c_{55}^{E,f} - v_f(c_{55}^m - c_{55}^{E,f})}{3c_{55}^m + 2c_{55}^{E,f} + 2v_f(c_{55}^m - c_{55}^{E,f})} \tag{2.16}$$

$$\epsilon_{11}^T = \epsilon_{11}^m \frac{2\epsilon_{11}^m + \epsilon_{11}^{T,f} - 2v_f(\epsilon_{11}^m - \epsilon_{11}^{T,f})}{2\epsilon_{11}^m + \epsilon_{11}^{T,f} + v_f(\epsilon_{11}^m - \epsilon_{11}^{T,f})} \tag{2.17}$$

To the author's knowledge, there are no established analytical models for the effective piezoelectric shear coupling properties ($d_{15}$ or $k_{15}$) of particulate piezoelectric composites in the literature. This stipulates the requirement of a sound verification and validation of the (particulate composite) homogenization models. Moreover, it indicates once more the need of understanding the shear mode capabilities of particulate piezoelectric composites as investigated experimentally and numerically in this thesis.

## 2.3   Results

This section gives an overview of the results of the shear mode characterization study of the investigated piezoelectric material systems.

First, the verification and validation process of the novel impedance-based measurement is presented in Section 2.3.1. Next, the outcomes of the experimental and numerical characterization study are given in Section 2.3.2 and Section 2.3.3, respectively.

### 2.3.1   Verification and validation of the novel $d_{15}$ measurement method

As the novel IDE-based $d_{15}$ measurement technique is employed to determine the shear mode properties of the various (composite) materials under analysis, one first has to establish the accuracy of the new experimental method. To this aim, a thorough verification and validation process was performed by means of a reference piezoelectric ceramic sample.

For the (purely theoretical) verification phase, the impedance of an IDE shear sample with known material properties was obtained via FEM simulations. Next, $d_{15}$ properties were derived from simulated impedance data, which were compared with the (a priori known) properties fed to the model. In this way, the theoretical accuracy of the novel technique could be verified.

Secondly, for the experimental validation phase, numerically obtained impedance data and resulting shear properties were compared with experimentally obtained data of a sample with the same (geometrical and material) properties.

The verification simulations were performed with the two-dimensional IDE-based shear measurement model as described in Section 2.2.2. The implemented reference material was a PZT5-H piezoelectric ceramic with electromechanical properties presented in Appendix A. The geometrical properties of the model are identical to the PZT507 shear measurement sample as presented in Section 2.2 (Table 2.3).

The impedance spectrum (3.5-16$MHz$) was simulated to include the fundamental and $3^{rd}$ overtone (anti)resonance frequencies as depicted by the impedance plot shown in Figure 2.14c. The occurrence of the standing elastic waves at resonance is illustrated by the surface horizontal strain (in 2-axis direction) plots on Figure 2.14a and b. Shear properties ($k_{15}$, $s_{55}^E$, and $d_{15}$), derived from the simulated obtained (anti)resonance frequencies, are summarized and compared to the model's material shear properties in Table 2.5.

The novel IDE-based shear property characterization method is (numerically) able to derive the sample's shear property data with a small relative error between the computed and model properties. The root cause of this error is most probably the non-uniformity and inhomogeneity of the induced electric field by the interdigitated electrodes.

| | $k_{15}$ $[-]$ | $s_{55}^E$ $[Pa^{-1}]$ | $d_{15}$ $[\frac{C}{N}]$ |
|---|---|---|---|
| Simulated properties | 0.64 | 4.25·10$^{-11}$ | 7.22·10$^{-10}$ |
| Model properties | 0.67 | 4.35·10$^{-11}$ | 7.41·10$^{-10}$ |
| *RE [%]* | *5.4* | *2.3* | *2.5* |

**Table 2.5:** Simulated versus model input shear material properties of the IDE-based verification and validation PZT5-H model (RE = Relative Error). Reported data obtained from [14].

The second and last fundamental step to establish confidence in the IDE-based characterization method's capability is to validate the technique by experiment. Therefore, an impedance sweep (3.5-16$MHz$) was performed on the IDE PZT507 shear sample as described in Section 2.2. The resulting experimentally obtained fundamental impedance spectrum were plotted and compared with the simulated impedance of the aforementioned (verification) reference FEM model as illustrated in Figure 2.14c.

One can observe a significant deviation between the experimental and simulated (normalized) impedance magnitude at resonance conditions. The error is caused by not taking any (mechanical or electrical) losses into account for the FEM simulations. This is permitted for the current analysis as the error has no effect on the $d_{15}$ characterization study for which solely the (relative) positions of the (anti)resonance frequencies are required.

Proceeding with the validation analysis, the shear property values can be derived from the experimentally obtained impedance plot of Figure 2.14c. These experimentally obtained values are presented and compared with the previously derived numerical shear properties in Table reftab:validation. Note that the simulated impedance data are based on PZT5-H, whereas the (experimental) sample is made of PZT507, a customized version of the standard PZT5-H material [14]. As no shear property data of PZT507 is available in the literature, the PZT5-H property data were considered as a first-order reference and applied for the FEM (verification and) validation simulations.

Again, the simulated shear properties deviate from the experimentally obtained ones within reasonable bounds (<10%). This can be expected as the simulation model's material properties (PZT5-H) deviate from the sample's material properties (PZT507). Note that, besides the dissimilarity of the material properties, the error introduced by the non-uniform and inhomogeneous electric field at the IDE fingers will contribute to the observed validation error as discussed in the verification analysis. Moreover, as discussed in Section 2.1.1, the experimental impedance measurement conditions are expected to introduce small errors too ($\sim 3\%$) [49, 70].

|  | $k_{15}$ [$-$] | $s_{55}^E$ [$Pa^{-1}$] | $d_{15}$ [$\frac{C}{N}$] |
|---|---|---|---|
| Experimental properties | 0.67 | $4.60 \cdot 10^{-11}$ | $7.75 \cdot 10^{-10}$ |
| Simulated properties | 0.64 | $4.25 \cdot 10^{-11}$ | $7.22 \cdot 10^{-10}$ |
| *RE [%]* | *4.5* | *8.2* | *7.4* |

**Table 2.6:** Experimental (PZT507) versus simulated (PZT5-H) properties of the verification/-validation model (RE = Relative Error). Reported data obtained from [14].

Based on the verification and validation analysis presented above, it can be concluded that the novel IDE-based shear property measurement method can (theoretically and experimentally) be applied for the observation and first-order quantification of a piezoelectric material's shear properties when the standard shear impedance-based technique falls short.

**(a)**



**(b)**



**(c)**
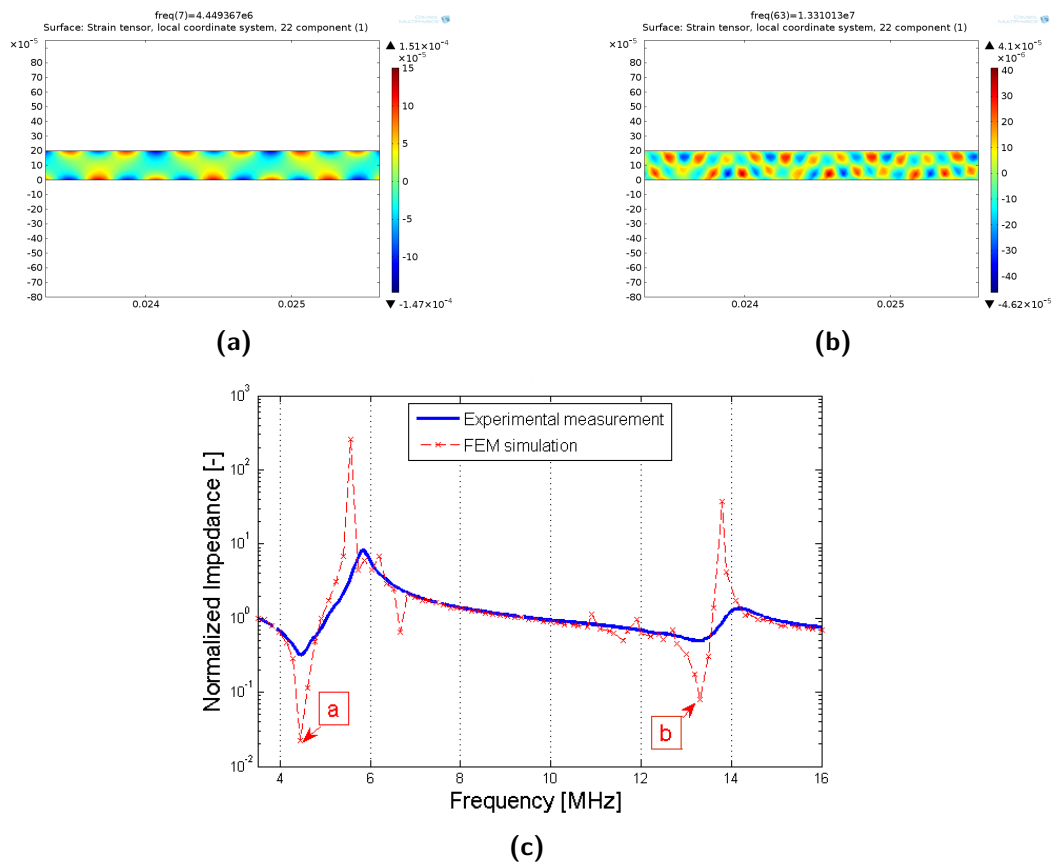
**Figure 2.14:** IDE-based shear mode characterization validation figures: (a) Strain ($2$-axis direction) surface plot illustrating the standing elastic shear wave at the fundamental resonance frequency, (b) Strain ($2$-axis direction) surface plot illustrating the standing elastic shear wave at the $3^{rd}$ overtone resonance frequency, and (c) experimental versus FEM simulated impedance plot ($3.6$-$16 MHz$).

### 2.3.2 Experimental results

This section presents the outcomes of the experimental shear mode property characterization study on piezoelectric (0-3 and 1-3) PZT-epoxy composite material systems. Firstly, the experimentally obtained impedance plots are introduced. Secondly, the results of the quasi-static piezoelectric charge constant measurements are given.

Impedance measurements were performed to observe and quantify the shear piezoelectric properties of the 0-3 and 1-3 composites.
All the particulate composite samples were characterized with flat (i.e. no (anti-)resonance frequencies) frequency spectra, as illustrated in the impedance plot of a $0.1mm$ thick 0-3 composite sample ($v_f$=0.3) depicted in Figure 2.15a. Consequently, no shear mode properties could be derived from the impedance measurements of the 0-3 composites.

In contrast, fundamental (anti-)resonance frequencies could be identified on the frequency spectra of the two fiber composite samples. Close-ups of the small, though observable peaks of the $v_f$=0.48 and $v_f$=0.65 fiber composite materials are plotted in Figure 2.15b and c, respectively.
Based on the procedures introduced in Section 2.1.1, the shear mode properties were derived from the experimentally obtained resonance peaks. The resulting $d_{15}$ values are presented in Table 2.7.
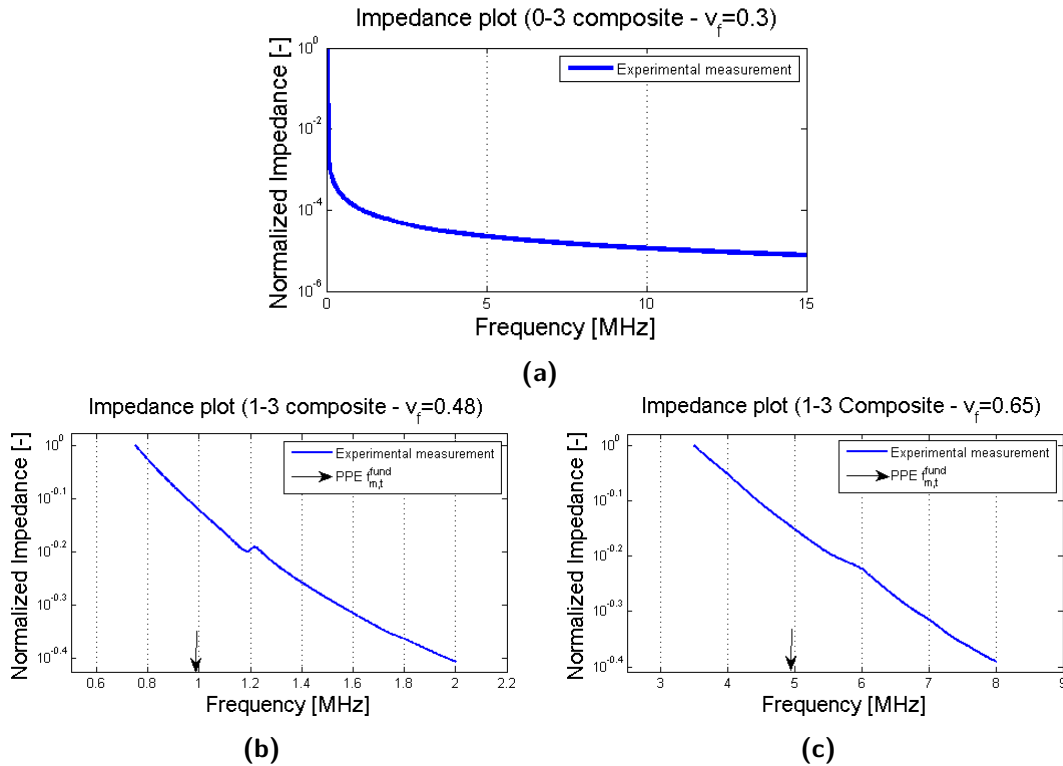


**Figure 2.15:** Experimental impedance plots: 0-3 composite ($v_f$=0.3, t=0.11$mm$) (a), 1-3 composite ($v_f$=0.48, t=1.54$mm$), 1-3 composite ($v_f$=0.65, t=0.3$mm$). The black arrows on the fiber composite impedance plots indicate the fundamental thickness resonance frequency measured with the original parallel plate poling electrods.

Quasi-static piezoelectric charge constant measurements were performed to complement the impedance-based results. The averaged experimentally obtained piezoelectric charge constants of the (PZT5A4-epoxy) particulate composite discs ($d_{33}$ and $d_{31}$) and rings ($d_{15}$) for

three PZT volume fractions are given in Table 2.7. Only the quasi-static $d_{33}$ measurements were performed with the fiber composite material samples due to the practical considerations stated in Section 2.2.1.

| | | 0-3 Composites | | | 1-3 Composites | |
|---|---|---|---|---|---|---|
| | $v_f \;=$ | 0.1 | 0.2 | 0.3 | 0.48 | 0.65 |
| **Impedance** | Resonance? | No | No | No | Yes | Yes |
| | $d_{15}\;[\frac{pC}{N}]$ | - | - | - | *106* | *190* |
| **Quasi-static** | $d_{31}\;[\frac{pC}{N}]$ | 0.2 | 0.8 | 1.3 | - | - |
| | $d_{33}\;[\frac{pC}{N}]$ | 0.8 | 2.5 | 3.9 | 352 | 371 |
| | $d_{15}\;[\frac{pC}{N}]$ | 0.8 | 1.91 | 2.79 | - | - |

**Table 2.7:** Summary of the experimental results of Chapter 2. Note that the (italic) impedance-based $d_{15}$ data should be considered as preliminary for reasons discussed in Section 2.4.

### 2.3.3   Numerical results

In order to determine the effective properties of both 0-3 and 1-3 piezoelectric composites, homogenization-based simulations were performed in tandem with the experimental (impedance and quasi-static) measurements. This section presents the resulting numerical property figures and verifies them with respect to the analytical framework developed in Section 2.3.3.

**0-3 Composites**
Figure 2.16 summarizes the simulated effective properties of the 0-3 (PZT5A4-epoxy) composite material system in terms of PZT volume fraction as defined in Section 2.2.2. For the elastic and dielectric properties, the results of *Furukawa*'s simplified analytical model are included for verification purposes. As both the numerical as well as the analytical model are based on low volume fractions (see Section 2.2.2), the property-fraction grahps are constructed for a $v_f$ up to 0.3.

Figure 2.16a depicts the effective longitudinal compliance $s_{33}^E$ in terms of PZT volume fraction $v_f$. It can be observed that there is no deviation between the simulated results of the center and corner located particle RVE models. Though, the numerically obtained $s_{33}^E$ values show a consistent offset with the analytical ones. Moreover, based on the trend of the numerical property-fraction relation, the $s_{33}^E$ value for a zero volume fraction differs from the expected value of the pristine epoxy material ($s_{33}^m$=3.45·10$^{-10}Pa^{-1}$), which is not the case for the analytical model. A potential cause for the small, though significant deviation could be a stiffening effect of the fixed (periodic) mechanical boundary conditions at the RVE's 1 and 3 edges applied to account for transverse contraction [63].

The effective shear compliance $s_{55}^E$ in terms of PZT volume fraction is illustrated in Figure 2.16b. For this case, there is a clear deviation between the two investigated FEM models. The center located particle model matches the analytical model, whereas the corner located particle model shows a clear deviation in both absolute value and the property-fraction trend with respect to the two other (center located particle numerical and analytical) models. A probable explanation of the presumably inaccurate results of the corner located particle model
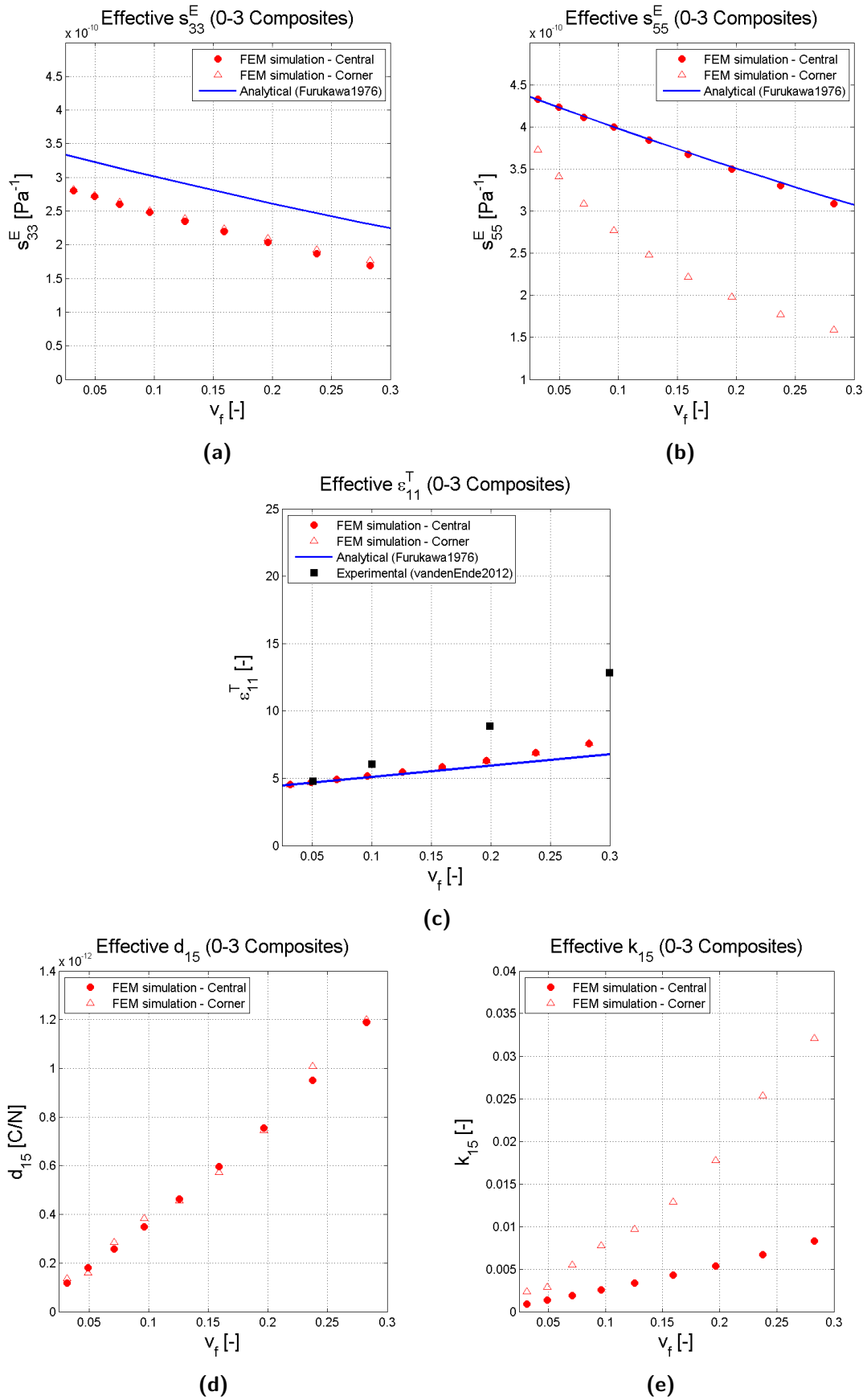
**Figure 2.16:** Numerical homogenization graphs for 0-3 composites: longitudinal compliance $s_{33}^E$ versus PZT5A4 particulate volume fraction $v_f$ (a), shear compliance $s_{55}^E$ versus $v_f$, permittivity $\epsilon_{11}^T$ versus $v_f$ (c), shear piezoelectric charge constant $d_{15}$ versus $v_f$ (d), shear coupling factor $k_{15}$ versus $v_f$ (e). The analytically obtained effective properties, as discussed in Section 2.2.2, are added, where available, for verification purposes.

is that the quarter particles positioned in the corners of the RVE, induce a (non-existing) stiffening effect for the applied uniform shear mechanical boundary conditions (see Table 2.4). This stiffening effect induces higher average shear stresses in the analysed RVE model, which eventually leads to a higher effective shear stiffness (lower effective shear compliance).

The effect of the PZT particle volume fraction on the relative permittivity $\epsilon_{11}^T$ can be examined in Figure 2.16c. Similar to the $s_{33}^E$ simulations, the center and corner located particle models do not differ. Moreover, for very low volume fractions (up to $v_f$=0.15), the numerical effective $\epsilon_{11}^T$ values match the analytical ones. However, for higher volume fractions, a non-linear trend in the numerical property-fraction causes the numerically obtained effective $\epsilon_{11}^T$ values to deviate from the analytical one.

To investigate the observed deviation in linear property-fraction behaviour of the numerical simulations, experimental data of a representative composite material system (particulate PZT5A4-epoxy) obtained from the literature[16] are included in Figure 2.16c [26]. Again, a non-linear relation can be observed as the experimental values start to deviate increasingly from the (linear) analytical ones for higher volume fractions. Hence, the non-linear trend of the numerical property-fraction relation is confirmed by the experimental data, exhibiting this non-linearity to a much higher extent.

The non-linear trend in the $\epsilon_{11}^T$-$v_f$ relation can be attributed to decreasing inter-particle distances for increased volume fractions. In contrast to the numerical models, this effect is not taken into account for the analytical model based on a single PZT inclusion in the polymer matrix. Although the numerical simulations also deviate from the linear property-fraction relation predicted by the highly simplified analytical model, a significant discrepancy between the numerical and experimental data is still present. Once more, this can be explained by the fact that the inter-particle distances will decrease as the volume fraction increases, eventually leading to touching/agglomerating particles. As the numerical model does not account for touching particles as well as interfacial effects, a deviation between the numerically and experimentally obtained values for $\epsilon_{11}^T$ is expected, commencing for relatively moderately low volume fractions (i.e. $v_f$=15%) and increasing for higher volume fractions.

The relation between the effective shear piezoelectric charge constant $d_{15}$ and volume fraction is depicted in Figure 2.16d. The center and corner located particle models result in identical effective $d_{15}$ values, which is expected as they did not differ for the effective permittivity simulations for which the same boundary conditions are implied (see Table 2.4). The numerical simulations indicate a quasi-linear fraction-property relation for the considered volume fraction range.

As discussed in Section 2.2.2, no analytical model could be applied for the verification of the numerical shear coupling properties. However, based on the above discussion on the effective permittivity simulations, one can expect an increasing small, though significant discrepancy by ignoring particle agglomerations and interfacial effects for increasing volume fractions.

Next, based on the numerically obtained $s_{55}^E$, $\epsilon_{11}^T$, and $d_{15}$ values, the effective shear coupling factor $k_{15}$ versus volume fraction can be obtained as illustrated in Figure 2.16e. Since the center and corner located particle RVE models deviate for the $s_{55}^E$ simulations, they differ for the $k_{15}$-$v_f$ relation too. As explained above, the center located particle model is expected to be the most accurate representation of the two.

---

[16]As the model assumes perfectly poled PZT inclusions, a set of representative experimental data of particulate piezoelectric composites (poled at optimum poling conditions) from the literature was included in Figure 2.16c instead of the experimentally obtained $\epsilon_{11}^T$ values of the prepared particulate composite discs.
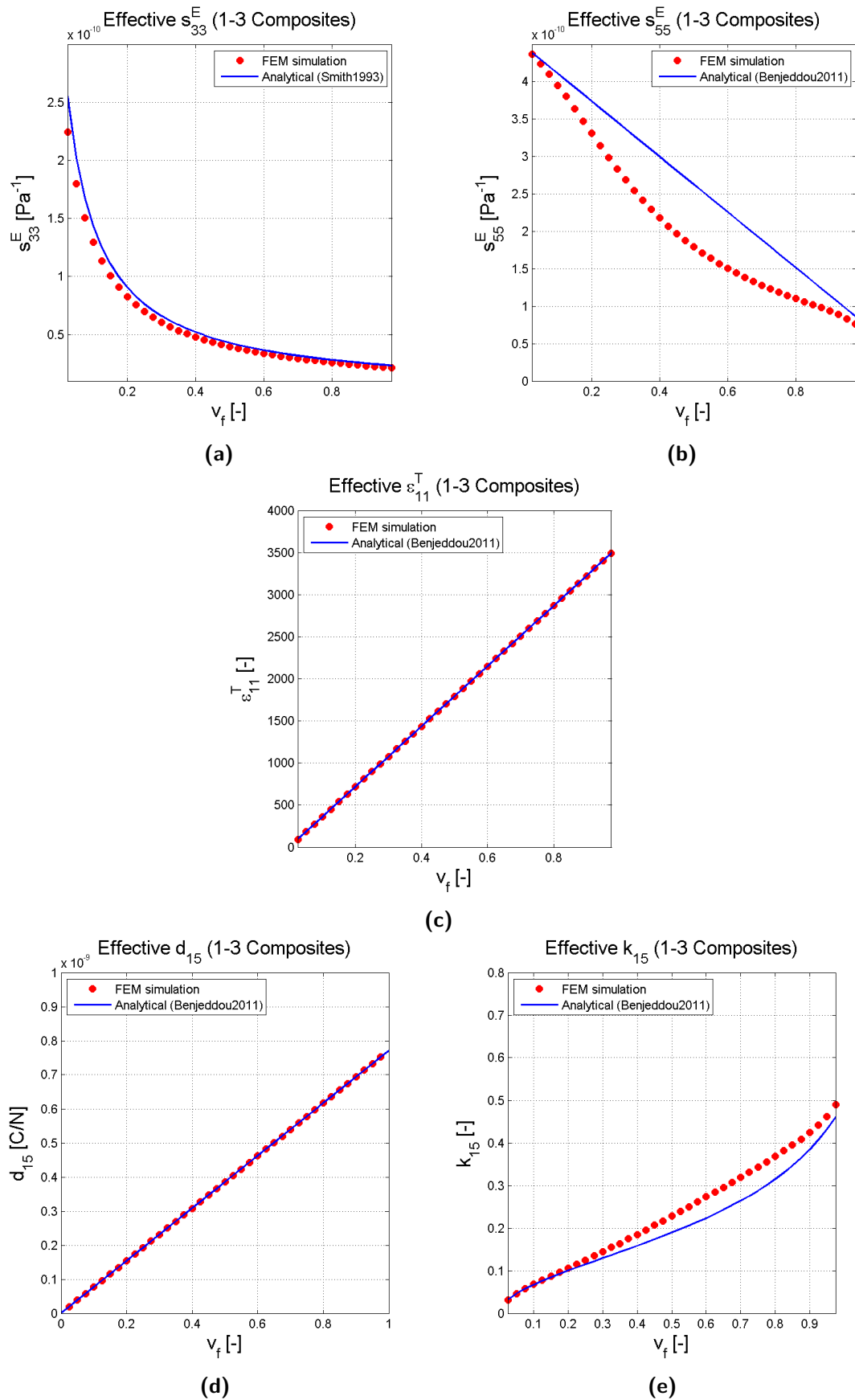
**Figure 2.17:** Numerical homogenization graphs for 1-3 composites: $s_{33}^E$ versus PZT5A4 fiber volume fraction $v_f$ (a), shear compliance $s_{55}^E$ versus $v_f$, permittivity $\epsilon_{11}^T$ versus $v_f$ (c), shear piezoelectric charge constant $d_{15}$ versus $v_f$ (d), shear coupling factor $k_{15}$ versus $v_f$ (e). The analytically obtained effective properties, as discussed in Section 2.2.2, are added, where available, for verification purposes.

## 1-3 Composites

Figure 2.17 summarizes the results of the effective property simulations of the second material system under consideration: the (SP53-epoxy) fiber piezoelectric composite. The effective properties in terms of fiber volume fraction ($v_f$) of both the numerical homogenization model and the analytical (homogenization) models are included in Figure 2.17.

The effective $s_{33}^E$ versus $v_f$ is plotted in Figure 2.17a. One can observe that the numerically obtained values follow the same trend as the analytical values. There is a consistent, though acceptably small overestimation of the analytical compliance values with respect to the numerical ones.

Figure 2.17b depicts the effective $s_{55}^E$ in terms of fiber volume fraction. In this case, the trend between the values of the two models differs and the relative error between the analytical and numerical data is much higher than for the simulated $s_{33}^E$ properties, except for the limit $v_f$ scenarios where both models approach the pristine (fiber and polymer) $s_{55}^E$ values.
A possible explanation for the observed deviation between the analytical and numerical results can be found in the zero thickness stress assumption. This assumption, which was not applied for the numerical homogenization-based simulations, is imposed to obtain a closed-form $s_{55}^E$ expression for the analytical model [67].

The results of the effective relative permittivity ($\epsilon_{11}^T$) simulations are presented in Figure 2.17c. In contrast to the 0-3 homogenization results, the numerical values match the analytical ones with a maximum relative error of 0.01%. As the fibers form a continuous path between the bottom and top electrodes of the RVE and there is, by consequence, no non-linear effect of touching/agglomerating particles, a linear permittivity-fraction relation can be observed for both (homogenization-based) models.

Figure 2.17d illustrates a good agreement between the numerically and analytically obtained $d_{15}$ values of the 1-3 composites. Contrary to the effective shear compliance analysis, the plane stress and uniform field assumptions (as stated in Section 2.2.2) have no influence on the simulated effective shear piezoelectric charge constant.

The relation between the simulated effective shear coupling factor $k_{15}$ and the fiber volume fraction is depicted in Figure 2.17e. Due to overestimation of the analytical shear compliance with respect to the numerical value, the analytically obtained $k_{15}$ figures are consistently lower than the numerically obtained ones, though the relative error between the two stays within reasonable bounds (maximum relative error $\sim$20%). As the analytical model is a simplified version of the numerical FEM model, it is expected that the numerical model provides a more accurate representation for the simulation of the effective $k_{15}$.

**Conclusions on the verification of 0-3 and 1-3 effective property simulations**
It was found that the (central particle located) 0-3 FEM model can solely be applied for a first order characterization of the effective shear properties of particulate composites as interfacial effects as well as the effects of touching particles are not taken into account.
In contrast, the results of the 1-3 composite numerical simulations were in close agreement with the figures obtained from the analytical framework. Solely the simulated shear compliance data deviated from the analytical ones. Taking into account the simplifying assumption(s) made for the closed-form analytical expression, it is expected that the numerical model is a more accurate representation of the physical reality.

## 2.4 Discussion

This section reviews and comments on the key results presented in Section 2.3.2 and 2.3.3. First, the numerically and experimentally obtained impedance spectra of the 0-3 and 1-3 piezoelectric composite systems are compared. Thereafter, the relative magnitudes of the particulate composites' piezoelectric charge constants ($d_{33}$, $d_{31}$, and $d_{15}$) at varying PZT volume fractions are investigated.

As presented in Section 2.3.2, no resonance peaks could be observed on the experimental impedance plots of the IDE-based particulate composite shear measurement samples. It was presumed that the piezoelectric shear coupling of these material systems is too low to induce observable resonance conditions from which shear material properties can be derived.

To investigate this hypothesis, numerical impedance plots were obtained by means of the two dimensional IDE-based FEM model. A first set of impedance spectra were simulated with a piezoelectric coupling matrix based on the verified effective property simulations, as discussed in the preceding section. The second set of simulated impedance plots were performed using the quasi-static experimental $d_{ij}$ measurements as input for the material's coupling.
For the complete set of investigated volume fraction and sample thicknesses, the three impedance spectra corresponded to each other by returning approximately identical flat spectra. This is illustrated in Figure 2.18a, in which the three (normalized) impedance spectra of a particulate composite sample ($v_f$=0.3) are collected for the analysed frequency range (0.1-15$MHz$).
Consequently, it can be stated that, based on numerical (homogenization-based) simulations and experimental (impedance-based and quasi-static) measurements, piezoelectric particulate composites exhibit shear piezoelectric coupling, albeit too low to be observed or quantified by impedance-based characterization techniques.

In contrast, fundamental (anti-)resonance peaks could be identified on the impedance spectra of the two prepared IDE fiber composite samples. Yet, the observed peaks are not located within the frequency range one would expect for pure (fundamental) shear resonance of the measured samples. This is illustrated in Figure 2.18b, in which the simulated impedance spectrum of the $v_f$=0.48 sample is plotted with the experimentally obtained one[17].
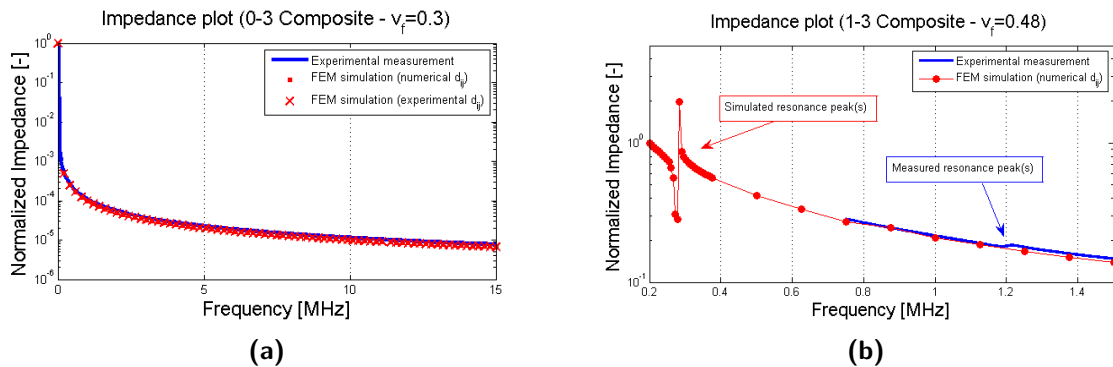


**Figure 2.18:** Experimental versus impedance plots: experimental and numerical impedance spectra of a 0-3 composite sample ($v_f$=0.3, t=0.11$mm$) (a), experimental and numerical impedance spectra of a 1-3 composite ($v_f$=0.48, t=1.54$mm$) (b).

---

[17]The impedance simulations were obtained by means of the two dimensional IDE-based FEM model with a piezoelectric shear charge constant $d_{15}$ equal to the numerically simulated effective $d_{15}$ value. Furthermore,
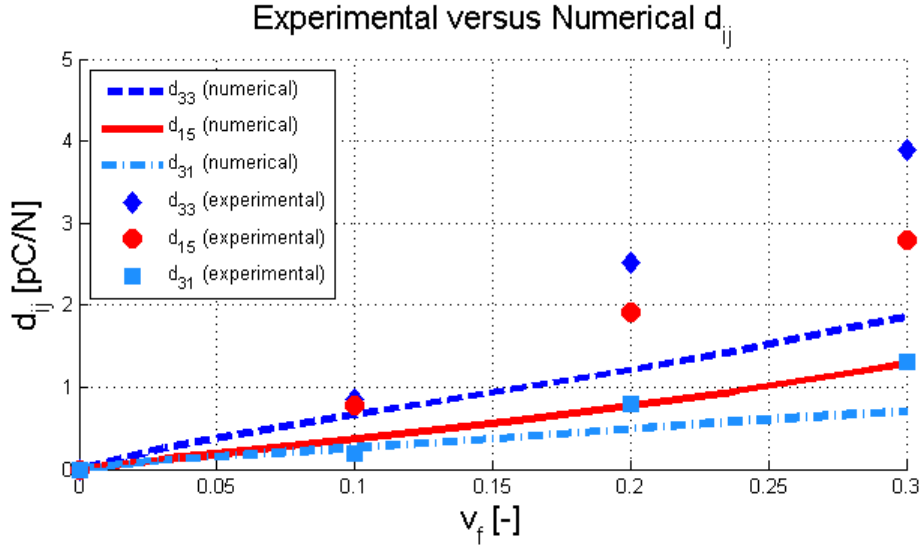
**Figure 2.19:** Experimental versus numerical $d_{ij}$ versus $v_f$ of a PZT5A4-epoxy particulate composite system. The experimental data is given in Table 2.7.

As the experimental resonance frequencies are closely located to the original fundamental thickness resonance frequencies (see Figure 2.15b and c), it is questionable that the observed frequencies represent the occurrence of pure shear resonance of the samples. Therefore, the derived $d_{15}$ values in Table 2.7, should be interpreted as preliminary in anticipation of future work investigating the exact physical roots of the observed frequencies.

Next, to put the relatively low magnitude of the numerically and experimentally obtained $d_{15}$ figures of the particulate composites in perspective, additional homogenization-based simulations were performed to determine the effective $d_{33}$ and $d_{31}$ properties of these material systems[18].
The resulting piezoelectric charge constant versus PZT volume fraction relations are depicted in Figure 2.19. The complementary quasi-static experimental data of the prepared composite discs ($d_{33}$ and $d_{31}$) and rings ($d_{15}$) are included too.

Two paramount conclusions can be drawn from Figure 2.19.
Firstly, it can be observed that the presumed underestimation of the numerical effective properties with respect to the experimental ones ones holds. As explained in Section 2.3.3, this can be attributed to the simplifying assumptions made for the homogenization-based simulations. Yet, the trend in charge constant versus volume fraction of the experimental and numerical $d_{ij}$ values is similar.

The second important observation is the relative magnitude of the piezoelectric charge constants at fixed volume fractions. Both the numerical and experimental data provide evidence that the bulk PZT5A4 $\frac{d_{15}}{d_{33}}$ ratio ($\sim 1.2$) is not maintained for the particulate composite material. In contrast, the bulk PZT5A4 $\frac{d_{31}}{d_{33}}$ ratio ($\sim 0.4$) is maintained for the particulate composite materials by both characterization methods.

A possible cause for the reduction in shear mode coupling capability of the piezoelectric

---

the $d_{33}$ value was based on the quasi-statically obtained one and it was assumed that $d_{31}$=-0.3$d_{33}$.

[18]The set-up of these FEM simulations is analogous to the analysis presented in Section 2.2.2, the key points are summarized in Appendix B.

particulate composite materials is that the shear stress/strain transfer from the (compliant) piezoelectric matrix to the micron-sized PZT particles is less effective than for normal (compressive or tensile) stress/strain transfer. This remarkable result has to be confirmed by future work by, for instance, less simplified numerical homogenization-based FEM simulations (e.g. taking into account interfacial effects) or an enlarged experimental investigation (e.g. exploring the effect of the particle size or sample geometry on the quasi-static measurements).

## 2.5   Conclusions Chapter 2

In this chapter an IDE-based measurement method was proposed for the shear mode characterization of piezoelectric composites. The novel method proved to be a sound alternative for the standard impedance-based shear measurement method as verified and validated by means of a reference PZT material. Moreover, the IDE-based technique appeared to be particularly convenient for thin and costly (composite) samples as no cutting operations, inevitably leading to material losses and increased risks of sample fracture, are required.

The new impedance-based technique was found to be unsuitable for the observation (and quantification) of the shear coupling properties of particulate composite materials as they failed to exhibit resonance behaviour. Numerical homogenization-based simulations as well as complementary experimental quasi-static measurements indicated that this can be attributed to the inherently low piezoelectric coupling properties of these composite material systems.

In contrast to the results of the particulate composites, fundamental resonance frequencies could be identified on the impedance spectra of the IDE fiber composite samples. Yet, the observed frequencies do not coincide with numerically simulated (pure shear) resonance frequencies. Future work on the physical cause behind these unexpected frequency figures is recommended to establish the validity of employing the new method for the shear mode property characterization of piezoelectric fiber composites.

Furthermore, the numerical and experimental characterization study indicated that, in contrast to the particulate composite's effective $\frac{d_{31}}{d_{33}}$ ratio, its effective $\frac{d_{15}}{d_{33}}$ ratio at fixed piezoelectric material filling grades, is lower than the bulk active material's $\frac{d_{15}}{d_{33}}$ ratio.

# Chapter 3

# A shear versus normal strain-driven composite energy harvesting patch

This chapter addresses the second research objective on the performance assessment of a piezoelectric composite energy harvesting patch operating at shear ($d_{15}$) versus normal ($d_{33}$) strain-driven loading conditions.

To this aim, the energy generating performance of a patch provided with IDE is simulated and compared with the maximum (material-based) energy densities. In addition, the effect of the electrode geometry on the energy generating capability is studied. Furthermore, surface strain-driven energy harvesting case studies were developed to asses the influence of complex strain states and to provide an experimental validation tool for the aforementioned numerical study.

## 3.1 Introduction

A summary of the resulting research strategy is illustrated in Figure 3.2.

First, a finite element model of a piezoelectric composite energy harvesting patch was constructed. The patch is provided with IDE to assess and compare its performance when operating on the $d_{15}$- and $d_{33}$-modes without having to alter its electrode design concept. To assess the patches' performance for the two operation modes of interest, both pure (1%) shear and normal strain-driven operations were studied.

Moreover, the patches' material properties were fixed by applying the numerically obtained particulate composite (PZT5A4-epoxy, $v_f$=20%) properties as presented in Chapter 2. Consequently, the simulated material's energy densities can be obtained conform the material figures of merit study discussed in Chapter 1 (see Equation 1.13). The corresponding material-based strain-driven energy densities (summarized in Figure 3.1) were used as a reference for the outcomes of the IDE patch simulations.

The second part governs two FEA case studies for which the energy generating performance of the compliant patch, being (shear and/or axially) strained by deformation of their host structure, were quantified and compared.

The first case investigates a patch attached to the surface of a cantilever (solid) rod host structure. Exerting an axial tensile force on the rod's end induces normal strain on the patch, whereas the application of a torsional moment puts the patch under shear strain. Henceforth, this case allows one to compare the energy-based performance of the patch operated at the two distinct load cases though with a constant elastic deformation energy resulting from the deformed host structure.

The first case provides a straightforward way to assess the performance of the patch at the two strain-driven loading conditions of interest. However, for most energy harvesting applications, the loads on the host structure are known and result in a predetermined (fixed) strain distribution. Consequently, a second case study was developed to evaluate the energy-based performance of a shear versus axial strain-driven loaded patch on the same location on a host structure subjected to a fixed loading condition.

The second case governs a cantilever beam bended by a vertical tip force. As a result, normal stresses/strains develop at the beam's top surface on which the patch is applied. Applying the concept of (plane strain) strain transformation[1], one can alter the effective patch's strain distribution by rotation of the (sufficiently small and perfectly bonded) compliant patch. A detailed explanation of this concept is given in Section 3.2.2.

The chapter's outline is as follows. Section 3.2 presents the theoretical background as well as the set-up of the FEM models constructed for the study introduced above. Next, the outcome of the numerical simulations are discussed in Section 3.3. A brief conclusion on the chapter's key points is presented in Section 3.4.
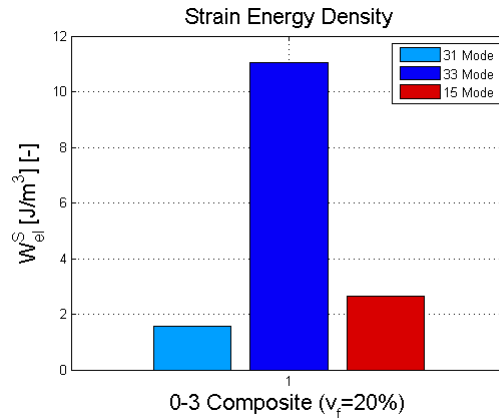


**Figure 3.1:** Strain-driven energy densities of the $v_f$=20% particulate composite operating at 1% strain. The material data were obtained from the effective property simulations presented in Chapter 2.

---

[1]Strain/stress transformation is a concept commonly used, for instance, to experimentally determine the strain or stress state of a material based on strain gauge readings [71].
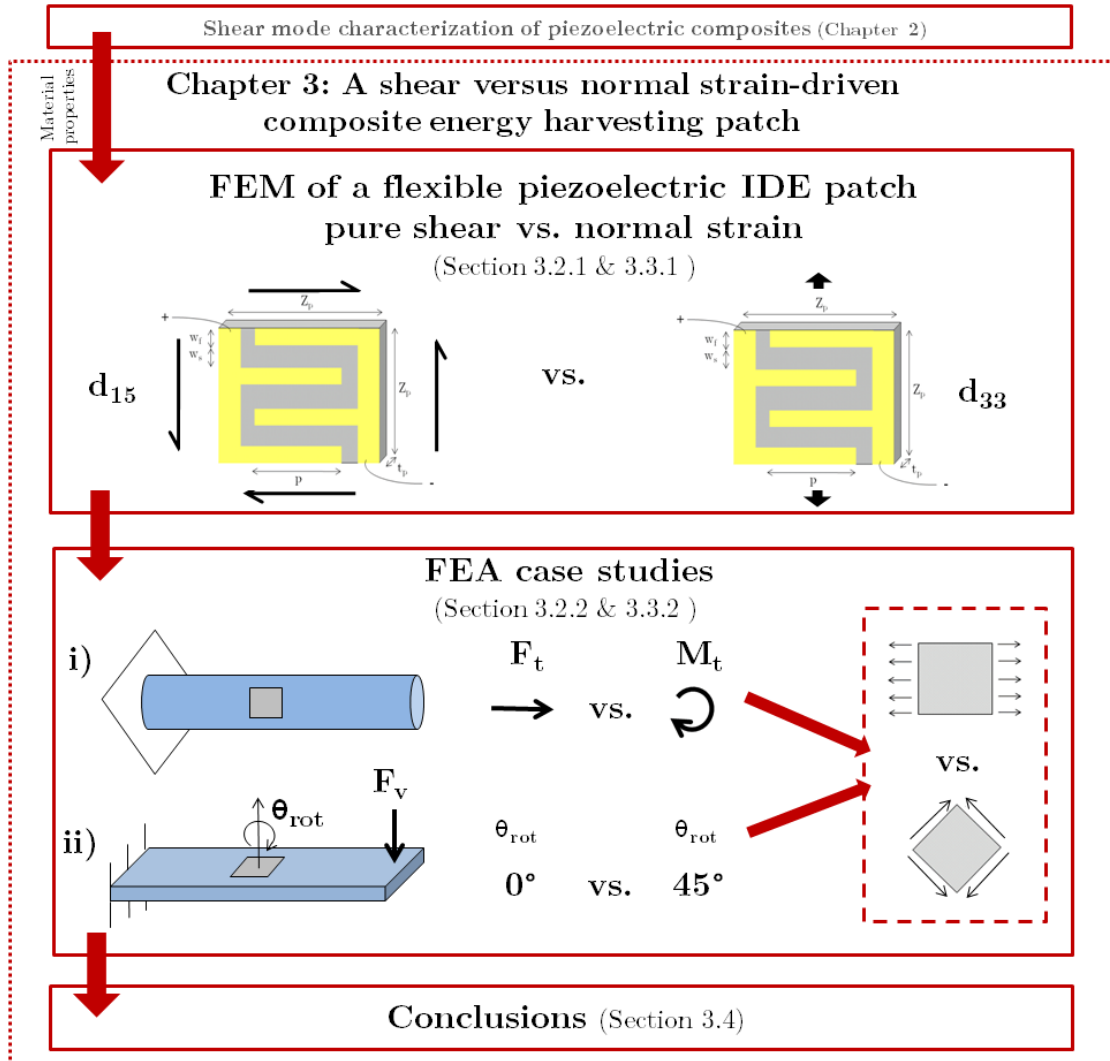
**Figure 3.2:** Graphical outline of Chapter 3.

## 3.2   Numerical methods

This section introduces the numerical simulations performed to assess the energy-based performance of a strain-driven flexible energy harvesting patch[2]. First, the set-up of the IDE-based patch finite element model is introduced in Section 3.2.1. Followed by the basic building blocks of the strain-driven energy harvesting case studies presented in Section 3.2.2.

### 3.2.1   Set-up of the piezoelectric energy harvesting patch model

An (adaptive) three dimensional finite element model of a square piezoelectric patch was constructed to examine the influence of the IDE design on the patches' performance for both $d_{15}$ and $d_{33}$ operation modes.

A generic image of the IDE-based patch is illustrated in Figure 3.3a. The size of the square patch is described by its square surface dimension $Z_p$ $[m]$ and thickness $t_p$ $[m]$. Conform the IDE geometrical definitions of Figure 2.4, $w_f$, $s_f$, $p$ and $t_s$, refer to the electrode finger width, inter-finger spacing, common finger length, and side electrode thickness, respectively.

As part of the IDE patch study investigates the effect of the electrode finger width and spacing on the patch's energy generating performance, the $w_f$ and $\frac{w_f}{s_f}$ figures were varied. The values of the fixed (IDE) dimensions as well as the investigated $w_f$ and $\frac{w_f}{s_f}$ intervals are summarized in Table 3.1.
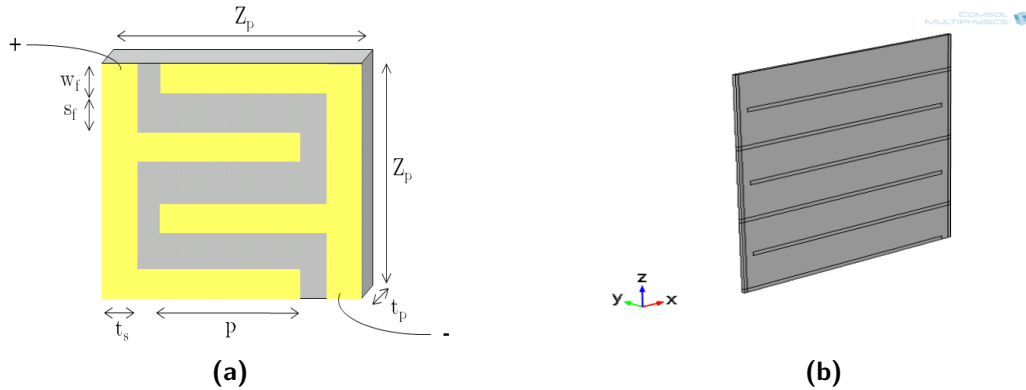


**Figure 3.3:** Images of the adaptive patch finite element model: generic image illustrating the patch's geometrical properties (a), and snapshot image of a patch in Comsol (b).

The patch's active material was implemented with bulk electromechanical material properties. Analogous to its geometrical properties, the density, (isotropic) compliance matrix, coupling matrix and permittivity vector of the adaptive model's composite material can be tailored to a particular material system as described in Appendix A.

For the present study, the assumed electromechanical material properties were based on a particulate (PZT-epoxy) composite ($v_f$=0.2) as summarized in Equation 3.1, 3.2, 3.3, and

| $w_f$ $[mm]$ | $\frac{w_f}{s_f}$ $[-]$ | $Z_p$ $[mm]$ | $t_p$ $[mm]$ | $p$ $[mm]$ | $t_s$ $[mm]$ |
|---|---|---|---|---|---|
| [0.25:0.25:1.25] | [0.1:0.05:1] | 15 | 0.2 | 13.6 | 0.2 |

**Table 3.1:** Fixed and varied dimensions for the IDE patch simulations.

---

[2]All finite element simulations discussed in this Chapter were performed in the Comsol environment with a *Stationary Study* approach as solely (quasi-)static operations are investigated.

$3.4^3$. The material's density was based on the rules of mixtures, whereas the compliance matrix is identical to the one of the pristine epoxy material. The piezoelectric coupling and (isotropic) permittivity matrix were based on the results of the numerical characterization study presented in Chapter 2.

$$\rho = 2500 [\frac{kg}{m^3}] \tag{3.1}$$

$$\bar{\bar{d}} = \begin{bmatrix} 0 & 0 & 0 & 0 & 0.5 & 0 \\ 0 & 0 & 0 & 0.5 & 0 & 0 \\ -0.3 & -0.3 & 0.8 & 0 & 0 & 0 \end{bmatrix} [\frac{pC}{N}] \tag{3.3}$$

$$\bar{\bar{s}}^E = 10^{-10} \cdot \begin{bmatrix} 3.45 & -1.03 & -1.03 & 0 & 0 & 0 \\ -1.03 & 3.45 & -1.03 & 0 & 0 & 0 \\ -1.03 & -1.03 & 3.45 & 0 & 0 & 0 \\ 0 & 0 & 0 & 4.48 & 0 & 0 \\ 0 & 0 & 0 & 0 & 4.48 & 0 \\ 0 & 0 & 0 & 0 & 0 & 4.48 \end{bmatrix} [Pa^{-1}] \tag{3.2}$$

$$\bar{\bar{\epsilon}}^T = \begin{bmatrix} 5.5 \\ 5.5 \\ 5.5 \end{bmatrix} [-] \tag{3.4}$$

The adaptive energy harvesting patch FEM was simulated with physics-controlled, tetrahedral mesh elements ('finer' size setting) within Comsol's *Piezoelectric devices* and *Electrostatic* module. Piezoelectric simulations were performed to compute the generated voltage ($V_{gen}$) upon mechanical excitation of the patch. $V_{gen}$ is computed by implying zero charge electrical boundary conditions on the 'positive' electrode finger network, whereas the 'negative' electrode finger network is provided with grounded electrical boundary conditions.

Electrostatic simulations were required to retrieve the free capacitance ($C_{free}$) of the energy harvesting system. $C_{free}$ is determined by applying a terminal potential of $1V$ on the 'positive' electrode finger network, whereas the 'negative' electrode finger network is electrically grounded (see Figure 3.4c). Consequently the generated energy ($U_{gen}$) is obtained by combining Equation 1.15 and 1.16 as formulated by Equation 3.5.

$$U_{gen} = \frac{1}{2} C_{free} V_{gen}^2 \tag{3.5}$$

As discussed in Section 3.1, the effect of the IDE lay-out on the patch's energy harvesting capabilities was investigated for two distinct mechanical excitation schemes: a pure shear ($\gamma_{13}^0 = 0.01$) versus pure normal ($\epsilon_{33}^0 = 0.01$) strain-driven loading schemes. These two conditions are illustrated in Figure 3.4a (pure shear strain) and 3.4b (pure normal strain).

By examining the two strain-driven loading conditions, the harvester's performance for two piezoelectric operation modes ($d_{15}$ and $d_{33}$) was investigated by appropriately orienting the (local) material axes system as each operation mode requires a different poling (or 3-axis) orientation[4]. The resulting material axes system with respect to the model's global coordinate system is summarized by Table 3.2. The X-Y-Z system refers to the global coordinate system as defined in Figure 3.3b, whereas the 1-2-3 refers to the local material system illustrated in Figure 1.3.

| Mode | X | Y | Z |
|------|---|---|---|
| $d_{15}$ | 3 | 2 | 1 |
| $d_{33}$ | 1 | 2 | 3 |

**Table 3.2:** Local material axes system (1-2-3) with respect to the global coordinate system (X-Y-Z) for the investigation of the $d_{15}$ and $d_{33}$ piezoelectric operation modes of the IDE patch.

---

[3]The material property indices are conform the standard piezoelectric orthogonal axes system as defined by Figure 1.3. Moreover, the effect of the electrodes on the mechanical behaviour of the patch is neglected.

[4]As discussed in Chapter 2, the piezoelectric material's poling axis has to be perpendicular to the IDE orientation for $d_{15}$ mode operation, whereas for $d_{33}$ mode operation the poling axis has to be aligned with the IDE field lines.

**(a)**                                                                                  **(b)**



**(c)**
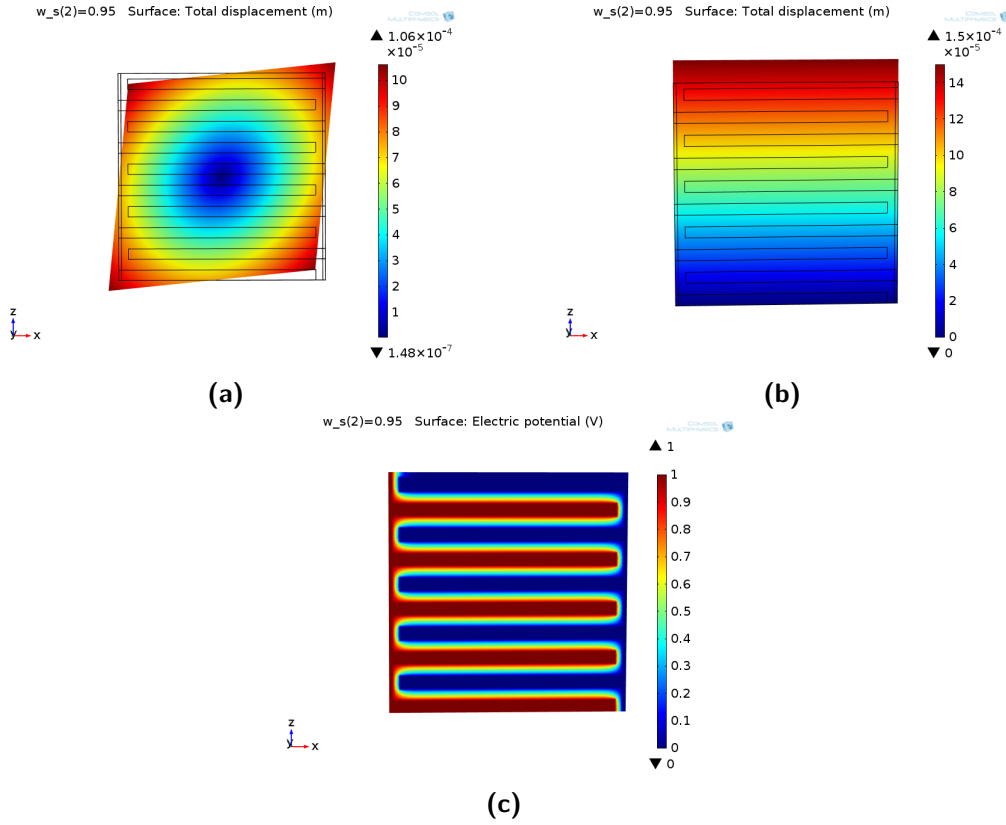
**Figure 3.4:** Surface displacement and potential graphs for the patch numerical IDE lay-out study ($w_f$=0.25$mm$ and $s_f$=0.263$mm$): surface displacement graph of the IDE patch at pure shear strain conditions ($\gamma_{13}^0 = 0.01$) depicted with a x10 scaling deformation factor (a), surface displacement graph of the IDE patch at pure normal strain conditions ($\epsilon_{33}^0 = 0.01$) depicted with a x10 scaling deformation factor (b), and surface potential graph of the IDE patch with a $1V$ excitation voltage applied for $C_{free}$ evaluation (c).

The last part on the set-up of the adaptive patch FEM briefly presents the analytical framework applied to verify the results of the numerical simulations.

For the evaluation of the free capacitance ($C_{free}$) *Engan*'s model was applied to the IDE system under analysis as described in Equation 3.6 [72].

$$C_{free} = \frac{2p(w_f + s_f)}{Z_p} \frac{K(k)}{K(k')} \epsilon^{a,T} \tag{3.6}$$

Where in Equation 3.6, $K(x)$ refers to the complete elliptical integral of the first kind (Equation 3.7[5]), and $k$ and $k'$ are variable functions fully determined by $w_f$ and $s_f$ (Equation 3.8 and 3.9, respectively).

$$K(x) = \int_0^{\frac{\pi}{2}} \frac{1}{\sqrt{1 - x^2 cos(\theta)}} d\theta \tag{3.7}$$

$$k = cos(\frac{\pi}{2}(1 - \frac{w_f}{w_f + s_f})) \tag{3.8}$$

$$k' = \sqrt{1 - k^2} \tag{3.9}$$

---

[5]The elliptical integral operation was performed within the MATLAB® computing environment [73].

Next, a simplified expression for the generated charge ($Q_{gen}$) by the deformed harvesting patch can be obtained by application of the piezoelectric linear constitutive equations (Equation 1.2). Consequently, Equation 3.10 is used to compute the approximate $Q_{gen}$ values for $d_{15}$ or $d_{33}$ strain-driven operations.

$$Q_{gen}^{d_{ij}} = d_{ij} \frac{p t_p}{s_{jj}^E} S_j \tag{3.10}$$

Lastly, the generated energy ($U_{gen}$) is evaluated by inserting Equation 3.6 and 3.10 into Equation 1.16 and 3.5.

### 3.2.2 Set-up strain-driven energy harvesting case studies

This section presents the main considerations required to construct and analyse the FEMs for the two aforementioned strain-driven energy harvesting case studies: an IDE patch on a cantilever rod (i) and an IDE patch on a cantilever beam (ii).

#### Patch on cantilever rod

The energy generated by a piezoelectric IDE patch on a cantilever rod ($r_{rod}$=3.5$cm$ and $L_{rod}$=20$cm$) is investigated via two distinct load cases: a torsional moment and an axial force. Examining these two load cases allows for comparison of the two operating modes of interest ($d_{15}$ and $d_{33}$), subjected to equal elastic deformation energies ($U_{el}$) [$J$].

A three dimensional finite element model of the patch-rod system was constructed in Comsol. The host structure was modelled as a solid aluminium shaft with linear elastic material properties presented in Appendix A. The rod was provided with fixed mechanical boundary conditions at its lower surface ($Z$=0), whereas either a static boundary force $F_t$ [$N$] or moment $M_t$ [$Nm$] was applied at its end ($Z$=$L_{rod}$) along or about the global $Z$-axis, respectively. A patch with fixed geometrical (Table 3.3[6]) and composite material properties (Equation 3.1, 3.2, 3.3, and 3.4) was attached to the radial outer surface of the rod at half its length. The piezoelectric and electrostatic simulations of the patch are conform the IDE patch analysis described in Section 3.2.1.

The single deviation with respect to the previous FEM model of the single IDE patch is the orientation of the local (1-2-3) material axes system with respect to the global (X-Y-Z) system. For $d_{33}$ mode operation, ($F_t$) the orientation as defined by Table 3.2 holds (see Figure 3.6). However, for $d_{15}$ operation ($M_t$), the poling (or 3-)axis has to follow the curvature of the rod (see Figure 3.5).

| $w_f$ [$mm$] | $\frac{w_f}{s_f}$ [$-$] | $Z_p$ [$mm$] | $t_p$ [$mm$] | $p$ [$mm$] | $t_s$ [$mm$] |
|---|---|---|---|---|---|
| 1 | 0.1 | 3.4 | 0.2 | 3.26 | 0.2 |

**Table 3.3:** Geometrical properties of the patch for the energy harvesting case studies.

---

[6]The electrode finger width and spacing values are based on the results of the IDE patch geometry study presented in Section 3.3.1.
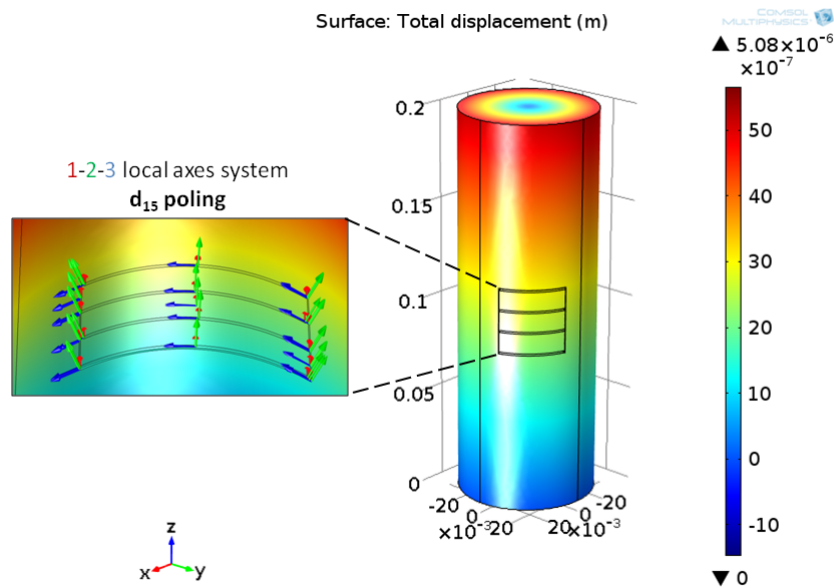
**Figure 3.5:** Surface displacement plot $[m]$ of the rod-patch FEM for $d_{15}$ operation $(M_t)$, the insert depicts the orientation of local material axes system with respect to the global axes system as defined in Equation 3.11.
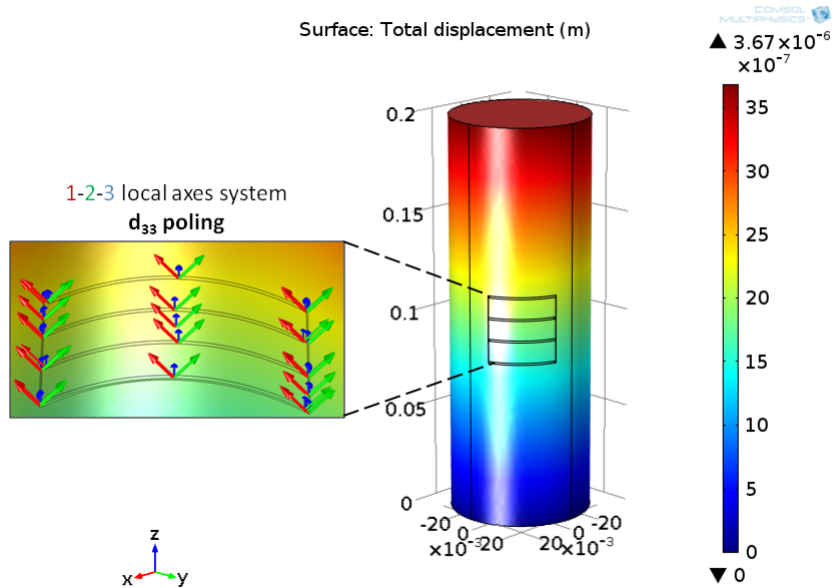


**Figure 3.6:** Surface displacement plot $[m]$ of the rod-patch FEM for $d_{33}$ operation $(F_t)$, the insert depicts the orientation of local material axes system with respect to the global axes system.

This was achieved by the cylindrical coordinate system transformation described in Equation 3.11[7].

$$
\begin{bmatrix} e_1 \\ e_2 \\ e_3 \end{bmatrix} = \begin{bmatrix} 0 & 0 & 1 \\ sin(tan^{-1}(X,Y)) & cos(tan^{-1}(X,Y)) & 0 \\ cos(tan^{-1}(X,Y)) & -sin(tan^{-1}(X,Y)) & 0 \end{bmatrix} \begin{bmatrix} e_X \\ e_Y \\ e_Z \end{bmatrix} \tag{3.11}
$$

Where in Equation 3.11, $\{e_X, e_Y, e_Z\}$ and $\{e_1, e_2, e_3\}$ are the set of unit vectors of the X-Y-Z and 1-2-3 axes systems, respectively.

Based on linear elastic theory, analytical equations for the strains developed at the outer (radial) surface of the host structure can be obtained [71]. These straightforward equations were used to verify the results of the numerical simulations.
The maximum shear strain $\gamma_{max}$ [−] developed at the rod's radial surface by a torsional moment $M_t$ [$Nm$] is described in Equation 3.12.

$$
\gamma_{max} = s_{55} \frac{2M_t}{\pi r_{rod}^3} \tag{3.12}
$$

Where in Equation 3.12, $\sigma_{55}$ is the shear compliance of the rod's material. Analogously, the normal strain $\epsilon_{max}$ developed due to the axial tensile force $F_t$ can be obtained by Equation 3.13.

$$
\epsilon_{max} = s_{33} \frac{F_t}{\pi r_{rod}^2} \tag{3.13}
$$

Where in Equation 3.13, $s_{33}$ is the longitudinal compliance of the rod's material.

**Patch on cantilever beam**

The second strain-driven energy harvesting case study governs a piezoelectric IDE patch on a cantilever beam ($L_{beam}$=20$cm$, $w_{beam}$=7$cm$, and $t_{beam}$=0.5$cm$). By adapting the patches' local axes system ($d_{15}$ or $d_{33}$ poling) and orientation by rotation, the generated energy by the patch operating at different strain states (and operation modes) can be assessed while the host structure is bended by a constant vertical tip force ($F_v$=50$N$).

The geometrical and material properties of the IDE patch are identical to the ones presented in the previous subsection on the set-up of the rod-patch FEM. As stated above, the patch is allowed to rotate on the beam's surface by $\theta_{rot}$ [°] with respect to the global Y-axis (clockwise positive). Henceforth, the local material coordinate system defined by Table 3.2 is adapted by rotating the local (1-2-3) axes system with $\theta_{rot}$ around the 2-axis for both operation modes. The local axes systems for the two operation modes ($d_{15}$ and $d_{33}$ poling) is illustrated by the inserts of Figure 3.7 for $\theta_{rot}$=25°.

The strain distribution variation is achieved by rotation of the patch and is based on (plane strain) strain transformations as explained in the subsequent paragraphs [71].

---

[7]The coordinate system transformation defined in Equation 3.11 was implemented in Comsol by means of a 'base vector coordinate system'.
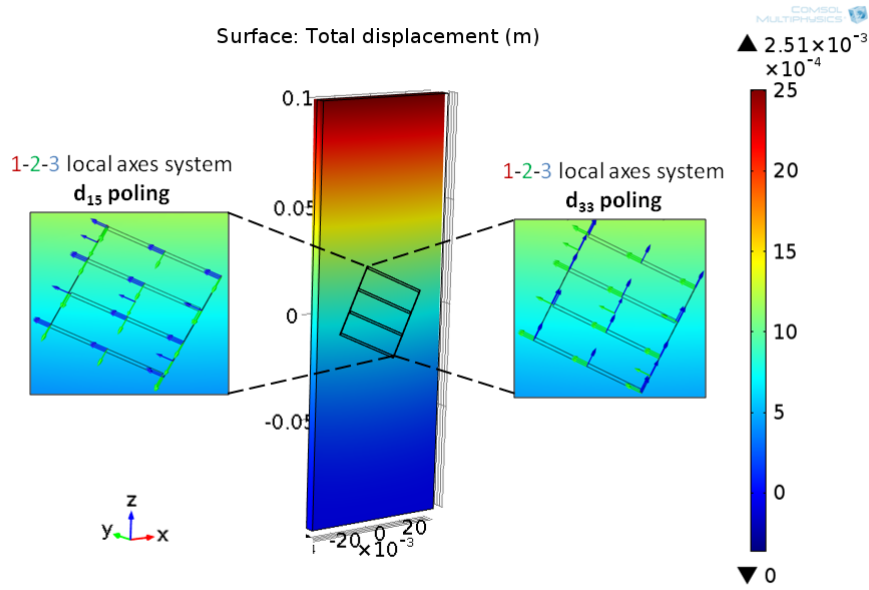
**Figure 3.7:** Surface displacement plot $[m]$ of the beam-patch FEM, the inserts represent orientation of local material axes system for $d_{15}$ (left) and $d_{33}$ (right) poled materials.

For an infinitesimal material element on the beam's surface (global X-Z plane), the normal ($\epsilon_1$) and shear ($\gamma_{23}$) strains with respect to the local $\theta_{rot}$-dependent 2-3 plane are determined in Equation 3.14 and 3.15, respectively, by applying the principle of (plane strain) strain transformation[8].

$$\epsilon_3 = \frac{\epsilon_X + \epsilon_Z}{2} - \frac{\epsilon_X - \epsilon_Z}{2}cos(2\theta_{rot}) + \gamma_{XZ}sin(2\theta_{rot}) \tag{3.14}$$

$$\gamma_{23} = (\epsilon_X - \epsilon_Z)sin(2\theta_{rot}) + \gamma_{XZ}cos(2\theta_{rot}) \tag{3.15}$$

Where in Equation 3.14 and 3.15, $\epsilon_X$, $\epsilon_Z$, and $\gamma_{XZ}$ refer to the in-plane (X-Z) transverse, normal, and shear strain, respectively, acting on the differential material element.

To apply this (plane strain) strain transformation method to change the strain state of the energy harvesting patch, two primary assumptions were made[9]:

1. The patch is assumed to be perfectly bonded to the host structure's surface. Although this assumption is valid for the numerical model, the interface between the patch and the host structure will never be perfect in reality. Consequently, this has to be taken into account when experimental tests would be performed to validate the numerical results.

---

[8]It is assumed that the out-of plane normal strain induced by the host structure's *Poisson*'s ratio can be neglected. Moreover, Equation 3.14 and 3.15 are valid for the $d_{33}$ local axes system definition defined in Table 3.2. The analysis for the $d_{15}$ axes system is completely analogous.

[9]These assumptions also apply for the rod-patch FEM study. However, it is presumed that they have a larger impact on the results of the patch-beam case study as a result of the applied strain transformation technique and are therefore stated in this subsection.

2. The net compliance of the patch, in terms of its material and geometrical properties, is neglected. In this way, it can be assumed that solely the deformation of the beam rules the resulting strain acting on the patch. This assumption affects the numerical as well as the experimental results as both the FEM and the real beam-patch system are characterized with a non-zero compliance and finite dimensions.

Taking the considerations above into account and recalling that the cantilever beam is deformed by a single vertical tip force $F_v$, the non-rotated patch can be described as a biaxially-loaded material element for which the strain distribution is described by Equation 3.16 ($\epsilon_X$), 3.17 ($\epsilon_Z$), and 3.18 ($\gamma_{XZ}$)[10].

$$\epsilon_X = s_{31} \frac{-6(Z - \frac{L_{beam}}{2})}{w_{beam}t_{beam}^2} F_v \tag{3.16}$$

$$\epsilon_Z = s_{33} \frac{-6(Z - \frac{L_{beam}}{2})}{w_{beam}t_{beam}^2} F_v \tag{3.17}$$

$$\gamma_{XZ} = 0 \tag{3.18}$$

Where in Equation 3.16, $s_{31}$ is the transverse compliance of the beam's material and $Z$ $[m]$ is the $Z$-axis coordinate.

Hence, by applying Equation 3.14 and 3.15, the patches' strain distribution is altered by rotation. The strain distribution transformation is visualized in Figure 3.8 for a normalized, though representative biaxial strain distribution ($\epsilon_X$=-0.3, $\epsilon_X$=1, $\gamma_{XZ}$=0). The normal strain has its maximum value at $\theta_{rot}$=0°, whereas the maximum shear strain is reached at $\theta_{rot}$=45°. Consequently, the patch was rotated from $\theta_{rot}$=0° to $\theta_{rot}$=45° for the strain-driven energy harvesting case study.
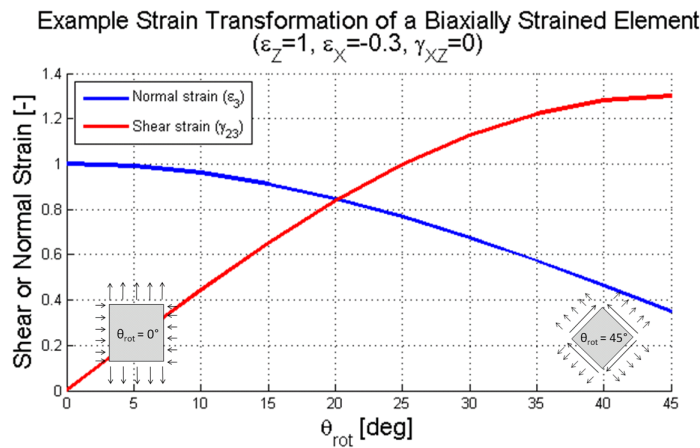


**Figure 3.8:** Strain transformation example of a biaxially strained material element ($\epsilon_X$=-0.3, $\epsilon_X$=1, $\gamma_{XZ}$=0) representative for the present beam-patch system analysis. Note that the local (1-2-3) axes system definition is conform the $d_{33}$ poling system as presented in Table 3.2.

---

[10]Analogous to the rod-patch case study, linear elastic deformation is assumed.

## 3.3    Results and discussion

### 3.3.1    IDE patch simulations

The individual patch simulations aimed to explore the effect of employing interdigitated electrodes on the patches' energy harvesting performance for $d_{15}$ versus $d_{33}$ operation. In addition, the influence of the electrode lay-out in terms of electrode finger width and spacing on the energy-based performance of the harvesting patch was investigated. Within the pre-determined $w_f$ and $\frac{w_f}{s_f}$ ranges, the optimal combination of $w_s$ and $\frac{w_f}{s_f}$ values was obtained for the numerical energy harvesting case studies.

**Verification of the IDE patch simulations**
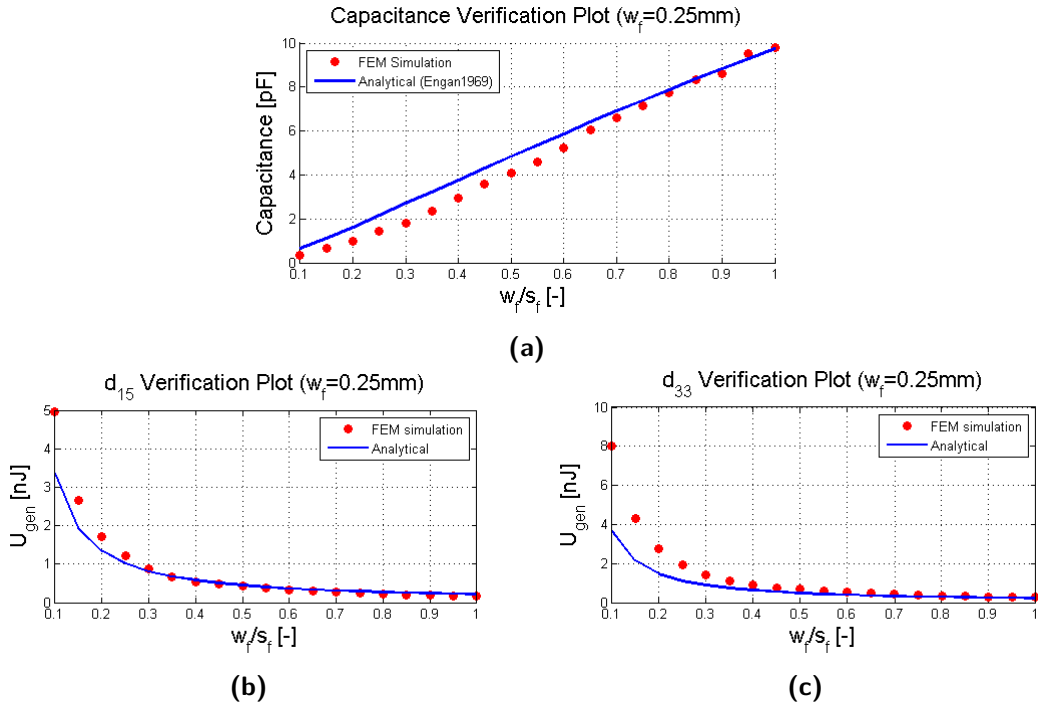
Prior to the presentation and discussion of the results of the IDE patch simulations, the results of these simulations were verified by aid of the analytical theoretical framework presented in Section 3.2.1.



**Figure 3.9:** IDE study verification plots for a fixed finger width ($w_f$=0.25$mm$) and variable finger spacing ($\frac{w_f}{s_f}$=[0.1:0.05:1]): capacitance verification plot (a), generated energy verification plot for $d_{15}$-mode operation (b), generated energy verification plot for $d_{33}$-mode operation (c).

First of all, the numerically obtained free capacitance of the IDE system were compared with the results of *Engan*'s model as depicted in Figure 3.9a. It is clear that the numerical results correspond to the analytical ones for small finger spacings ($\frac{w_f}{s_f} \geq 0.6$). Though, for larger spacings, the analytical model overestimates the system's $C_{free}$ with respect to the numerical model. This relative error between the $C_{free}$ results of two models increases with increasing finger spacings (decreasing $\frac{w_f}{s_f}$)[11].

---

[11]The increasing deviation between the numerical and analytical $C_{free}$ results for increasing finger spacings resulted, in combination with the occurrence of unrealistic/impractical high voltages at larger spacings (lower $C_{free}$ values), in the $\frac{w_f}{s_f}$=0.1 lower bound for the present IDE geometry study.

A possible cause for the observed discrepancy between the numerically and analytically obtained $C_{free}$ figures at small finger spacings can be that the one dimensional analytical model does not account for the presence of the side electrodes, which affects the total capacitance of the IDE system too. This small, though significant effect is more present at small finger spacings for which the absolute value of $C_{free}$ decreases.

The generated energy ($U_{gen}$) figures resulting from the finite element simulations were compared with the ones from the analytical model for each of the two loading cases. Analogous to the capacitance verification study, the numerical and analytical $U_{gen}$ values are plotted for a fixed finger width ($w_f$=0.25$mm$) and variable finger spacing (see Figure 3.9b and c).
The numerical model matches the analytical one for small finger spacings. However, commencing at a $\frac{w_f}{s_f}$ ratio equal to 0.5, a deviation between the results of the two models is present which increases for decreasing $\frac{w_f}{s_f}$ values. The aforementioned $C_{free}$ underprediction of the analytical model for low $\frac{w_f}{s_f}$ values is the root cause of the observed deviation in $U_{gen}$ figures (see Equation 1.16 and 3.5).
Notwithstanding the significant errors in absolute $U_{gen}$ values of the two models at large finger spacings ($RE_{max}$=30% for $d_{15}$, $RE_{max}$=50% for $d_{33}$), the FEM results can be used to determine the effect of the IDE geometry (for the investigated $\frac{w_f}{s_f}$ interval) as there is a good agreement at small finger spacings and an identical trend for larger ones.
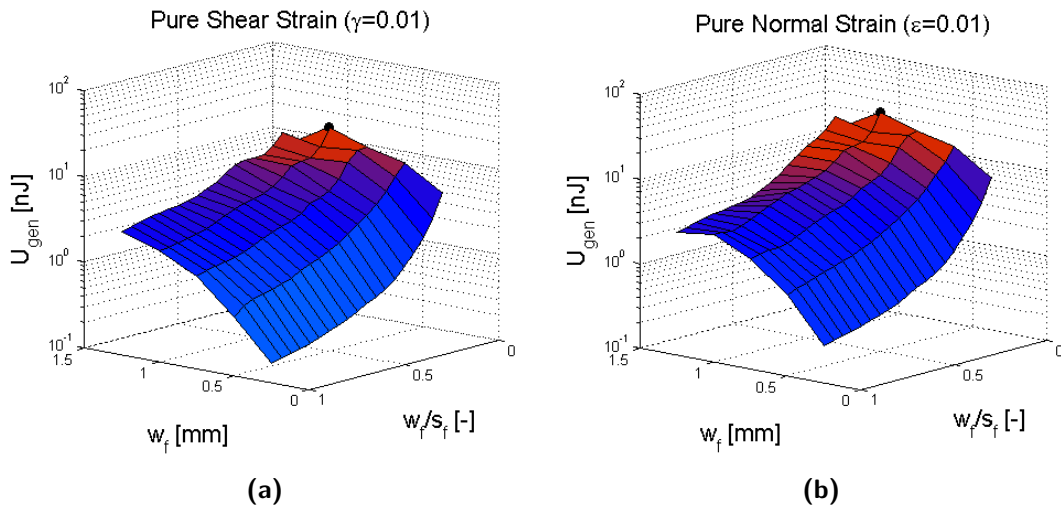


**Figure 3.10:** Effect of the IDE lay-out on the net generated energy of the harvesting patch: pure shear strain ($d_{15}$) operation (a) and pure normal strain ($d_{33}$) operation (b).

**Effect of the IDE (geometry) on $U_{gen}$**

The effect of the electrode finger width and spacing on the energy-based performance of the IDE harvesting patch is illustrated in Figure 3.10a and b for the two investigated $d_{15}$ (pure shear strain) and $d_{33}$ (pure normal strain) operations, respectively.

One can observe that $U_{gen}$ increases for increasing finger spacings. This effect, which is also visible on Figure 3.9b and c, is caused by the increased capacitance at larger spacings.

Furthermore, the absolute value of the finger width influences the energy generating capability of the patch too. For the pure normal strain operation ($d_{33}$ poling), $U_{gen}$ increases for increasing $w_f$ values up to $w_f$=1cm. After this 'local optimum' the $\frac{U_{gen}}{w_f}|_{\frac{w_f}{s_f}}$ slope becomes negative. Henceforth, the maximum generated energy, within the investigated $w_f$ and $\frac{w_f}{s_f}$ ranges, is obtained at $\{w_f$=1cm, $\frac{w_f}{s_f}$=0.1$\}$.

For the pure shear strain operation ($d_{15}$ poling), the $\frac{U_{gen}}{w_f}|_{\frac{w_f}{s_f}}$ trend is slightly different. For $\frac{w_f}{s_f}$ values up to 0.2, the maximum $U_{gen}$ value is reached at the highest (investigated) $w_f$ value. Yet, for $\frac{w_f}{s_f}$=0.1, the highest generated energy value is attained at $w_f$=1cm, coinciding with the maximum $U_{gen}$ value. Consequently, the $\{w_f$=1cm, $\frac{w_f}{s_f}$=0.1$\}$ IDE geometry combination also results for $d_{15}$ operation in the highest generated energy value for the investigated $w_f$ and $\frac{w_f}{s_f}$ ranges.

The $\{w_f$=1cm, $\frac{w_f}{s_f}$=0.1$\}$ IDE geometry combination corresponds to a $U_{gen}$ figure equal to 2.71$nJ$ for the pure normal 1% strain case, while 1.65$nJ$ is harvested for the 1% pure shear strain case. Consequently, the obtained strain-driven energy densities by IDE operations ($W_{el}^{S,IDE}$ $[\frac{J}{m^3}]$) are equal to 0.355$\frac{J}{m^3}$ ($d_{15}$) and 0.602$\frac{J}{m^3}$ ($d_{33}$). These values can be compared with the reference, material-based strain-driven energy densities for 1% strain operations (see Figure 3.1) as presented in Table 3.4.

Although $d_{15}$-mode operation clearly results in lower $U_{gen}$ values in absolute sense, the energy density-based analysis indicates that by using IDE the material is more efficiently employed when $d_{15}$ rather than $d_{33}$ operations are envisioned.

|          | $W_{el}^{S,IDE}$ $[\frac{J}{m^3}]$ | $W_{el}^{S}$ $[\frac{J}{m^3}]$ | $\eta_{IDE}$ $[\%]$ |
|----------|-----------|-----------|-----------|
| $d_{15}$ | 0.355     | 2.56      | 13.9      |
| $d_{33}$ | 0.602     | 11.04     | 5.5       |

**Table 3.4:** Comparison of the simulated IDE versus reference strain-driven energy densities. $\eta_{IDE}$=$\frac{W_{el}^{S,IDE}}{W_{el}^{S}}$×100%.

### 3.3.2 Case studies

This subsection presents and discusses the main results of the strain-driven energy harvesting case studies.

**Patch on cantilever rod**

Table 3.5 summarizes the outcome of numerical rod-patch energy harvesting case study. First of all, the absolute values of the applied $M_v$ and $F_t$ loads were varied to obtain a constant elastic deformation energy ($U_{el}$=145$nJ$) in the strained patch for both operation modes. This resulted in fixed $M_t$ (=50$Nm$) and $F_t$ (=5$kN$) values.

Next, the shear $\gamma_{23,host}^{an}$ and normal $\epsilon_{23,host}^{an}$ strain figures determined by the analytical framework presented in Section 3.2.1 (Equation 3.13 and 3.12) were used to verify the numerically obtained strains ($\gamma_{23,host}^{FEM}$ and normal $\epsilon_{23,host}^{FEM}$) acting on the host structure. As reported in Table 3.5, good agreement was found for both operation modes.
Likewise, the $\gamma_{23,host}^{FEM}$ and $\epsilon_{23,host}^{FEM}$ figures corresponded to the average strains values experienced by the patch ($\gamma_{23,patch}^{FEM}$ and $\epsilon_{33,patch}^{FEM}$), indicating that strains developed in the host structure are efficiently transferred to the compliant patch.

Lastly, the generated energy by the patch was retrieved. Application of the torsional moment ($d_{15}$ operation) results in $U_{gen}$=0.19$nJ$, whereas the same patch generates 0.94$nJ$ upon axial loading of the rod ($d_{33}$ operation). At the first sight, the lower $U_{gen}$ value can be attributed to the implied $\frac{d_{15}}{d_{33}}$ (=0.625) piezoelectric charge constant ratio of the patches' composite material. However, at the same time, the ratio of the shear strain developed in the patch for $d_{15}$ operation over the normal strain developed for $d_{33}$ operation ($\frac{\gamma_{23,patch}^{FEM}}{\epsilon_{33,patch}^{FEM}}$) equals 1.39. Hence, one would expect that the effect of the two ratios would compensate each other, resulting in similar generated energy values for both operation modes.

A possible cause for the relatively low $U_{gen}$ value obtained for $d_{15}$ operation could be the strain state at the patch-rod interface. The non-uniform strain distribution could be a source of charge/voltage cancellation, decreasing the net generated energy by the patch. The use of interdigitated electrodes could also play a (minor) role. As a result of the (pure) shear deformation of the square patch, its electrode fingers will make an angle with the (fixed) local 1-axis (see Figure 3.11), resulting in a decreased effectiveness of the charge collecting electrodes.

| Mode | Load | $U_{el}$ [$nJ$] | $\epsilon_{ij,patch}^{FEM}$ [$\cdot10^{-5}$] | $\epsilon_{ij,host}^{FEM}$ [$\cdot10^{-5}$] | $\epsilon_{ij,host}^{an}$ [$\cdot10^{-5}$] | $U_{gen}$ [$pJ$] |
|---|---|---|---|---|---|---|
| $d_{15}$ | $M_t$=50$Nm$ | 145 | $\gamma_{23}$=2.542 | $\gamma_{23}$=2.539 | $\gamma_{23}$=2.540 | 0.19 |
| $d_{33}$ | $F_t$=5$kN$ | 145 | $\epsilon_{33}$=1.83 | $\epsilon_{33}$=1.85 | $\epsilon_{33}$=1.86 | 0.94 |

**Table 3.5:** Summary of the results of the rod-patch FEA study.
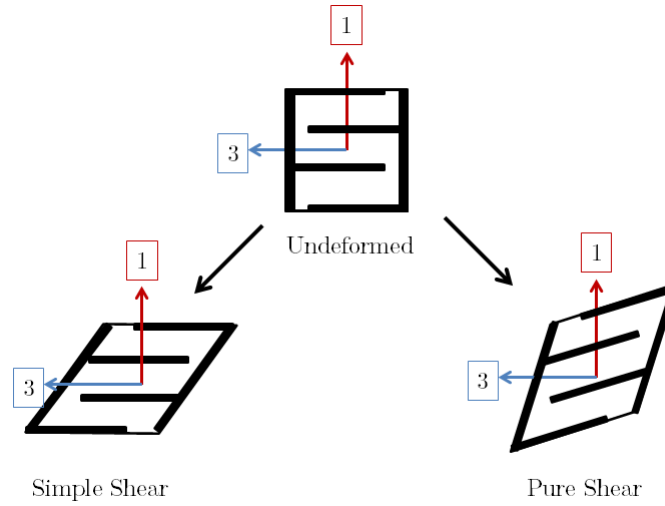
**Figure 3.11:** Simple versus pure shear deformation of the IDE patch.

**Patch on cantilever beam**

By adapting the patches' local axes system ($d_{15}$ or $d_{33}$ poling) and strain distribution, the generated energy by the patch operating at different modes could be quantified and compared for a constant vertical tip force ($F_v$) acting on the cantilever beam host structure.

The net generated energy ($U_{gen}$) by the patch at different rotation angles ($\theta_{rot}$=[0:5:45°]) is depicted in Figure 3.12. Both the absolute $U_{gen}$ values at fixed rotation angles and the $U_{gen}$-$\theta_{rot}$ are not conform the anticipated strain transformation analogy (see Figure 3.8). That is, one would expect that for both the shear and normal operation modes the numerically obtained $U_{gen}$-$\theta_{rot}$ data could be mapped to the shear and normal strain transformation relations, respectively.

For example, the generated energy for the shear mode operation ($d_{15}$ poling) is expected to be zero at $\theta_{rot}$=0° and increase, with a trend conform the anticipated shear strain versus rotation angle, to its maximum value at $\theta_{rot}$=45°. This is clearly not the case for the simulated $d_{15}$ poled $U_{gen}$-$\theta_{rot}$ data; the maximum $U_{gen}$ value is approximately obtained at $\theta_{rot}$=15°, whereas $\theta_{rot}$=45° returns the minimum $U_{gen}$ value.
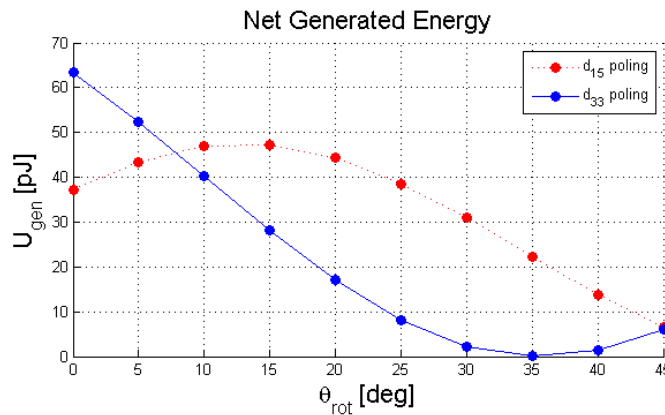


**Figure 3.12:** Net generated energy by the ($d_{15}$ or $d_{33}$ poled) patch for the investigated $\theta_{rot}$ interval.
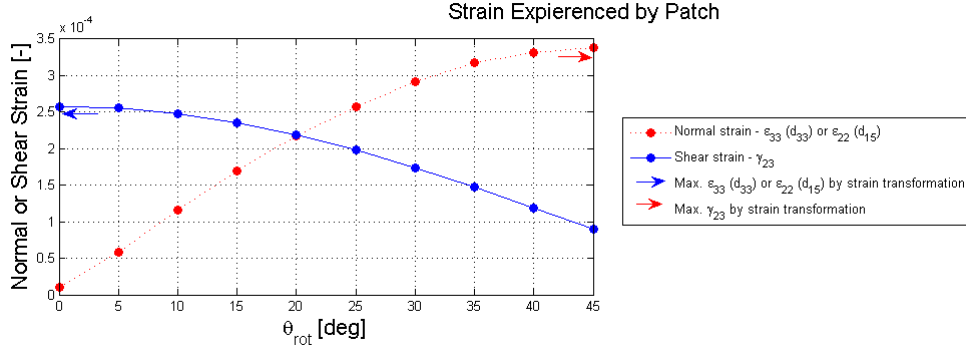
**Figure 3.13:** Strain experienced by the patch for the investigated $\theta_{rot}$ interval. The arrows denote the normal ($\theta_{rot}$=0°) and shear ($\theta_{rot}$=45°) strain values based on the strain transformation principle (Equation 3.14 and 3.15).

Two procedures were performed to investigate these unexpected results. Firstly, the actual strain distribution of the rotated patch was retrieved and compared with the anticipated biaxially (plane strain) strain transformation to test the applicability of the strain transformation principle. Secondly, the individual contribution of each $d_{ij}$-mode to the generated energy was investigated to check whether the results can (partially) be attributed to the simultaneous coupling of the activated $d_{ij}$-modes.

The simulated patches' surface strain states at different rotation angles are plotted in Figure 3.13. It is clear that the change in shear and normal strain is in close agreement with the anticipated (plane strain) strain transformation (see Figure 3.8). Henceforth, the applicability of the (plane strain) strain transformation principle holds and cannot be used to explain the unanticipated net generated energy results plotted in Figure 3.12.

Next, all but the piezoelectric charge constants of interest ($d_{ij}$ for the $d_{ij}$ poled patch) in the simulated piezoelectric coupling matrix were set to zero. This approach allows one to observe the individual contribution of the $d_{15}$- or $d_{33}$-mode to the generated energy by the $d_{15}$ or $d_{33}$ poled patch, respectively, as the simultaneous coupling by the different operation modes is ruled out[12].
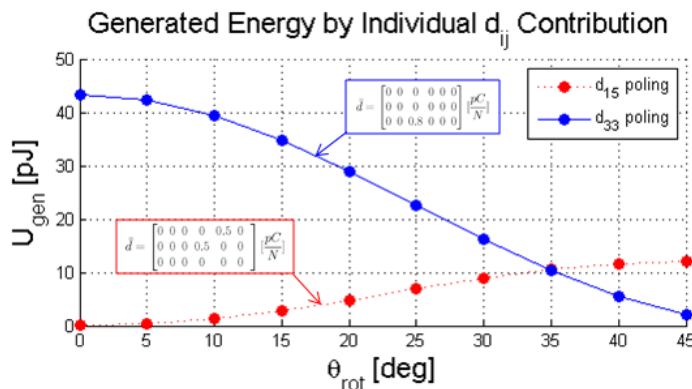


**Figure 3.14:** Individual $d_{15}$ or $d_{33}$ contribution to the generated energy for the $d_{15}$ or $d_{33}$ poled patch.

---

[12]This procedure cannot be performed by experiment as real piezoelectric material systems do not offer the flexibility to alter their coupling matrices to this extent. Henceforth, this procedure can be seen as an

The outcome of this study is illustrated in Figure 3.14. One can observe that the trend (and maxima) of the resulting individual $U_{gen}$-$\theta_{rot}$ data can be related to actual strain state of the patch (see Figure 3.13). Though, the $U_{gen}$ figures for $d_{15}$ operation are much lower than one would expect from the patches' strain distribution. Two possible causes for this behaviour were stated in the previous subsection on the results of the rod-patch case study.

Lastly, the procedure of separating the individual $d_{ij}$ contributions to $U_{gen}$ was performed for each of the three modes. The resulting individual $U_{gen}$ values were summed resulting in cumulative $U_{gen}$ data for the $d_{15}$ and $d_{33}$ poled patches.
The outcome of this virtual approach is illustrated in Figure 3.15a ($d_{15}$ poled patch) and b ($d_{33}$ poled patch). One can clearly see that the cumulative trend as well as the $\theta_{rot}$ locations of the cumulative $U_{gen}$ minima and maxima, are in close agreement with the individual $d_{ij}$ data depicted in Figure 3.14 [13].

At this point, there is no solid explanation for the unanticipated trends and local minima/-maxima of the net generated energy figures (see Figure 3.15). Still, by comparing the net with the (expected) cumulative $U_{gen}$ data, one can presume the presence of charge or voltage cancellation/augmentation as predicted by the finite element simulations. A crucial question would be whether the numerical computations are an accurate representation of the physical reality. That is, if one would test the given beam-patch system by experiment, would the outcome be in agreement with the intuitive cumulative or the unanticipated net energy data obtained by simulation? Moreover, it would be of interest to test the effect of changing the finite element formulations within the Comsol software or the perform the simulations by a another FEM package.
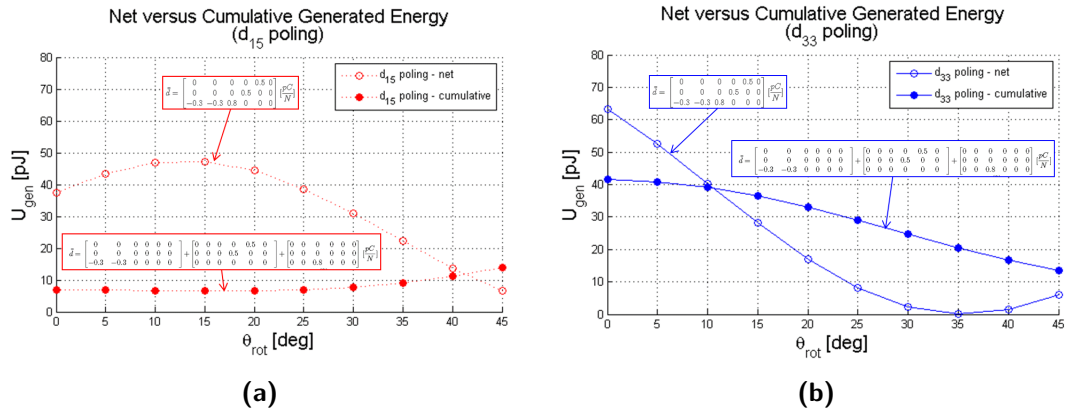


**Figure 3.15:** Net versus cumulative $d_{ij}$ generated energy: $U_{gen}$ versus $\theta_{rot}$ for $d_{15}$ poled patch (a), $U_{gen}$ versus $\theta_{rot}$ for $d_{33}$ poled patch (b).

---

attractive feature of the performed numerical (finite element) simulations.

[13] Some deviation between the individual and cumulative $U_{gen}$ figures can be observed in terms of absolute values and trend at the minima (e.g. $\theta_{rot}=0°$ for the $d_{15}$ poled patch).

## 3.4   Conclusions Chapter 3

This section concludes the chapter on the numerical performance assessment of a composite IDE energy harvesting patch under shear versus normal static strain-driven loading conditions.

Finite elements simulations revealed that a particulate composite (PZT5A4-epoxy, $v_f$=0.2) patch, provided with an optimal electrode finger width and spacing, is characterized with a $0.36\frac{J}{m^3}$ or $0.60\frac{J}{m^3}$ energy generating density when excited by either a static 1% shear or normal strain, respectively. Although $d_{15}$ (shear strain) operations clearly result in lower absolute generated energy figures with respect to conventional $d_{33}$ (normal strain) loading conditions, the material is more efficiently employed when operated in the $d_{15}$-mode for the investigated IDE patch concept.

The second part of the study addressed two (shear versus normal) strain-driven energy harvesting case studies.
The first case investigated a composite IDE patch attached to a cantilever rod host structure. By altering the external load on the rod's end and adapting the poling orientation of the simulated composite material, the energy-based performance of the patch load by pure shear or normal strains could be compared. Accounting for the reduced shear mode coupling of the simulated (particulate) composite material ($\frac{d_{15}}{d_{33}}$=0.625) conform the characterization study presented in Chapter 2, the rod-patch simulations indicate, one more, that loading the patch in shear instead of normal strain-driven conditions lowers the harvested energy by the patch.

The second case study governed a cantilever beam bended by a single vertical tip force which was provided with the same compliant energy harvesting patch. Applying the concept of (plane strain) strain transformation, the energy-based performance of the patch at varying strain states though constant external loading on the host structure was investigated. Although the simulated strain states of the rotated patch are conform the presumed strain transformation analogy, the (net) generated energy figures cannot be related to the obtained strain states and are therefore unexpected. Additional finite element simulations indicate the presence of charge or voltage cancellation/augmentation. Further numerical simulations and experimental validation tests as part of future work could provide new insights on these unanticipated results.

Chapter 4

# Conclusions and recommendations

This thesis investigated the employment of compliant piezoelectric material systems for shear-strain driven energy harvesting applications. The first part (Chapter 2) of the study focused on the shear mode property characterization of particulate and fiber piezoelectric composites, while the second part (Chapter 3) addressed the performance assessment of a compliant piezoelectric energy harvesting patch provided with interdigitated electrodes (IDE) under static shear versus normal strain-driven loading schemes.

To determine the piezoelectric coupling properties of the selected composite material systems, an IDE-based impedance measurement method was developed. The novel method proved to be a sound alternative for the standard impedance-based shear measurement method as verified and validated by means of a reference PZT material. The method is adapted to the standard piezoelectric composite production method and is particularly suitable for thin and costly samples as no cutting operations, inevitably leading to material losses and increased risks of sample fracture, are required.

However, it was found out that the impedance-based method cannot be applied for the characterization of piezoelectric shear properties of particulate composites as they failed to exhibit resonance behaviour. Numerical effective property simulations as well as complementary experimental quasi-static measurements indicated that this can be attributed to the inherently low (shear) piezoelectric coupling properties of these material systems.
Resonance frequencies were present on the impedance spectra of the fiber composite samples. Yet, the observed frequencies do not coincide with numerically simulated pure shear resonance frequencies. Consequently, future work to determine the physical cause behind the unexpected values of the observed frequencies is recommended to establish the validity of the novel impedance-based method for the shear mode property characterization of piezoelectric fiber composites.

Moreover, both the numerical effective property simulations and the experimental quasi-static measurements indicated that, in contrast to the effective $\frac{d_{31}}{d_{33}}$ ratio, the particulate composite's effective $\frac{d_{15}}{d_{33}}$ ratio at fixed piezoelectric material volume fractions, is lower than the bulk piezoelectric material's $\frac{d_{15}}{d_{33}}$ ratio. Consequently, the anticipated advantage of employing shear-mode for increased electromechanical coupling efficiency, is not valid in the case of

piezoelectric particulate composites.

For the second part of this work, finite element simulations were performed to determine the influence of employing interdigitated electrode (IDE) on the energy harvesting performance of a compliant patch operated in a pure shear ($d_{15}$) as well as a normal ($d_{33}$) strain-driven loading environment. It was demonstrated that a particulate composite (PZT5A4-epoxy, $v_f$=0.2) patch, provided with an optimal electrode finger width and spacing, is characterized with a $0.36\frac{J}{m^3}$ or $0.6\frac{J}{m^3}$ energy density when operated at either a (static) pure 1% shear or normal strain, respectively. Although $d_{15}$ conditions clearly result in low absolute generated energy figures in comparison with conventional $d_{33}$ operations, the composite material is more efficiently operated in $d_{15}$ mode for the investigated IDE concept.

Furthermore, strain-driven energy harvesting case studies for the IDE patch were developed and simulated. The case studies assessed the influence of complex strain states on the patches' energy-based performance and suggested practical experimental validation schemes for the Chapter's purely numerical analysis.
Unanticipated results were obtained for the bended cantilever beam case study. Although the simulated strain states of the rotated patch are conform the applied strain transformation principle, the generated energy versus rotation angle data cannot be related to the obtained strain state variation.

Lastly, some paramount additional recommendations for future work on this topic can be formulated.
As stated above, the numerical and experimental analyses demonstrated a significant difference in shear mode coupling between the particulate (0-3) and fiber (1-3) piezoelectric composites in terms of resonance behaviour as well as $d_{15}$ magnitude at varying piezoelectric material filling grades. Therefore, characterization of quasi 1-3 composites produced by dielectrophoresis could be of interest to further examine the influence of the active material's connectivity on the effective composite material's shear mode properties.

Concerning the numerical simulations, one could extend the reduced volume element definitions employed for the effective property simulations by, for instance, taking interfacial effects, interparticle distances, and particle shapes into account. Moreover, one could employ more complex (semi-)analytical models such as the *Mori-Tanaka* method to verify the finite element results. To further improve the impedance-based finite element simulations, one could include the effect of loss by use of complex permittivity, compliance, and piezoelectric coupling matrices.

Concerning the experimental measurements, it is highly recommended to study the effect of the sample ring geometries for the quasi-static $d_{15}$ measurements as well as to experimentally validate the unanticipated results of the numerical beam-patch energy harvesting case study.

# References

[1] Cook-Chennault, K.A., Thambi, N., Bitetto, M.A. and Hameyie, E.B., "Piezoelectric energy harvesting: a green and clean alternative for sustained power production," *Bulletin of Science, Technology & Society*, vol. 28, pp. 496–509, 2008.

[2] Anton, S. and Sodano, H., "A review of power harvesting using piezoelectric materials (2003-2006)," *Smart Materials and Structures*, vol. 16, pp. 1–21, 2007.

[3] Erturk, A. and Inman, D.J., *Piezoelectric Energy Harvesting.* West Sussex (UK): John Wiley & Sons, Ltd., 2011.

[4] Kim, H.S., Kim, J.-H. and Kim, J., "A review of piezoelectric energy harvesting based on vibration," *International Journal of Precision Engineering and Manufacturing*, vol. 12, pp. 1129–1141, 2011.

[5] Mo, C. and Davidson, J., "Energy harvesting technologies for structural health monitoring applications," *1st IEEE Conference on Technologies for Sustainability (SusTech)*, vol. 1, pp. 192–198, 2013.

[6] Dagdeviren, C., Yang, B.D., Su, Y., Tran, P.L., Joe, P., Anderson, E., Xia, J., Doraiswamy, V., Dehdashti, B., Feng, X., Lu, B., Poston, R., Khalpey, Z., Ghaffari, R., Huang, Y. , Slepian, M.J. and Rogers, J.A., "Conformal piezoelectric energy harvesting and storage from motions of the heart, lung, and diaphragm," *Proceedings of the National Academy of Sciences of the United States of America*, vol. 111, pp. 1927–1932, 2014.

[7] Mitcheson, B., Yeatman, E.M., Rao, G.K., Holmes, A.S., Green, T.C., "Human and machine motion for wireless electronic devices," *Proceedings of the IEEE*, vol. 96, pp. 1457–1486, 2008.

[8] Marsic, V. and Giuliano, A., "Energy harvesting technology to power wireless sensors for aircraft structural load monitoring," *Cranfield Innovative Manufacturing Research Centre.* (poster presentation).

[9] Priya, S. and Inman, D.J., *Energy Harvesting Technologies.* New York (NY, USA): Springer Science + Business Media, 2009.

[10] Bowen, C.R., Kim, H.A., Weaver, P.M. and Dunn, S., "Piezoelectric and ferroelectric materials and structures for energy harvesting applications," *Energy & Environmental Science*, vol. 7, pp. 25–44, 2014.

[11] Holterman, J. and Groen, P., *Piezoelectric Materials and Applications.* Apeldoorn (the Netherlands): Stichting Applied Piezo, 2013.

[12] Curie, J. and Curie, P., "Développement, par pression, de l'électricité polaire dans les cristaux hémièdres à faces inclinées," *Comptes rendus de l'Académie des Sciences*, vol. 91, p. 383, 1880.

[13] Jaffe, B., Cook, W.R. Jr. and Jaffe, H., *Piezoelectric Ceramics.* London (UK): Academic Press, 1971.

[14] Morgan Advanced Materials, "Piezoelectric Ceramics - Technical Brochure." http://www.morganelectroceramics.com.

[15] The Institute of Electrical and Electronics Engineers Inc., "IEEE Standard on Piezo-electricity," 1987. New York (NY, USA).

[16] Richards, C., Anderson, M.J., Bahr, D.F. and Richards, R.F., "Efficiency of energy conversion for devices containing a piezoelectric component," *Journal of Micromechanics and Microengineering*, vol. 14, pp. 717–721, 2004.

[17] Uchino, K. and Hirose, S., "Loss mechanisms in piezoelectrics: how to measure different losses seperately," *IEEE Transactions of Ultrasonics, Ferroelectrics, and Frequency Control*, vol. 48, pp. 307–321, 2001.

[18] Beeby, S., Tudor, M.J. and White, N.M., "Energy harvesting vibration sources for microsystems applications," *Measurement Science and Technology*, vol. 17, 2006. R175–R195.

[19] Patel, I., Siores, E. and Shah, T., "Utilisation of smart polymers and ceramic based piezoelectric materials for scavenging wasted energy," *Sensors and Actuators A: Physical*, vol. 159, pp. 213–218, 2010.

[20] Safari, A., Jadidian, B. and Akdogan, E.K., *Piezoelectric Composites for Transducer Applications in 'Comprehensive Composite Materials' .* Oxford (UK): Elsevier Science Ltd., 2012.

[21] Randall, C.A., Kim, N. Kucera, J.-P., Cao, W. and Shrout, T.R., "Intrinsic and extrinsic size effects in fine-grained morphotropic-phase-boundary lead zirconate titanate ceramics," *Journal of the American Ceramic Society*, vol. 88, pp. 677–688, 1998.

[22] Chen, Q.X. and Payne, P.A., "Industrial applications of piezoelectric polymer transducers," *Measurement Science and Technology*, vol. 6, pp. 249–267, 1994.

[23] Kawai, H., "The piezoelectricity of poly(vinylidene fluoride)," *The Japanese Journal of Applied Physics*, vol. 8, pp. 975–976, 1969.

[24] Zhu, G., Zeng, Z., Zhang, L., Yan, X., "Piezoelectricity in $\beta$-phase PVDF crystals: a molucular simulation study," *Computational Materials Science*, vol. 44, pp. 224–229, 2008.

[25] van den Ende, D.A., van Kempen, S.E., Wu, X., Groen, W.A., Randall, C.A. and van der Zwaag, S., "Dielectrophoretically structured piezoelectric composites with high aspect ratio piezoelectric particles inclusions," *Journal of Applied Physics*, vol. 111, 2012. 124107 (13pp.).

[26] van den Ende, D., *Structured Piezoelectric Composites - Materials and Applications.* Phd thesis, Delft University of Technology (Delft, the Netherlands), June 2012.

[27] Newnham, R.E., Skinner, D.P. and Cross, L.E., "Connectivity and piezoelectric-pyroelectric composites," *Materials Research Bulletin*, vol. 13, pp. 525–536, 1978.

[28] Klicker, K.A., Biggers, J.V. and Newnham, R.E., "Composites of PZT and epoxy for hydrostatic transducer applications," *Journal of the American Ceramic Society*, vol. 64, pp. 5–9, 1981.

[29] van den Ende, D.A., van de Wiel, H.J., Groen, W.A. and van der Zwaag, S., "Direct strain energy harvesting in automobile tires using piezoelectric PZT–polymer composites," *Smart Materials and Structures*, vol. 21, 2012. 015011 (11pp.).

[30] Rödig, T. and Schönecker, A., "A survey on piezoelectric ceramics for generator applications," *Journal of the American Ceramic Society*, vol. 93, pp. 901–912, 2010.

[31] Goldschmidtboeing, F. and Woias, P., "Characterization of different beam shapes for piezoelectric energy harvesting," *Journal of Micromechanics and Microengineering*, vol. 18, p. 104013, 2008.

[32] Baker, J., Roundy, S. and Wright, P.K., "Alternative geometries for increasing power density in vibration energy scavenging," *American Institute of Aeronautics and Astronautics (AIAA)*, vol. 1, pp. 1–12, 2005.

[33] Sun, H., de Vries, T.J.A., de Vries, R. and van Dalen, H., "Energetic optimization of a piezo-based touch-operated button for man-machine interfaces," *Smart Materials and Structures*, vol. 21, 2012. 035026 (8pp.).

[34] Kim, S., Clark, W.W., Wang, Q.-M., "Piezoelectric energy harvesting with a clamped circular plate: Analysis," *Journal of Intelligent Material Systems and Structures*, vol. 16, pp. 847–854, 2005.

[35] Kim, S., Clark, W.W., Wang, Q.-M., "Piezoelectric energy harvesting with a clamped circular plate: Experimental study," *Journal of Intelligent Material Systems and Structures*, vol. 16, pp. 855–863, 2005.

[36] Inman, D.J., *Engineering Vibrations.* Upper Saddle River (NJ, USA): Pearson Education, 2013.

[37] Schenck, N.S. and Paradiso, J.A., "Energy harvesting with shoe-mounted piezoelectrics," *IEEE Micro*, vol. 16, pp. 30–42, 2001.

[38] Kim, H.W., Batra, A., Priya, S., Uchino, K., Markley, D., Newnham, R.E. and Hofmann, H.F., "Energy harvesting using a piezoelectric cymbal transducer in dynamic environment," *Japanese Journal of Applied Physics*, vol. 43, pp. 6178–6183, 2004.

[39] Priya, S., "Advances in energy harvesting using low profile piezoelectric transducers," *Journal of Electroceramics*, vol. 19, pp. 167–184, 2007.

[40] Guyomar, D. and Lallart, M., "Recent progress in piezoelectric conversion and energy harvesting using nonlinear electronic interfaces and issues in small scale implementation," *Micromachines*, vol. 2, pp. 274–294, 2001.

[41] Somiya, T., *Stretchable Electronics.* Weinheim (Germany): Wiley-VHC., 2013.

[42] Wang, H., Zhang, Q.M., Cross, L.E. and Sykes, A.O., "Piezoelectric, dielectric, and elastic properties of poly(vinylidene fluoride/trifluoroethylene)," *Journal of Applied Physics*, vol. 74, pp. 3394–3398, 1993.

[43] Galpaya, D., Wang, M., Liu, W., Motta, N., Waclawik, E. and Yan, C., "Recent advances in fabrication and characterization of graphene-polymer nanocomposites," *Graphene*, vol. 1, pp. 30–49, 2012.

[44] Somiya, S., Aldinger, F., Claussen, N., Spriggs, R.M., Uchino, K., Koumoto, K. and Kaneno, M., *Handbook of Advanced Ceramics* . Elsevier Inc., 2003.

[45] Kim, S., *Low power energy harvesting with piezoelectric generators.* PhD thesis, University of Pittsburgh (Pittsburgh (PA), USA), 2002.

[46] Mo, C., Kim, S. and Clark, W.W., "Theoretical analysis of energy harvesting performance for unimorph piezoelectric benders with interdigitated electrodes," *Smart Materials and Structures*, vol. 18, 2009. 055017 (8pp.).

[47] Lodeiro, M.J., Stewart, M., and Cain, M., "A round-robin to measure the direct piezoelectric coefficient using the berlincourt method," 2004. VAMAS Technical Working Area 24 - Performance related properties of electroceramics (Report No. 47).

[48] European Committee for Electrotechnical Standardization, "Piezoelectric properties of ceramic materials and components – Part 2: Methods of measurement – Low power (EN 50324-2)," May 2002. Brussels (Belgium).

[49] Pardo, L. and Brebol, K., *Properties of ferro-piezoelectric ceramic materials in the linear range: determination from impedance measurements at resonance.* Dordrecht (the Netherlands): Springer Science + Business Media, 1 ed., 2011. Chapter 13 of Multifunctional Polycrystalline Ferroelectric Materials.

[50] Kwok, K.W., Chan, H.L.W., and Choy, C.L. , "Evaluation of the material parameters of piezoelectric materials by various methods," *IEEE Transactions on Ultrasonics, Ferroelectrics, and Frequency Control*, vol. 4, pp. 733–742, 1997.

[51] Cao, W., Zhu, S., and Jiang, B. , "Analysis of shear modes in a piezoelectric vibrator," *Journal of Applied Physics*, vol. 1998, pp. 4415–4420, 83.

[52] Aurelle, N. Roche, D., Richard, C., and Gonnard, P. , "Sample aspect ratio influence on the shear coefficients," *Proceedings of the Ninth IEEE International Symposium on Applications of Ferroelectrics*, vol. 1995, pp. 162–165, 1995.

[53] Dorf, R.C., *The Electrical Engineering Handbook.* Boca Raton (FL, USA): CRC Press, 2 ed., 1997.

[54] Milyutin, E., Gentil, S., and Muralt, P., "Shear mode bulk acoustic wave resonator based on c-axis oriented AlN thin film," *Journal of Applied Physics*, vol. 104, 2008. 084508.

[55] Suarez-Gomez, A., Saniger-Blesa, J.M. and Calderon-Pinar, F., "Universal synthesis of PZT (1-x)/x submicrometric structures using highly stable colloidal dispersions: A bottom-up approach," *Advances in Ferroelectrics*, 2012. ISBN: 978-953-51-0885-6 (In-Tech).

[56] Liu, Z., Chen, P., Zhang, X. and Yu, C., "Degradation of plasma-treated poly(p-phenylene benzobisoxazole) fiber and its adhesion with bismaleimide resin," *RSC Advances*, vol. 4, pp. 3893–3899, 2014.

[57] Deutz, D.B., Tempelman, E., van der Zwaag, S., Groen, W.A., "Piezoelectric lead zirconium titanate composite touch sensors for integration with flexible OLED technology," *Proceedings of the European Conference on Application of Polar Dielectrics 2014*, 2014. In press.

[58] COMSOL Multiphysics, "COMSOL Multiphysics V4.4," November 2013. www.comsol.com.

[59] Spicci, L. and Cati, M., "Ultra-sound piezo-disk transducer model for material parameter optimization," *Proceedings of the COMSOL Conference 2010 (Paris)*, 2010.

[60] Ferroperm Piezoceramics A/S, "Full Data Matrix." www.ferroperm-piezo.com, 2006.

[61] Kar-Gupta, R. and Venkatesh, T.A., "Electromechanical response of piezoelectric composites: effects of geometric connectivity and grain size," *Acta Materiala*, vol. 56, pp. 3810–3823, 2008.

[62] Guo, Z., Shi, X., Chen, Y., Chen, H., Peng, X., and Harrison, P., "Mechanical modeling of incompressible particle-reinforced neo-hookean composites based on numerical homogenization," *Mechanics of Materials*, vol. 70, pp. 1–17, 2014.

[63] Chambion, B., Goujon, L., Badie, L., Mugnier, Y., Barthod, C., Galez, C., Wiebel, S. and Venet, C., "Optimization of the piezoelectric response of 0-3 composites: a modeling approach," *Smart Materials and Structures*, vol. 20, 2011. 115006 (8pp.).

[64] Trindade, M.A. and Benjeddou, A., "Finite element homogeization technique for the characterization of $d_{15}$ shear piezoelectric macro-fibre composites," *Smart Materials and Structures*, vol. 20, 2011. 075012 (17pp.).

[65] Smith, W. and Auld, B., "Modeling of 1-3 composite piezoelectrics: thickness-mode oscillation," *IEEE Transcriptions on Ultrasonics, Ferroelectrics, and Frequency Control*, vol. 40, pp. 41–49, 1993.

[66] Prasad, G. and Madhusudhana, R.C.V., "Characterization of 1-3 piezoelectric polymer composites - a numerical and analytical evaluation procedure for thickness mode vibrations," *Condensed Matter Physics*, vol. 13, pp. 1–10, 2010.

[67] Benjeddou, A. and Al-Ajmi, M., "Analytical homogenizations of piezoceramic shear macro-fibre composites," *Proceedings of the IUTAM Symposium on Multiscale Modelling of Fatigue, Damage and Fracture in Smart Materials Systems*, vol. 1, pp. 229–242, 2011.

[68] Furukawa, T., Fujino, K., and Fukada, E., "Electromechanical properties in the composites of epoxy resins and PZT ceramics," *Japanese Journal of Applied Physics*, vol. 15, pp. 2119–2129, 1976.

[69] Wong, C.K., Poon, Y.M., and Shin, F.G., "Explicit formulas for effecive piezoelectric coefficients of ferroelectric 0-3 composites based on effective medium theory," *Journal of Applied Physics*, vol. 93, pp. 487–496, 2003.

[70] Klicker, K.A., *Piezoelectric Composite with 3-1 Connectivity for Transducer Applications.* Phd thesis, The Pennsylvania State University (State College (PA), USA), 1980.

[71] Hibbeler, R.C., *Mechanics of Materials.* Singapore: Prentice Hall - Pearson Education South Asia Pte Ltd, 7 ed., 2008.

[72] Engan, H., "Excitation of elastic surface waves by spatial harmonics of interdigital transducers," *IEEE Transactions on Electron Devices*, vol. 16, pp. 1014–1017, 1969.

[73] Mathworks, "MATLAB R2011b," March 2011. www.mathworks.com.

[74] Kranz, B., Benjeddou, A., and Drossel, W.-G., "Numerical and experimental characterizations of longitudinally polarized piezoelectric $d_{15}$ shear macro-fiber composites," *Acta Mechanica*, vol. 224, pp. 2471–2487, 2013.

[75] Smart Material Corporation, "Material Datasheet." www.smart-material.com, 2012.

[76] Andrews, C., Lin, Y., Sodano, H.A., "The effect of particle aspect ratio on the electroelastic properties of piezoelectric nanocomposites," *Smart Materials and Structures*, vol. 19, 2010. 025018 (14pp.).

Appendix A
# Electromechanical material properties

**Epoxy [74]**

$$\rho = 1150 \frac{kg}{m^3} \tag{A.1}$$

$$\bar{\bar{s}}^E = 10^{-10} \cdot \begin{bmatrix} 3.45 & -1.03 & -1.03 & 0 & 0 & 0 \\ -1.03 & 3.45 & -1.03 & 0 & 0 & 0 \\ -1.03 & -1.03 & 3.45 & 0 & 0 & 0 \\ 0 & 0 & 0 & 4.48 & 0 & 0 \\ 0 & 0 & 0 & 0 & 4.48 & 0 \\ 0 & 0 & 0 & 0 & 0 & 4.48 \end{bmatrix} [Pa^{-1}] \tag{A.2}$$

$$\bar{\bar{d}} = \bar{\bar{0}} \quad [\frac{C}{N}] \tag{A.3}$$

$$\bar{\epsilon}^T = \begin{bmatrix} 4.5 \\ 4.5 \\ 4.5 \end{bmatrix} [-] \tag{A.4}$$

**PZT5A4 [14]**[1]

$$\rho = 7900 \frac{kg}{m^3} \tag{A.5}$$

$$\bar{\bar{s}}^E = 10^{-11} \cdot \begin{bmatrix} 1.68 & -0.56 & -0.56 & 0 & 0 & 0 \\ -0.56 & 1.68 & -0.56 & 0 & 0 & 0 \\ -0.56 & -0.56 & 1.80 & 0 & 0 & 0 \\ 0 & 0 & 0 & 4.50 & 0 & 0 \\ 0 & 0 & 0 & 0 & 4.50 & 0 \\ 0 & 0 & 0 & 0 & 0 & 4.50 \end{bmatrix} [Pa^{-1}] \tag{A.6}$$

$$\bar{\bar{d}} = 10^{-10} \cdot \begin{bmatrix} 0 & 0 & 0 & 0 & 5.50 & 0 \\ 0 & 0 & 0 & 5.50 & 0 & 0 \\ -1.95 & -1.95 & 4.60 & 0 & 0 & 0 \end{bmatrix} [\frac{C}{N}] \tag{A.7}$$

$$\bar{\epsilon}^T = \begin{bmatrix} 1650 \\ 1650 \\ 1850 \end{bmatrix} [-] \tag{A.8}$$

**Sonox SP53 [75]**[1]

$$\rho = 7450 \frac{kg}{m^3} \tag{A.9}$$

$$\bar{\bar{s}}^E = 10^{-11} \cdot \begin{bmatrix} 1.58 & -0.49 & -0.49 & 0 & 0 & 0 \\ -0.49 & 1.58 & -0.49 & 0 & 0 & 0 \\ -0.49 & -0.49 & 2.29 & 0 & 0 & 0 \\ 0 & 0 & 0 & 7.70 & 0 & 0 \\ 0 & 0 & 0 & 0 & 7.70 & 0 \\ 0 & 0 & 0 & 0 & 0 & 7.70 \end{bmatrix} [Pa^{-1}] \tag{A.10}$$

$$\bar{\bar{d}} = 10^{-10} \cdot \begin{bmatrix} 0 & 0 & 0 & 0 & 7.71 & 0 \\ 0 & 0 & 0 & 7.71 & 0 & 0 \\ -2.75 & -2.75 & 6.80 & 0 & 0 & 0 \end{bmatrix} [\frac{C}{N}] \tag{A.11}$$

$$\bar{\epsilon}^T = \begin{bmatrix} 3580 \\ 3580 \\ 3800 \end{bmatrix} [-] \tag{A.12}$$

---

[1]As the values of $s_{12}^E$, $s_{13}^E$, $s_{23}^E$, $s_{66}^E$ are not available in the literature, $s_{12}^E = s_{13}^E = s_{23}^E = \nu \cdot s_{11}^E$ and $s_{66}^E = s_{55}^E$ was assumed, where $\nu$ is the reported material's *Poisson*'s ratio.

## PZT5-H [58]

$$\rho = 7500 \frac{kg}{m^3} \tag{A.13}$$

$$\bar{\bar{d}} = 10^{-10} \cdot \begin{bmatrix} 0 & 0 & 0 & 0 & 7.41 & 0 \\ 0 & 0 & 0 & 7.41 & 0 & 0 \\ -2.74 & -2.74 & 5.93 & 0 & 0 & 0 \end{bmatrix} [\frac{C}{N}] \tag{A.15}$$

$$\bar{\bar{s}}^E = 10^{-11} \cdot \begin{bmatrix} 1.65 & -0.478 & -0.845 & 0 & 0 & 0 \\ -0.478 & 1.65 & -0.845 & 0 & 0 & 0 \\ -0.845 & -0.845 & 2.07 & 0 & 0 & 0 \\ 0 & 0 & 0 & 4.35 & 0 & 0 \\ 0 & 0 & 0 & 0 & 4.35 & 0 \\ 0 & 0 & 0 & 0 & 0 & 4.26 \end{bmatrix} [Pa^{-1}] \tag{A.14}$$

$$\bar{\bar{\epsilon}}^T = \begin{bmatrix} 3130 \\ 3130 \\ 3400 \end{bmatrix} [-] \tag{A.16}$$

## PZ27 [60]

$$\rho = 7700 \frac{kg}{m^3} \tag{A.17}$$

$$\bar{\bar{d}} = 10^{-10} \cdot \begin{bmatrix} 0 & 0 & 0 & 0 & 5.06 & 0 \\ 0 & 0 & 0 & 5.06 & 0 & 0 \\ -1.70 & -1.70 & 4.25 & 0 & 0 & 0 \end{bmatrix} [\frac{C}{N}] \tag{A.19}$$

$$\bar{\bar{s}}^E = 10^{-11} \cdot \begin{bmatrix} 1.70 & -0.66 & -0.816 & 0 & 0 & 0 \\ -0.66 & 1.70 & -0.816 & 0 & 0 & 0 \\ -0.816 & -0.816 & 2.30 & 0 & 0 & 0 \\ 0 & 0 & 0 & 4.35 & 0 & 0 \\ 0 & 0 & 0 & 0 & 4.35 & 0 \\ 0 & 0 & 0 & 0 & 0 & 4.71 \end{bmatrix} [Pa^{-1}] \tag{A.18}$$

$$\bar{\bar{\epsilon}}^T = \begin{bmatrix} 1796 \\ 1796 \\ 1802 \end{bmatrix} [-] \tag{A.20}$$

## Bulk properties for the adaptive IDE patch model

$$\rho = \rho_0 \frac{kg}{m^3} \tag{A.21}$$

$$\bar{\bar{d}} = \begin{bmatrix} 0 & 0 & 0 & 0 & d_{15} & 0 \\ 0 & 0 & 0 & d_{15} & 0 & 0 \\ d_{31} & d_{31} & d_{33} & 0 & 0 & 0 \end{bmatrix} [\frac{C}{N}] \tag{A.23}$$

$$\bar{\bar{s}}^E = \cdot \begin{bmatrix} s_{11}^E & s_{12}^E & s_{13}^E & 0 & 0 & 0 \\ s_{12}^E & s_{22}^E & s_{23}^E & 0 & 0 & 0 \\ s_{13}^E & s_{23}^E & s_{33}^E & 0 & 0 & 0 \\ 0 & 0 & 0 & s_{44}^E & 0 & 0 \\ 0 & 0 & 0 & 0 & s_{55}^E & 0 \\ 0 & 0 & 0 & 0 & 0 & s_{66}^E \end{bmatrix} [Pa^{-1}] \tag{A.22}$$

$$\bar{\bar{\epsilon}}^T = \begin{bmatrix} \epsilon_{11}^T \\ \epsilon_{22}^T \\ \epsilon_{33}^T \end{bmatrix} [-] \tag{A.24}$$

## Aluminium [58]

$$\rho = 2700 \frac{kg}{m^3} \tag{A.25}$$

$$\bar{\bar{d}} = \bar{\bar{0}} \quad [\frac{C}{N}] \tag{A.27}$$

$$\bar{\bar{s}}^E = 10^{-11} \cdot \begin{bmatrix} 1.43 & -0.47 & -0.47 & 0 & 0 & 0 \\ -0.47 & 1.43 & -0.47 & 0 & 0 & 0 \\ -0.47 & -0.47 & 1.43 & 0 & 0 & 0 \\ 0 & 0 & 0 & 3.80 & 0 & 0 \\ 0 & 0 & 0 & 0 & 3.80 & 0 \\ 0 & 0 & 0 & 0 & 0 & 3.80 \end{bmatrix} [Pa^{-1}] \tag{A.26}$$

$$\bar{\bar{\epsilon}}^T = \begin{bmatrix} 1 \\ 1 \\ 1 \end{bmatrix} [-] \tag{A.28}$$

# Appendix B

# Set-up $d_{33}$ and $d_{31}$ simulations

Table B.1 summarizes the two sets of RVE boundary conditions applied for the homogenization-based $d_{33}$ and $d_{31}$ simulations [63, 76]. Equations B.1 and B.2 were applied to compute the effective $d_{33}$ and $d_{31}$, respectively.

$$d_{33} = \frac{\hat{S}_3}{\hat{E}_3} = \frac{\frac{1}{A} \int_A S_3 dA}{\frac{1}{A} \int_A E_3 dA} \tag{B.1}$$

$$d_{31} = \frac{\hat{S}_1}{\hat{E}_3} = \frac{\frac{1}{A} \int_A S_1 dA}{\frac{1}{A} \int_A E_3 dA} \tag{B.2}$$

| Case | Property | BC | 1 | 2 | 3 | 4 | A |
|------|----------|-----|---------|-------|-------|----------|---|
| **IV** | $d_{33}$ | MBC | $dv$=0 | − | $dv$=0 | $du$=$dv$=0 | − |
|      |          | EBC | − | $V = 1$ | − | $V = 0$ | − |
| **V** | $d_{31}$ | MBC | $du$=$dv$=0 | − | − | − | − |
|      |          | EBC | − | $V = 1$ | − | $V = 0$ | − |

**Table B.1:** Mechanical and electrical boundary conditions for the $d_{33}$ and $d_{31}$ effective property simulations with the RVE defined by Figure 2.12). Note that the '−' symbol indicates symmetrical boundary conditions with respect to the opposite boundary line. (E/M)BC = (Electrical/Mechanical) Boundary Condition(s).